

# REGULARIZATION APPROACHES FOR RESTORING IMAGES CORRUPTED BY DATA CORRELATED NOISE MODELS

Thesis

Submitted in partial fulfillment of the requirements for the degree of

DOCTOR OF PHILOSOPHY

by

SHIVARAMA HOLLA K



DEPARTMENT OF MATHEMATICAL & COMPUTATIONAL SCIENCES

NATIONAL INSTITUTE OF TECHNOLOGY KARNATAKA

SURATHKAL, MANGALORE - 575025

October, 2018



*Dedicated to...*

*My beloved parents  
and family members...*

*&*

*All of my Teachers and Colleagues...*



## DECLARATION

I hereby *declare* that the Research Thesis entitled **REGULARIZATION APPROACHES FOR RESTORING IMAGES CORRUPTED BY DATA CORRELATED NOISE MODELS** which is being submitted to the **National Institute of Technology Karnataka, Surathkal** in partial fulfillment of the requirements for the award of the Degree of **Doctor of Philosophy in Mathematical and Computational Sciences** is a *bonafide report of the research work carried out by me*. The material contained in this Research Thesis has not been submitted to any University or Institution for the award of any degree.

Shivarama Holla K

Reg. No.: 155002 MA15F08

Department of Mathematical and Computational Sciences

Place: NITK, Surathkal.

Date: October 25, 2018



## **CERTIFICATE**

This is to *certify* that the Research Thesis entitled **REGULARIZATION APPROACHES FOR RESTORING IMAGES CORRUPTED BY DATA CORRELATED NOISE MODELS** submitted by **SHIVARAMA HOLLA K**, (Reg. No.: 155002 MA15F08) as the record of the research work carried out by him, is *accepted as the Research Thesis submission* in partial fulfillment of the requirements for the award of degree of **Doctor of Philosophy**.

(Dr. Jidesh P.)

Research Supervisor

Chairman - DRPC





# ACKNOWLEDGMENT

I would like to use this opportunity to show my gratitude towards the people who have helped in my research work and writing this thesis.

First and foremost, my sincere gratitude and appreciation goes to my research supervisor, *Dr. Jidesh P.*, Department of Mathematical and Computational Sciences, for all the benevolent support and precious guidance throughout my doctoral work. All your expert advice and encouragement helped me to concentrate on my research which I gratefully thank you. It has been my honor to work with you.

Further I thank one of my RPAC members, *Dr. Shashidhar G Koolagudi*, Department of Computer Science and Engineering, for examining all my reports and giving valuable suggestions, which were helpful in improving this work. Also, I thank *Prof. Francoise Malgouyres*, Institute of Mathematics of Toulouse, Faculty of Science and Engineering, Universite Paul Sabatier, France and *Dr. Partha Pratim Roy*, Assistant Professor, Department of Computer Science and Engineering, IIT Roorkee, for evaluating my thesis and appreciating my work.

I am thankful to *Prof. Santhosh George*, former Head of the Department and also one of my RPAC members of Mathematical and Computational Sciences and *Prof. B.R. Shankar*, Head of the Department of Mathematical and Computational Sciences, for providing better facilities and developing good infrastructure for research in the department. I also thank all the teaching and non-teaching staff for all their support and help. I take this opportunity to thank my fellow research scholars of the Department of Mathematical and Computational Sciences for helping me and making my stay at NITK wonderful and memorable. I would like to extend my gratitude towards the official staffs of academic and hostel office for helping me for all the official works related to my research.

Finally, I am thankful to my parents, brother, sister, and friends for supporting my decision of opting for Ph.D. Their encouragement helped me in the successful completion of my research.

Place: NITK, Surathkal

Shivarama Holla K

Date: October 25, 2018



# ABSTRACT

This thesis is dedicated to study the problem of restoring images corrupted by data correlated noise and linear blurring artifacts. Image restoration being an ill-posed problem, a closed form solution hardly exists, even if one exists, it does not continuously depend on the data. Therefore, in general, an iterative solution is being sought under a regularization framework. To this end, the image degradation process is modeled mathematically under a variational framework and it is solved using various computational methods to ensure the desired output.

Three different noise distributions (viz. Chi, Rayleigh and Poisson) are being considered in this thesis. The reason for choosing these distributions are well justified by their presence in various practical imaging modalities such as Magnetic Resonance (MR), Synthetic Aperture Radar (SAR), Ultrasound(US) etc. Three different restoration models are proposed to handle these noise distributions and they are detailed in three chapters of this thesis. The Bayesian framework (which uses the statistical information of the noise present in an image to derive the energy functional) is being employed for designing the functional that corresponds to the model whose solution is being sought. The solutions (corresponding to the three restoration models proposed in this thesis) are provided using Non-Local Total Variational (NLTV), Non-Local Total Bounded Variational(NLTBV) and Non-Local  $p - norm$  total variation schemes as the regularization priors, since they ensure preservation of the details in the input data better compared to many other state-of-the art regularization priors. The numerical solution is provided using the split Bregman iterative scheme to improve the convergence rate and reduce the parameter sensitivity of these models. Qualitative and quantitative analysis of these models are provided for various images from different imaging modalities (such as MR, SAR, US etc) to justify their performance and substantiate their relevance in the context of the current literature.

**Keywords:** Image restoration, data-correlated noise, split Bregman scheme, Total Variation, linear blur.

**AMS Classification:** 68U10, 94A08.



# Contents

<b>Abstract</b> . . . . .	i
<b>List of Figures</b> . . . . .	vi
<b>List of Tables</b> . . . . .	ix
<b>Nomenclature and Abbreviations</b> . . . . .	xi
<b>1 INTRODUCTION</b>	<b>1</b>
1.1 INVERSE PROBLEMS . . . . .	1
1.2 IMAGE RESTORATION AS AN INVERSE PROBLEM . . . . .	3
1.3 IMAGE DEGRADATION . . . . .	5
1.4 BRIEF HISTORY OF IMAGE RESTORATION PROBLEM . . . . .	11
1.5 SOLUTION TO AN IMAGE DEGRADATION PROBLEM . . . . .	12
1.5.1 Variational methods . . . . .	13
1.5.2 Deriving variational model using the MAP estimator . . . . .	15
1.5.3 Review of the variational models . . . . .	16
1.5.4 Nonlocal methods . . . . .	18
1.6 PROS AND CONS OF EXISTING VARIATIONAL MODELS . . . . .	20
1.7 MOTIVATION OF THE RESEARCH . . . . .	21
1.8 PERFORMANCE MEASURES . . . . .	21
1.9 RESEARCH OBJECTIVES . . . . .	23
1.10 ORGANIZATION AND CONTRIBUTIONS OF THE THESIS . . . . .	24
<b>2 NONLOCAL TOTAL BOUNDED VARIATION APPROACH TO RESTORE MULTIPLE-COIL MRI DATA</b>	<b>27</b>
2.1 INTRODUCTION . . . . .	27
2.2 NOISE FORMULATION . . . . .	28
2.2.1 Theory . . . . .	29
2.3 OVERVIEW OF MRI RESTORATION . . . . .	31
2.4 RESEARCH WORK . . . . .	33

2.4.1	Energy functional using MAP estimator . . . . .	33
2.4.2	Split-Bregman Iteration Method . . . . .	34
2.4.3	Formulated model using split-Bregman iteration scheme . . . . .	37
2.4.4	Algorithm for the proposed scheme . . . . .	40
2.5	EXPERIMENTAL RESULTS . . . . .	40
2.6	Summary . . . . .	44
<b>3</b>	<b>NON LOCAL TOTAL VARIATION REGULARIZATION MODELS FOR RESTORING RAYLEIGH NOISE</b>	<b>55</b>
3.1	INTRODUCTION . . . . .	55
3.1.1	Speckle reduction in brief . . . . .	56
3.1.2	Ultrasound image . . . . .	56
3.1.3	Synthetic Aperture Radar image . . . . .	57
3.2	RESEARCH WORK . . . . .	59
3.2.1	Variance stabilizing transform for Rayleigh distribution . . . . .	60
3.2.2	The formulated variational models for Rayleigh distributed noise	61
3.2.3	Split-Bregman iteration scheme for the proposed models . . . . .	63
3.2.4	Algorithm to implement the methods . . . . .	66
3.3	EXPERIMENTAL RESULTS . . . . .	68
3.4	Summary . . . . .	80
<b>4</b>	<b>NONLOCAL VARIATIONAL APPROACH TO RESTORE POISSONIAN IMAGES</b>	<b>83</b>
4.1	INTRODUCTION . . . . .	83
4.1.1	Computed Tomography . . . . .	84
4.1.2	Fluorescence and confocal microscopy . . . . .	86
4.1.3	Variational methods for Poisson restoration . . . . .	87
4.1.4	Non-local $p - norm$ filter . . . . .	89
4.2	RESEARCH WORK . . . . .	90
4.2.1	Non-local variational model for Poisson noise reduction . . . . .	90
4.3	EXPERIMENTAL RESULTS . . . . .	92
4.4	Summary . . . . .	94
<b>5</b>	<b>CONCLUSIONS AND FUTURE SCOPES</b>	<b>103</b>
5.1	CONCLUDING REMARKS . . . . .	103
5.2	FUTURE SCOPE OF THE RESEARCH . . . . .	105

<b>A</b>	<b>Appendix A</b>	<b>107</b>
A.1	EXAMPLE FOR AN ILL-POSED PROBLEM . . . . .	107
A.2	EULER-LAGRANGIAN DERIVATIVE . . . . .	107
A.3	CONDITION FOR EXISTENCE OF A UNIQUE SOLUTION FOR <i>Chi</i> DISTRIBUTED RESTORATION MODEL . . . . .	108
A.4	UNIQUENESS OF THE SOLUTIONS OF RAYLEIGH MODELS . . .	110
<b>B</b>	<b>Appendix B</b>	<b>111</b>
B.1	MAP ESTIMATOR FOR THE NON-CENTRAL <i>Chi</i> DISTRIBUTION	111
B.2	MAP ESTIMATE FOR THE RAYLEIGH DISTRIBUTION . . . . .	113
B.3	MAP ESTIMATOR FOR POISSON DISTRIBUTION . . . . .	114
<b>C</b>	<b>Appendix C</b>	<b>117</b>
C.1	SAMPLE CODE FOR THE NLTV FILTER USING SPLIT BREG- MAN ITERATIVE SCHEME . . . . .	117
	<b>Bibliography</b> . . . . .	120
	<b>List of Publications</b> . . . . .	133





## List of Figures

1.1	Gaussian PDF . . . . .	6
1.2	Image with Gaussian noise . . . . .	6
1.3	Gamma PDF . . . . .	7
1.4	Image with Gamma noise . . . . .	7
1.5	Rayleigh PDF . . . . .	8
1.6	Image corrupted by Rayleigh noise . . . . .	8
1.7	Rician PDF . . . . .	9
1.8	Image corrupted by Rician noise . . . . .	9
1.9	Poisson PDF . . . . .	10
1.10	Image corrupted by Poisson noise . . . . .	10
1.11	Results of TV and Tikhonov . . . . .	17
1.12	Non-local restoration methods . . . . .	19
2.1	Multiple-coil MRI formation . . . . .	28
2.2	Non-central <i>Chi</i> PDF . . . . .	30
2.3	Bregman distance . . . . .	35
2.4	Magnitude images in <i>k</i> – <i>space</i> . . . . .	42
2.5	Test images considered for <i>Chi</i> restoration . . . . .	43
2.6	Comparision: Rician . . . . .	46
2.7	Comparision: Rician noise and linear blur . . . . .	46
2.8	MRI Results 1 . . . . .	48
2.9	MRI Results 2 . . . . .	49
2.10	Multiple-coil MRI Results 1 . . . . .	50
2.11	Multiple-coil MRI Results 2 . . . . .	51
2.12	Comparision: <i>Chi</i> noise . . . . .	52

2.13	Comparison: <i>Chi</i> noise and linear blur . . . . .	52
3.1	Ultrasound imaging mechanism . . . . .	58
3.2	SAR imaging system . . . . .	59
3.3	Test images considered in Rayleigh restoration . . . . .	70
3.4	Results: VST . . . . .	71
3.5	Results: Babera . . . . .	72
3.6	Results: Peppers . . . . .	72
3.7	Results: Synthetic-1 . . . . .	73
3.8	Results: Synthetic-2 . . . . .	73
3.9	Results: Ultrasound . . . . .	74
3.10	Results: SAR . . . . .	75
3.11	Results: Peppers-color . . . . .	75
3.12	Results: Enlarged peppers . . . . .	76
3.13	Results: Enlarged Barbera . . . . .	76
3.14	Absolute error analysis . . . . .	77
3.15	Box plot . . . . .	79
4.1	CT imaging technique . . . . .	85
4.2	A sample CT image . . . . .	85
4.3	Fluorescence microscope . . . . .	87
4.4	Fluorescence image of an amoeba . . . . .	88
4.5	Test images considered for Poisson restoration . . . . .	97
4.6	Poisson restoration 1 . . . . .	97
4.7	Poisson restoration 2 . . . . .	98
4.8	Poisson restoration 3 . . . . .	98
4.9	Poisson restoration 4 . . . . .	99
4.10	Poisson restoration 5 . . . . .	99
4.11	Poisson restoration 6 . . . . .	100
4.12	Poisson restoration 7 . . . . .	100
4.13	1-D data restoration . . . . .	101
4.14	Comparison with several $p$ values . . . . .	101

## List of Tables

2.1	Parameter values . . . . .	45
2.2	SNR values: Rician noise . . . . .	47
2.3	SNR values: Rician-noise and blur . . . . .	47
2.4	SSIM values: Rician noise . . . . .	47
2.5	SSIM values: Rician-noise and blur . . . . .	47
2.6	SNR values: non-central <i>Chi</i> -noise . . . . .	53
2.7	SNR values: non-central <i>Chi</i> -noise and blur . . . . .	53
2.8	SSIM values: non-central <i>Chi</i> -noise . . . . .	53
2.9	SSIM values: non-central <i>Chi</i> -noise and blur . . . . .	53
3.1	SNR values: Rayleigh restoration . . . . .	78
3.2	SSIM values: Rayleigh restoration . . . . .	78
3.3	Parameter values: Rayleigh restoration . . . . .	80
4.1	Quality metrics for Poisson restoration . . . . .	96
4.2	Parameter values for different methods for peak (30,70) . . . . .	96



## Nomenclature and Abbreviations

Symbol	Representation
$u_0$	: Input image
$u$	: Original image
$n$	: Noise
$\sigma$	: Standard deviation
$\rho$	: Correlation coefficient
$\mu$	: Mean
$K$	: Blurring operator
$k$	: Filter mask
$*$	: Convolution operator
$\Omega$	: Image domain
$\lambda$	: Regularization parameter
$\mathbb{R}$	: Real space
$\mathcal{P}$	: Penalty function
$\mathcal{H}$	: Heaviside function
$\mathcal{N}$	: Neighborhood
$\phi$	: Objective function
$J$	: Regularization functional
$P$	: Probability function
$\Delta$	: Laplacian operator
$\Delta_{NL}$	: Non-local Laplacian operator
$\nabla$	: Gradient operator
$\nabla_{NL}$	: Non-local gradient operator
$div$	: Divergence function
$div_{NL}$	: Non-local divergence
$\partial$	: Partial derivative
$\ \cdot\ $	: Euclidean norm
$ \cdot $	: Absolute value
$\Sigma$	: summation
$\forall x$	: for all $x$

### Abbreviations and expansions

NLTBV : Non-Local Total Bounded Variation	SB : Split Bregman
SAR : Synthetic Aperture Radar	US : Ultrasound
MAP : Maximum A Posteriori	TV : Total Variation
NLTV : Non-Local TV	TBV : Total Bounded Variation
PSF : Point Spread Function	PDF : Probability Density Function
IID : Identically and Independently Distributed	MLE : Maximum Likelihood Estimator
BV : Bounded Variation	NLM : Non-Local Means



# Chapter 1

## INTRODUCTION

### 1.1 INVERSE PROBLEMS

Many well-known problems in the field of science and engineering are categorically inverse in nature (Vogel (2002); Bertero and Boccacci (1998)). Being ubiquitous in most computing applications, these problems have attracted the attention of scientist and engineers for decades altogether. Apart from various problems in the other disciplines, the applicability of these problems also spans over imaging and image processing, such as medical imaging like X-ray, Computed Tomography (CT), Magnetic Resonance (MR), ultrasound, etc and satellite imaging systems like, Synthetic Aperture Radar(SAR), hyperspectral, multi-spectral, etc.

Inverse problem is defined as the problem in which the solution is known, using this solution, the problem is derived with certain conditions and prior knowledge of the given solution (Hansen (2010)). For example, let  $Ax = B$ , in which  $B$  is given and we have some prior knowledge about the degradation  $A$  (is a known linear operator), using this knowledge, one has to find the value of  $x$ . If the solution of this problem satisfies the following three conditions: 1. existence, 2. uniqueness and 3. continuous dependence on the initial data, then it is said to be a well-posed problem (Hadamard and Morse (1953)). If the solution fails to satisfy any one of these three criteria, then the problem is said to be an ill-posed one. See Appendix A.1 for the numerical verification of an inverse ill-posed problem.

One of the well-known techniques for solving an ill-posed inverse problem is penalization model. This theory deals with solving an inverse problem, by stating it as a

constrained minimization problem, which is further approximated to an unconstrained minimization problem by adding the penalty function. For instance, let the constrained minimization problem be

$$\min_x f(x) \quad \text{subject to } x \in \Omega, \quad (1.1)$$

where  $\Omega \subset \mathbb{R}^n$ . Above problem is approximated to an unconstrained minimization problem using the Lagrange formulation as,

$$\min_x \{f(x) + \lambda \mathcal{P}(x)\}, \quad (1.2)$$

where  $\mathcal{P} : \mathbb{R}^n \rightarrow \mathbb{R}$ , is the penalty function and  $\lambda$  is the penalty parameter.  $\mathcal{P}$  is said to be a penalty function if it satisfies the following conditions:

1.  $\mathcal{P}$  is continuous.
2.  $\mathcal{P}(x) = 0$  if and only if  $x \in \Omega$ .
3.  $\mathcal{P}(x) \geq 0$  for all  $x \in \mathbb{R}^n$ .

The penalization theory is further categorized into two: regularization framework and sparsity model. The data of interest is sufficiently smooth in case of regularization, whereas sparsity models consider the data as sparsely represented on a given basis. Now let us consider the inverse problem,

$$Ax + \varepsilon = B, \quad (1.3)$$

where  $\varepsilon$  is an additive noise in the observed data  $B$ . Using the penalization theory to solve above problem gives,

$$\min_x \{ \|Ax - b\|_{L_2} + \lambda \|x\|_{L_p} \}, \quad (1.4)$$

where  $\lambda$  acts as the regularization parameter and  $L_2$  represents  $L_2$  norm ( $\|\cdot\|_p$  will be used instead of  $\|\cdot\|_{L_p}$  throughout this thesis). When  $p = 0$  ( $L_0$  norm) or  $p = 1$  ( $L_1$  norm), the problem tends to a sparsity reduction model and for  $p > 1$  its a regularization framework, in general. Though the penalization approach provides a satisfying approximation to the desired data, it does not care about the statistical properties of the distortion such as distribution (Mohammad Djafari (2002)). To overcome such situations, a statistical approach such as Bayesian inference method is employed. In this approach, a prior knowledge of the perturbation and unknowns i.e,  $\varepsilon$  and  $x$  in (1.3), are translated to prior probability laws  $P(\varepsilon)$  and  $P(x)$ , respectively. Hence the observed



data can be represented as  $P(B|x)$ . The posterior probability of the desired data  $P(x|B)$  is then determined by applying the Bayes rule, given by,

$$P(P1|P2) = \frac{P(P2|P1)P(P1)}{P(P2)}, \quad (1.5)$$

where generally  $P1, P2$  are events and  $P(P2) \neq 0$ . Finally, estimation theories such as Maximum A Posteriori (MAP) or Maximum Likelihood (ML) estimator are employed in order to get a better approximation to the desired data  $x$ .

From the discussion regarding the inverse problems and their solutions using the two aforementioned approaches, one can conclude that the penalization method gives a better approximation to the original data, but it tends to neglect the statistical knowledge in the given noisy data. Whereas, the Bayesian approach maps a priori information in a distortion into an appropriate probabilistic law and solves it using one of the estimation techniques to get a much better approximation to the required data. Since we are dealing with images, our primary goal is to perform the image restoration by stating it as an inverse problem, which is detailed in the next section.

## 1.2 IMAGE RESTORATION AS AN INVERSE PROBLEM

A digital image comprises of a matrix with intensity values acquired by the active light sensors (in the visible range of the electromagnetic spectrum) in an image acquisition device. An atmospheric interference (such as lightning, dust, moisture etc), insufficient light while capturing the image data and defects in the acquisition device sensors cause disturbances in the acquired data leading to the so called noise. Improper focusing of the lens of the camera or motion of the object or subject also causes imperfections in the acquired images, generally coined as blurs. Both noise and blurring artifacts cause data loss and result in deviation of the acquired data from their original observations. Recovering of an image from such distortions meanwhile retaining vital information (such as sharp edges, textures and fine details) in the given image is the main task of image restoration. Due to uncertainty about the desired data, image restoration is an approximation problem. Hence, the problem thus defined is an inverse and ill-posed problem in the sense of Hadamard and Morse (1953). The given noisy and blurry image

data  $u_0$  is modeled as,

$$u_0 = Ku + n, \quad (1.6)$$

which is the most widely assumed data independent noise model (Gunturk and Li (2012)) where  $u$  is the original image,  $n$  is generally an additive white Gaussian noise with mean zero and  $K$  is the linear shift invariant blurring operator.

However, some of the prominent imaging fields such as medical(computed tomography, magnetic resonance, ultrasound etc.), microscopic(fluorescence, confocal) and satellite(synthetic aperture radar, multi and hyper-spectral etc.) produce images contaminated by data-correlated noise distortions. Here the image representation is different from the usual intensity images and the images are not generally formed in the visible range of the electromagnetic spectrum (Chang (2003); Borengasser et al. (2007)). For instance, CT images are formed in the X-ray frequency range and they represent the attenuation coefficient of the X-ray waves, whereas ultrasound images are formed due to the reflections of the sound wave from various objects, see Smith and Webb (2010) for the details of the image formation and representation in medical imaging. Restoring images from distortions such as noise and blur is a challenging task due to the inherent correlation between the data and noise, hence a proper modeling of the deterioration process needs to be done to yield better approximations to the original data. Regularization theory solves this problem by replacing (1.6) by

$$K^* u_0 = (K^* K + \lambda B') u_\lambda, \quad (1.7)$$

where  $\lambda$  is regularization parameter,  $B'$  is a positive definite operator such that  $K^* K + \lambda B'$  is an invertible operator with bounded inverse and  $K^*$  is the adjoint operator to  $K$ . The redefined inverse problem is then solved using a linear system of equations. Sparsity based methods replace (1.6) by

$$u^\lambda = \arg \min \|u_0 - Ku\|_2 + \lambda \|u\|_1. \quad (1.8)$$

Further, it is usually solved using the optimization(minimization) theory. As discussed earlier, the penalization theory neglects the nature of degradation. Deterioration of an image varies depending on the acquisition device and the environment in which it is being captured. Hence, these scenarios should be dealt with utmost care while designing the model to obtain a better approximation to the data of interest. The next sec-

tion highlights the design of a degradation problem and its solution using the Bayesian framework.

### 1.3 IMAGE DEGRADATION

As discussed in the previous section, in a real-world scenario, the formulation of an image is usually affected by two kinds of distortions namely, noise and blur. Blur is a common phenomenon in images which transpires due to the improper focusing of the camera lens (out of focus blur) and unexpected movement of the subject or the object (motion blur) (Hansen et al. (2006)) being imaged. An out of focus blur can be modeled as,

$$u_0 = Ku, \quad (1.9)$$

where  $K$  is a bounded linear blurring operator, under the assumption that it is shift invariant, the operation can be modified as a linear convolution(\*) with the Gaussian kernel  $k$ , eventually leading to the formulation

$$u_0 = k * u, \quad (1.10)$$

where  $k * u$  is the convolution of  $u$  with the filter mask  $k$ . As discussed earlier,  $u$  and  $u_0$  are original and corrupted images respectively. The point spread function of this blurring phenomena can be defined as a two-dimensional Gaussian function as follows,

$$K(i, j) = \frac{1}{2\pi\sigma^2} e^{-\frac{i^2+j^2}{2\sigma^2}}, \quad (1.11)$$

where  $\sigma$  is the standard deviation of the Gaussian distribution and  $(i, j)$  represents the Cartesian coordinates.

The image noise causes random fluctuations in all the pixel values. Let us recall the data-independent additive noise model (with the linear blur):

$$u_0 = Ku + n, \quad (1.12)$$

where  $n$  is usually zero mean white Gaussian noise which is random, identically and independently distributed (IID). The probability density function(PDF)  $P$  of Gaussian distribution is given by,

$$P(z|\sigma, \mu) = \frac{1}{\sigma\sqrt{2\pi}} e^{-\frac{(z-\mu)^2}{2\sigma^2}}, \quad (1.13)$$

where  $\sigma$  and  $\mu$  are the standard deviation and mean of a random sample  $z$  respectively. Gaussian plot for various values of  $\sigma$  and  $\mu$  are shown in Figure 1.1. A visual represen-

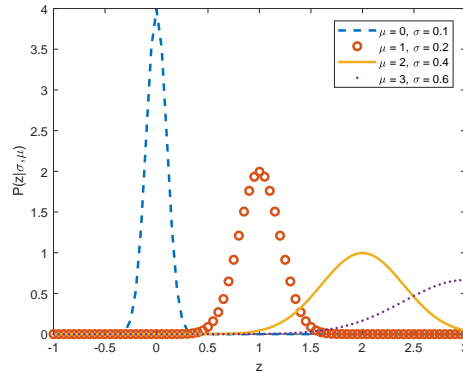


**Figure 1.1** Gaussian PDF with various mean and standard deviation.

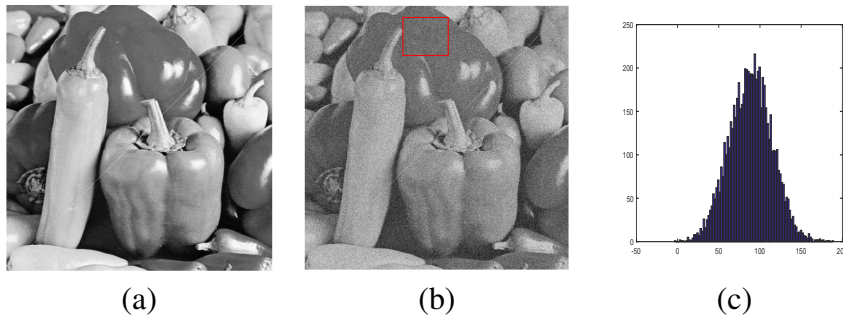


**Figure 1.2** (a) Original “Peppers” image, (b) corrupted by Gaussian noise, (c) histogram of highlighted area in (b).

tation of “peppers” image corrupted by Gaussian noise is shown in Figure 1.2(b) and histogram of the portion highlighted in this figure is given in Figure 1.2(c).

Many image degradation models, especially from medical and satellite modalities, are observed to follow a data-correlated noise distribution such as Rice, Gamma, Rayleigh, Poisson etc. For instance, in magnitude MR images the data is corrupted by Rician noise (Fernandez and Vega (2013)), ultrasound and SAR images are distorted by Rayleigh noise which is multiplicative in nature (Jin and Yang (2011a)). A multiplicative noise model is generally given by,

$$u_0 = Kun, \quad (1.14)$$

where  $n$  follows Gamma or Rayleigh distribution and has a unit mean. The PDF of

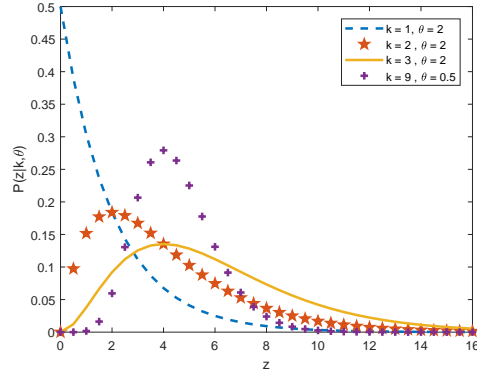


**Figure 1.3** Gamma PDF with different scale and shape parameters.

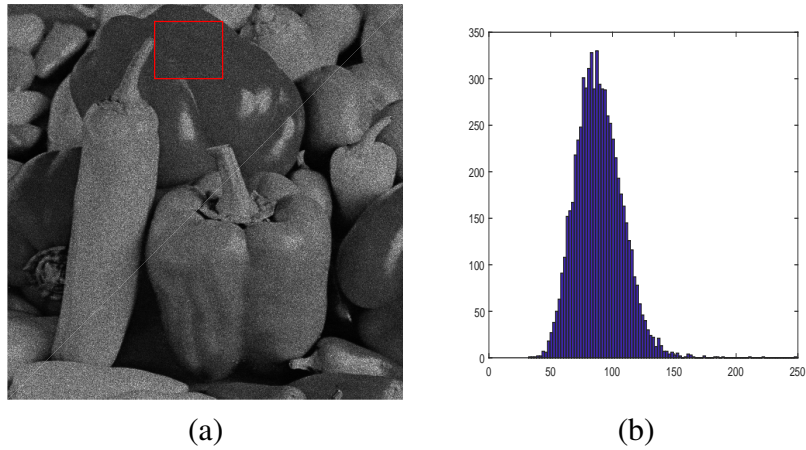


**Figure 1.4** (a)“Peppers” image corrupted by Gamma noise, (b) histogram of highlighted area in (a).

Gamma distribution is,

$$p(z|k, \theta) = \begin{cases} \frac{1}{\Gamma(k)\theta^k} z^{k-1} e^{-\frac{z}{\theta}} & \text{if } z \geq 0 \\ 0 & \text{if } z < 0 \end{cases}, \quad (1.15)$$

where  $k, \theta > 0$ , mean  $\mu = k\theta$  and variance  $\sigma^2 = k\theta^2$ . Plots of Gamma distributed PDF with different values of  $k$  and  $\theta$  are shown in Figure 1.3. The peppers image corrupted by gamma noise is given in Figure 1.4(a) and the histogram of the highlighted area in this image is given in Figure 1.4(b).

The PDF of the Rayleigh distribution is given by,

$$p(z|\sigma') = \frac{z}{\sigma'^2} e^{-\frac{z^2}{2\sigma'^2}}, \quad (1.16)$$

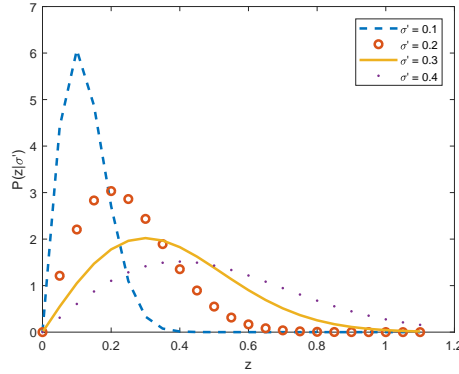


**Figure 1.5** Rayleigh PDF with different scale parameters.

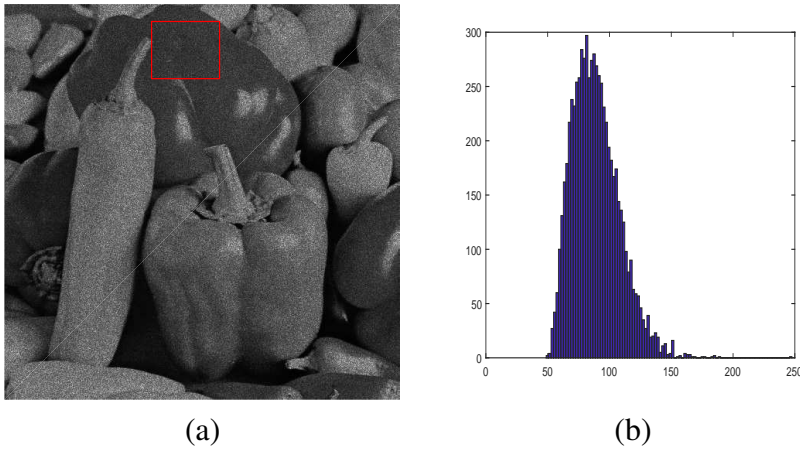


**Figure 1.6** (a)“Peppers” image corrupted by Rayleigh noise, (b) histogram of highlighted area in (a).

where  $\sigma'$  is a scale parameter, variance  $\sigma^2 = \frac{4-\pi}{2}\sigma'^2$  and mean  $\mu = \sigma'\sqrt{\pi/2}$ . The PDF plot of Rayleigh distribution with various  $\sigma'$  values are given in Figure 1.5. Rayleigh corrupted peppers image is shown in Figure 1.6(a) and histogram of the homogeneous area highlighted here is shown in Figure 1.6(b). The speckle noise which is multiplicative in nature usually follows either a Gamma or a Rayleigh PDF.

Apart from Rayleigh and Gamma, there are other noise distributions which are data-correlated, for instance, Rician and Poisson noise distortions are generally data-correlated. The PDF of a Rice distribution is,

$$p(z|\mu, \sigma) = \frac{z}{\sigma^2} e^{-\frac{(z^2+\mu^2)}{2\sigma^2}} I_0\left(\frac{z\mu}{\sigma^2}\right), \quad (1.17)$$

where  $I_0$  is the modified zeroth order Bessel function of the first kind. As mentioned

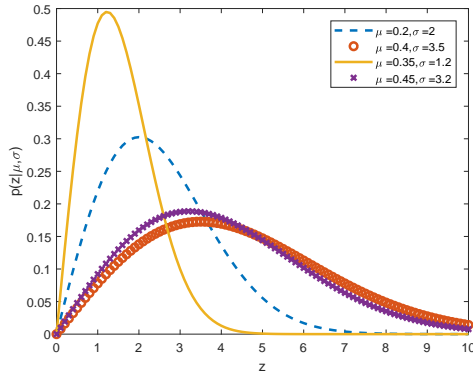


**Figure 1.7** Rician PDF with various values of  $\mu$  and  $\sigma$ .

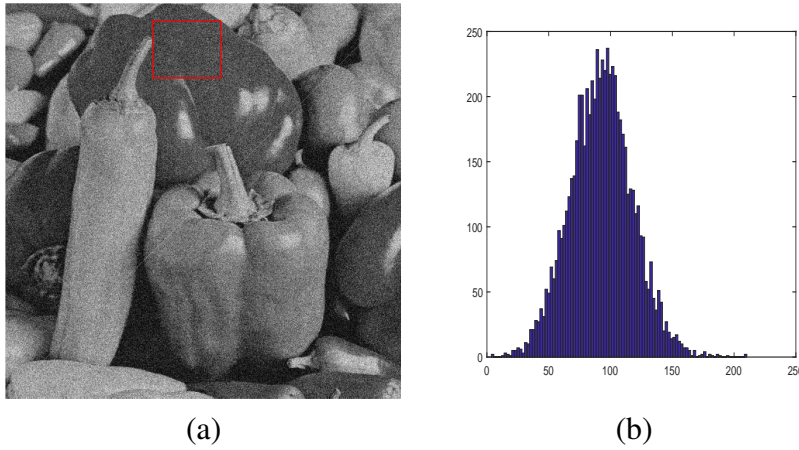


**Figure 1.8** (a)“Peppers” image corrupted by Rician noise, (b) histogram of highlighted area in (a).

earlier, Rician noise is common in magnitude MR data, where the data is formed in the complex domain <sup>1</sup>. PDFs of Rician distribution with various values of  $\sigma$  and  $\mu$  are given in Figure 1.7. Peppers image corrupted with a Rician distributed noise and the histogram of the homogeneous area in this image are shown in Figures 1.8(a) and 1.8(b) respectively.

Furthermore, the Poisson PDF is given by,

$$P(z|\sigma) = \frac{e^{-\sigma} \sigma^z}{z!}, \quad (1.18)$$

where  $z \geq 0$  and  $\sigma$  is the standard deviation. Microscopic images (such as confocal and

<sup>1</sup>The noise in each (real and imaginary) plane is additive Gaussian, however, the noise in the magnitude data formed by squaring and adding each plane is found to be Rice distributed.

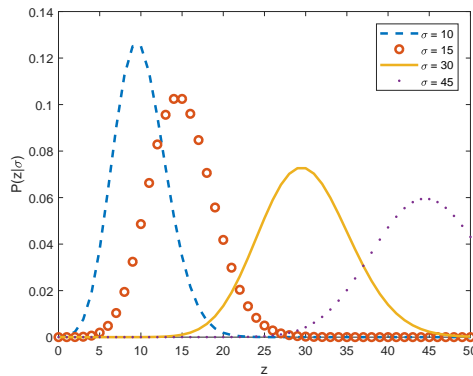


**Figure 1.9** Poisson PDF with various values of  $\sigma$ .

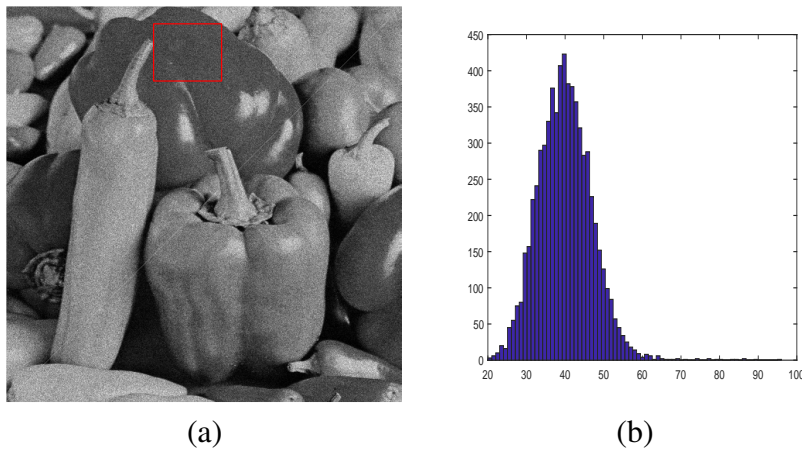


**Figure 1.10** (a) “Peppers” image corrupted by Poisson noise, (b) histogram of highlighted area in (a).

fluorescence), hyperspectral, multispectral and telescopic images are commonly corrupted by Poisson noise<sup>2</sup> (see Kervrann and Trubuil (2004); Liu et al. (2017); Mansouri et al. (2016) for more details). Poisson PDFs for different values of  $\sigma$  are given in Figure 1.9. Histogram of the selected homogeneous area from the Poissonian image shown in Figure 1.10(a) is given in Figure 1.10(b).

Once the degradation is modeled properly, the next task involves recovering the original image from the distorted observation using these degradation statistics. The next section gives a bird’s eye view of most popular image restoration methods from the literature.

<sup>2</sup>As these images are generally formed as a result of a Poisson process.



## 1.4 BRIEF HISTORY OF IMAGE RESTORATION PROBLEM

Image restoration is a classical image processing problem in the literature. The image restoration started ever since digital images started dominating the imaging applications (Gonzalez and Woods (2006)). Most imaging applications acquire images under various imaging conditions. The acquired data is apparently distorted in most imaging applications. The data representation differs with reference to the application under consideration. Nevertheless, the distortion or degradation is observed to follow a certain pattern. The major causes of distortion are noise and device artifacts (Gunturk and Li (2012)). The noise intervention happens during the acquisition stage or transmission of the data. The noisy features are random fluctuations that disturb the data. Since they are random, their probability follows different distributions. The common distributions found in the imaging literature are already discussed earlier in this thesis. The noise distribution changes with the conditions under which the images are captured. The medical imaging systems are prone to various kinds of noises. The common ones among them are Gamma (Aubert and Aujol (2008)), Poisson (Zhu et al. (2012)) and Rayleigh (Mäkitalo et al. (2010)). The distortions are mainly due to the improper reflection of the signals used to probe the details of the subject. For instance, the ultrasound imaging is prone to speckles, as the sound wave gets reflected and transmitted upon hitting the object (Abbott and Thurstone (1979)). The final images formed are generally noisy due to the improper interference of the signals sent to probe the data and many times they are received out of phase at the sensors. Similar conditions arise in the other kinds of applications such as satellite imaging. In satellite imaging, the images are captured by devices located at large distances from the object (Porcello et al. (1976)). Therefore, the signal sent to probe the data gets reflected or deviated from the desired path while transmitting through a medium. Moreover, distortions can also be caused due to the improper functioning of the devices used for capturing the data. The device artefacts cause distortions in the data (such as blurriness) which gets combined with the noise resulting in a tedious restoration process.

One of these major issues with the degradation is that it results in different kinds of distortions. Therefore, a common method becomes inadequate to handle them properly.

Therefore, many methods have been proposed for restoring images from different kinds of distortions.

## 1.5 SOLUTION TO AN IMAGE DEGRADATION PROBLEM

Modeling the degradation process has already been discussed in previous sections. Now the subsequent step deals with solving the model thus designed. There have been a plethora of restoration models for restoring data uncorrelated noise distributions such as additive Gaussian, salt and pepper (also called as impulse noise), etc. Mean filter (Gonzalez and Woods (2006)) replaces each pixel in the noisy image by the average of the neighborhood (also known as a patch) pixels. Here, as the size of the patch increases, the degree of smoothness also increases in the restored version of the image. This filter performs better for a low density additive Gaussian distributed noise. Salt and pepper noise shall be removed using the median filter which replaces each pixel in the target image by the median of pixel values of the patch around it. Here, the patch is reshaped into a one dimensional array with  $N$  elements and sorted (in ascending order). The element in the position:  $(N + 1)/2$  of the sorted array replaces the center pixel in each patch. Some of the advanced averaging filters such as non-local means (Buades et al. (2005)), block matching collaborative filter (Dabov et al. (2007)) replaces each target patch by the average of similar patches in a search window. The data independent nature of additive Gaussian noise makes the restoration easier. But under data-dependent noise distribution, the restoration process is more challenging. There are a few proposals toward restoring images from such distortions as well, see Makitalo and Foi (2013a); Foi (2011); Fernandez and Lopez (2006), for the details.

As discussed in the beginning, we deal with the restoration of images, considering it as an inverse problem. The ability of the Bayesian approach over the penalization theory for a better approximation of the data of interest makes it a suitable choice for solving the image restoration problem. In the Bayesian approach, the problem is reformulated as an energy minimization problem using a MAP estimation technique and further solved under a variational framework, see Le et al. (2007); Aubert and Aujol (2008) for details.

### 1.5.1 Variational methods

Calculus of variation is used to state the problem of finding a function's integral which is maximum or minimum for a certain value, which is similar to the extrema (see Gelfand and Fomin (1963), Jost and Li Jost (1998) for the details). The integral is also known as a functional. These functionals include functions and their derivatives. One straightforward example for such a problem is finding a curve that joins two points such that the length of the curve is as shortest as possible. If there are no conditions, then the solution would be the straight line joining the two points. If there is a condition such as the two points are on some surface in the hyperplane, then the surface need not be flat. So, there can be many other solutions. These solutions are called geodesics. We can find the extrema of a functional by finding the maxima or minima of the associated function. This is done by finding the points where the derivative of the function vanishes, which is usually performed using the Euler-Lagrange (E-L) derivatives (see Appendix-A.2 for more details).

A general variational framework in terms of energy formulation can be written as

$$\min_u \phi(u) \quad \text{subject to } H(u),$$

where  $\phi(u)$  is the objective function and  $H(u)$  is the constraint. In a general, basis pursuit problem of  $Ku = u_0$ , the problem is an unconstrained problem or it has infinitely many solutions. So the goal is to find the approximate solution or probable optimal solution. The solution is sought under a minimization framework where the  $L_1$  norm of  $u$  should be minimized subject to the constraints to be defined, i.e,

$$\min_{u \in R^n} \|u\|_1 \quad \text{subject to } Ku - u_0 = 0. \quad (1.19)$$

By relaxing the constraints, we can form an unconstrained minimization problem, that is,

$$\min_{u_0 \in L^2, u \in R^n} \|u\|_1 + \lambda \|Ku - u_0\|_2^2. \quad (1.20)$$

Here  $L^2$  norm is taken under the assumption that  $u_0$ , the observed data is in  $L^2(\Omega)$  and residue should be smooth. In the similar lines, we can form image denoising problem, where the degradation model is  $u_0 = u + n$ . Here we assume that  $u$  belong to the space of bounded variation ( $BV(\Omega)$ ), where the Total Variation ( $TV(u) = \int_{\Omega} \|\nabla u\|_2 dx dy$ ) is

bounded. Now the constrained minimization problem is,

$$\min_{u \in BV(\Omega)} \|u\|_{BV} \quad \text{subject to} \quad \|u - u_0\|_2^2 = |\Omega|\sigma^2, \quad (1.21)$$

where  $|\Omega|$  represents the total pixel count in the image. The above problem can be made unconstrained by formulating as given below,

$$\min_{u_0 \in L^2(\Omega), u \in BV(\Omega)} \|u\|_{BV} + \lambda \|u - u_0\|_2^2 - |\Omega|\sigma^2. \quad (1.22)$$

Generally the energy minimization problem is stated as,

$$E_{total} = E_{Smoothness}(u) + \lambda E_{Fidelity}(u, u_0). \quad (1.23)$$

The smoothness term involves derivatives of  $L_p$  norm, which is also called as the regularization term. The data fidelity term controls the smoothness of the data by adding back the lost details in the minimization process.  $\lambda$  represents the regularization parameter. The functional of  $E_{Smoothness}(u)$  can be stated as (see Gilboa (2018) for more details):

$$F(u) = \int_{\Omega} f(x, u(x), \nabla u(x)) dx, \quad (1.24)$$

where  $f(x, u(x), \nabla u(x)) \in \mathbb{R}^n$ ,  $x = (x_1, x_2, \dots, x_n)$ . For the regularization, we are concerned with derivatives of  $u$ , thus we can have a simplified formulation of the problem.

Let  $J(u)$  be regularization functional, defined as:

$$J(u) = \int_{\Omega} \phi(|\nabla u(x)|) dx, \quad (1.25)$$

where  $\phi(u)$  is a function of norm of  $u$ . Further, the E-L of the functional (1.25) is

$$\partial_u J(u) = -div \left( \frac{\phi'(|\nabla u|)}{|\nabla u|} \nabla u \right). \quad (1.26)$$

The gradient descent marching with artificial time  $t$  is applied on above equation with the following conditions,

- Neumann boundary condition :  $\partial u / \partial N = 0$  on  $\partial \Omega$ .
- Initial condition :  $u(0, x, y) = u_0(x, y)$ .

The above boundary and initial conditions are assumed for all PDEs described in this thesis unless defined otherwise. The gradient descent solution is given by

$$u_t = -\partial_u J(u) = div \left( \frac{\phi'(|\nabla u|)}{|\nabla u|} \nabla u \right), t \geq 0, (x, y) \in \mathbb{R}^2. \quad (1.27)$$

In the next section, the derivation of an energy functional using a MAP estimation is detailed.

## 1.5.2 Deriving variational model using the MAP estimator

Consider the most common additive noise model given in (1.12). Let us opt for the Bayesian methodology to solve this inverse problem, for that, one has to first model the degradation process. The noise distribution assumed is given by (1.13). Using the Bayesian theory we can redefine (1.13) with original ( $u$ ) and noisy observation( $u_0$ ) as,

$$P(u_0|u) = \frac{1}{\sigma\sqrt{2\pi}} e^{-\frac{(u_0-u)^2}{2\sigma^2}}, \quad (1.28)$$

where  $P(u_0|u)$  is the conditional probability of  $u_0$  given  $u$ . It is also the likelihood estimate of the distribution. Now let us apply Bayes rule given in (1.5) to the above equation, which leads to,

$$P(u|u_0) = \frac{P(u_0|u)P(u)}{P(u_0)}. \quad (1.29)$$

The next step is to maximize the posterior probability  $P(u|u_0)$ . Here  $P(u_0)$  is a constant and does not affect the minimization step, therefore it is omitted from the further steps.

The maximization problem after substituting likelihood estimation of  $P(u_0|u)$  is,

$$\max_u \{P(u|u_0)\} = \max_u \left\{ \frac{1}{\sigma\sqrt{2\pi}} e^{-\frac{(u_0-u)^2}{2\sigma^2}} P(u) \right\}. \quad (1.30)$$

where  $P(u)$  is the prior probability. Next, we apply a negative log transform on both sides of the above equation, which modifies the maximization problem into a minimization problem i.e.,

$$\min_u \{-\log(P(u|u_0))\} = \min_u \left\{ -\log \left( \frac{1}{\sigma\sqrt{2\pi}} \right) + \frac{(u_0-u)^2}{2\sigma^2} - \log(P(u)) \right\}. \quad (1.31)$$

For the sake of simplicity, omit  $-\log$  from the left hand side and constant terms on the right hand side of the above equation and simplify, to get,

$$\min_u \{P(u|u_0)\} = \min_u \left\{ (u_0-u)^2 - \log(P(u)) \right\}. \quad (1.32)$$

Now let us consider prior probability  $P(u) = e^{-\frac{\lambda}{2}J(u)}$  (the Gibb's prior), where  $J(\cdot)$  is the regularization prior (defined in the previous section) and  $\lambda$  is the regularization parameter. Further, reformulating the above equation as an energy minimization problem  $E(u)$  (and also considering linear blur  $K$ ) yields,

$$E(u) = \min_u \left\{ \int_{\Omega} (u_0 - Ku)^2 dx dy + \frac{\lambda}{2} J(u) \right\}, \quad (1.33)$$

where  $\Omega$  is the image domain. The above minimization problem yields the restored version of the image for an appropriately chosen regularization prior, such as  $J(u) = TV(u)$ , which is well known as total variation regularization. Further, the problem is numerically solved using artificial time marching scheme (or gradient descent scheme).

Though the gradient descent solver is trivial, it takes a large number of iterations to converge to the solution and the solution in each iteration depends on the regularization parameter  $\lambda$  as well as the time step. In order to overcome such drawbacks, one can opt for the fast solvers such as augmented Lagrangian (Chan et al. (2011)), primal-dual (Zhu and Chan (2008)), forward backward splitting (Combettes and Wajs (2005)), Chambolle projection (Chambolle and Pock (2010)) scheme, split-Bregman (Goldstein et al. (2010)) iterative approach etc. The split-Bregman approach has been employed in this thesis for solving the proposed models, since it converges faster and moreover, the convergence is less sensitive to the parameters used therein. The next section gives a brief survey on some of the variational approaches.

### 1.5.3 Review of the variational models

Tikhonov regularization (Tikhonov and Arsenin (1977)) is one of the pioneer approaches for solving an ill-posed problem. The regularization prior  $\phi(u)$  in the Tikhonov regularization takes the form,  $\phi(u) = |\nabla u|^2$ . Hence, the energy functional in 1.33 changes to,

$$E(u) = \min_u \int_{\Omega} \left\{ (u_0 - Ku)^2 + \frac{\lambda}{2} |\nabla u|^2 \right\} du. \quad (1.34)$$

The E-L formulation of the above equation is given by,

$$-\Delta u - \lambda K^*(u_0 - Ku) = 0, \quad (1.35)$$

where  $\Delta$  represents Laplacian operator and  $K^*$  is the adjoint of  $K$ . Above equation can be solved using gradient descent scheme. The diffusion process in the Tikhonov method is effective but edges and fine details are penalized extensively during the process. Motivated by the Tikhonov method, Rudin et al. (1992) proposed a restoration model that performs well in restoring images and known as total variation regularization. Here,  $\phi(u) = \|\nabla u\|_2$ ,  $u \in BV(\Omega)$ , total variation is represented as  $TV(u)$ , which is given by

$$TV(u) = \int_{\Omega} \|\nabla u\|_2 \, dx dy.$$

Thus, the energy functional in case of TV takes the form,

$$E(u) = \min_u \int_{\Omega} \left\{ (u_0 - Ku)^2 + \frac{\lambda}{2} \|\nabla u\|_2 \right\} dx dy. \quad (1.36)$$

Applying E-L equation on 1.36 we get,

$$-div \left( \frac{\nabla u}{|\nabla u|} \right) - \lambda K^*(u_0 - Ku) = 0. \quad (1.37)$$

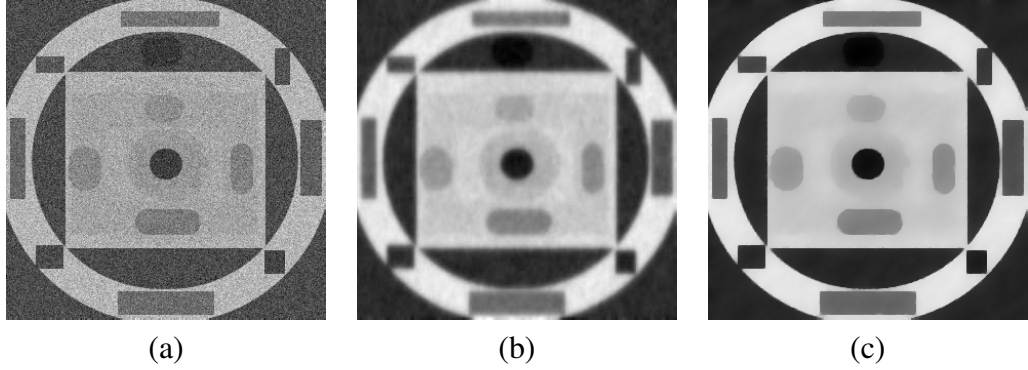


**Figure 1.11** (a) Test image corrupted by the Gaussian noise of variance 35, restored using (b) Tikhonov regularization (150 iterations) (c)TV regularization (200 iterations).

The solution for the above equation is sought as in the previous case. In homogeneous regions where  $|\nabla u| \approx 0$ ,  $1/|\nabla u|$  is unbounded, hence the smoothing is more. Near the edges where  $|\nabla u| \rightarrow \infty$ ,  $1/|\nabla u|$  vanishes and the diffusion gets stopped. The selection of smaller time step in the gradient descent evaluation leads to a stable solution. Hence, the restoration process needs a larger number of iterations to converge. Tested results of TV and Tikhonov restoration are shown in Figure 1.11. The denoising and edge preserving capability of the model is evident in this figure.

Many variants of TV model are available in the literature, some prominent ones are highlighted subsequently. The anisotropic TV takes the function  $\phi(u) = |\partial u/\partial x + \partial u/\partial y|$  (Esedoglu and Osher (2004)), where  $x$  and  $y$  are the directions of the derivative. The  $L^1$  norm regularizer has been implemented in Alliney (1992) for controlling the smoothness relatively better. Kuijper (2007) proposed a p-Laplacian driven restoration model, here, the function  $\phi(\cdot)$  is defined as  $\phi(u) = \|\nabla u\|_p^p$ . Marquina and Osher (2000) introduced a gradient descent model based on level set motion for noise removal. For all these TV variants, numerical implementation is done by using finite difference schemes, explained below. Let us consider two dimensional image  $u$  and define the partial derivative using the central differencing scheme (with  $h$  as the pixel difference, which is usually considered as one) as follows,

$$\frac{\partial u}{\partial x} = \frac{u_{x+1,y} - u_{x-1,y}}{2h}, \quad (1.38)$$

and

$$\frac{\partial u}{\partial y} = \frac{u_{x,y+1} - u_{x,y-1}}{2h}. \quad (1.39)$$

Using (1.38) and (1.39) the numerical implementation of the gradient operator  $\nabla$  for image  $u$  can be derived as,

$$\nabla u = \begin{bmatrix} \frac{\partial u}{\partial x} & \frac{\partial u}{\partial y} \end{bmatrix}.$$

Divergence operator  $\nabla \cdot$  or  $div$  is defined as,

$$div(\nabla u) = \begin{bmatrix} \frac{\partial}{\partial x} & \frac{\partial}{\partial y} \end{bmatrix}' \begin{bmatrix} \frac{\partial u}{\partial x} & \frac{\partial u}{\partial y} \end{bmatrix},$$

which leads to,

$$div(\nabla u) = \frac{\partial^2 u}{\partial x^2} + \frac{\partial^2 u}{\partial y^2} = \Delta u.$$

### 1.5.4 Nonlocal methods

Unlike the image filtering methods which replaces the pixels with the average of their neighborhood, non-local methods select similar patches in a predefined image domain and perform averaging (Non-Local Means (NLM) by Buades et al. (2005)) or thresholding (Block Matching 3D (BM3D) filtering by Dabov et al. (2007)) and replace the filtered patches back on the respective indices. Here we discuss the basic formulation of non-local variational framework (based on TV-norm) proposed by Gilboa and Osher (2008). The TV non-local variants (Azzari and Foi (2014)) are formally designed to handle additive data independent noise with Gaussian PDF. The Non-Local TV (NLTV) methods performs well (in terms of local details preservation) compared to the ordinary TV variants. The non-local averaging filter introduced in Buades et al. (2005) is

$$NL(u(x)) = \frac{1}{c(x)} \int_{\Omega} e^{-d_{\sigma}(u(x),u(y))/h^2} u(y) dy, \quad (1.40)$$

where  $x, y \in \Omega$ ,  $h$  is the space step and

$$d_{\sigma}(u(x),u(y)) \triangleq \int_{\Omega} G_{\sigma}(t') |u(x+t') - u(y+t')|^2 dt', \quad (1.41)$$

where  $t'$  is the distance from the center pixel (usually half of the size of a patch),  $G_{\sigma}$  is the Gaussian kernel  $\left( G_{\sigma} \triangleq \frac{1}{2\pi\sigma^2} e^{-\frac{(x^2+y^2)}{2\sigma^2}} \right)$  with standard deviation  $\sigma$  and

$$c(x) \triangleq \int_{\Omega} e^{-d_{\sigma}(u(x),u(y))/h^2} dy, \quad (1.42)$$

hereafter we consider  $h = 1$ . Now let us define the weight matrix  $w(x,y) = d_{\sigma}(x,y)^{-2}$  which is a symmetric matrix. Define the non-local gradient as:

$$\nabla_{NL} u(x,y) = (u(y) - u(x)) \sqrt{w(x,y)}. \quad (1.43)$$



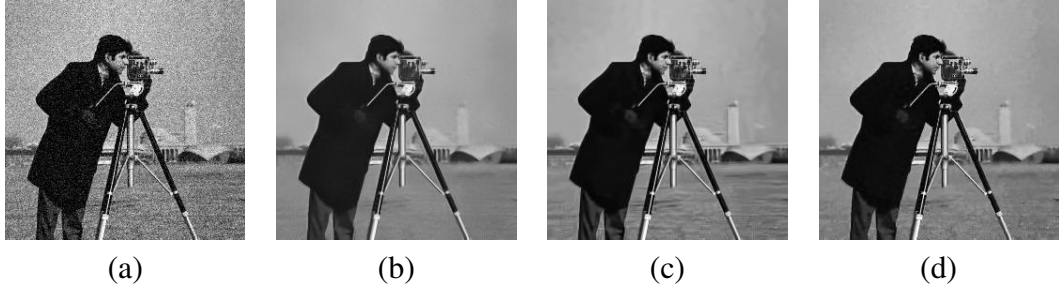


**Figure 1.12** (a) Noisy image (additive Gaussian with variance = 25), restored with (b) Nonlocal means, (c) BM3D and (d) Nonlocal TV.

Further defining the Laplacian as a weighted graph  $G = (V, E)$ , with  $V$  as a finite set of vertices and  $E$  as finite set of edges, we have

$$\Delta_{NL}(u(k)) = \sum_{l \in \mathcal{N}_k} w(k, l)(u(l) - u(k)), \quad (1.44)$$

where  $k, l \in V$  and  $\mathcal{N}_k$  is the local neighborhood of  $k$  (or set of nodes with edges connected to  $k$ ). Now let us describe the NLTV as

$$E(u, u_0, \lambda) = J_{NLTV}(u) + \frac{\lambda}{2} (\|Ku - u_0\|_{L^2}^2 - |\Omega|\sigma^2), \quad (1.45)$$

$J_{NLTV}(u)$  is defined as

$$\begin{aligned} J_{NLTV}(u) &= \int_{\Omega \times \Omega} \phi(|\nabla_{NL}u|^2) dx dy, \\ &= \int_{\Omega} \phi \left( \int_{\Omega} (u(y) - u(x))^2 w(x, y) dy \right) dx. \end{aligned} \quad (1.46)$$

The Euler-derivative of  $J_{NLTV}(u)$  with respect to  $u$  is

$$J'(u) = -2\nabla \cdot (\nabla_{NL}u \phi'(|\nabla_{NL}u|^2(x))), \quad (1.47)$$

The gradient descent/artificial time marching solution of NLTV for an additive Gaussian noise and linear blur, amounts to

$$\begin{aligned} u_{n+1} &= u_n + \Delta t [-2\nabla_{NL} \cdot (\nabla_{NL}u \phi'(|\nabla_{NL}u|^2(x))) \\ &\quad + \lambda K^*(Ku - u_0)]. \end{aligned} \quad (1.48)$$

The restoration results using various non-local variants are demonstrated in Figure 1.12.

Image restoration under a data independent Gaussian noise distribution has been discussed in detail in the preceding sections. Many of these approaches have also been extended to the data-correlated noise scenarios as well, see for instance: TV variant, for Poisson denoising by Le et al. (2007), for Gamma restoration by Aubert and Aujol (2008), for restoring MR images corrupted by Rician noise (Liu et al. (2015)). How-

ever, in case of data-dependent noise, proper analysis of distortion should be done and an efficient regularizer should be selected to get better results. Most of the proposed schemes under data-correlated noise models lag such elaborative analysis.

## 1.6 PROS AND CONS OF EXISTING VARIATIONAL MODELS

Many variational methods have been proposed for restoring images based on different degradation models described in the literature. Nevertheless, they have their own pros and cons. A brief description of various restoration models under the variational framework and their pros and cons are detailed in the table shown below.

<b>Model Name, Authers and Year</b>	<b>Pros</b>	<b>Cons</b>
Perona and Malik (Perona and Malik (1990))	<ol style="list-style-type: none"> <li>1. Better removal of noise in homogeneous area.</li> <li>2. Smoothing can be controlled using the diffusion coefficient.</li> </ol>	<ol style="list-style-type: none"> <li>1. Fails in well and preservation of sharp edges and fine details.</li> <li>2. Noise distribution is not being considered.</li> </ol>
Total Variation (Rudin et al. (1992))	<ol style="list-style-type: none"> <li>1. Better preservation of sharp edges.</li> <li>2. The fidelity term helps in retaining lost details.</li> </ol>	<ol style="list-style-type: none"> <li>1. Smooths out some of the fine structures.</li> <li>2. Diffusion process dependent on the regularization parameter.</li> <li>3. Smooth areas are transformed into piecewise constant regions (staircase effect).</li> </ol>
Mean Curvature Motion (Marquina and Osher (2000))	<ol style="list-style-type: none"> <li>1. Reaches the steady state solution quickly compared to the TV.</li> <li>2. The staircase effects are solved.</li> </ol>	<ol style="list-style-type: none"> <li>1. Smooths out some edges and fine details.</li> <li>2. Uses gradient descent scheme</li> </ol>
Non-local Total Variation (Gilboa and Osher (2008))	<ol style="list-style-type: none"> <li>1. Efficient in texture preserving.</li> <li>2. Non-local restoration methods give better approximation to the desired data.</li> </ol>	<ol style="list-style-type: none"> <li>1. Diffusion process dependent on the regularization parameter.</li> <li>2. Low convergence rate.</li> <li>3. Designed to handle data independent noise.</li> </ol>
Aubert and Aujol (Aubert and Aujol (2008))	<ol style="list-style-type: none"> <li>1. Smooths out data-dependent gamma noise.</li> <li>2. Noise distribution took into consideration.</li> </ol>	<ol style="list-style-type: none"> <li>1. Staircase effect remains.</li> <li>2. Low convergence rate.</li> </ol>
TV Poisson (Le et al. (2007))	<ol style="list-style-type: none"> <li>1. Data-dependent Poisson noise is being removed.</li> <li>2. Model being derived using the noise PDF, which produces better result.</li> </ol>	<ol style="list-style-type: none"> <li>1. Dependent on regularization parameter.</li> <li>2. Low convergence rate.</li> </ol>

## 1.7 MOTIVATION OF THE RESEARCH

Restoring images from data-correlated noise setup is a challenging task, as the noise is a function of data itself. Since restoration is an inverse and ill-posed problem, an accurate approximation to the original data is highly challenging. Though there are some studies relating to the data-dependent noise distortions, still there are further scopes for thoroughly analyzing the models and devising more improvised models to handle such degradation scenarios. Unlike the data-independent noise restoration models, data-dependent models are not analyzed quite extensively in terms of their theoretical and practical aspects. Most of the real-life imaging systems are found to produce data-correlated noise distributions, so handling such distortions is the need of the hour. Data-correlated multiplicative and additive noise models (following Rayleigh and Rice noise distribution, respectively) are being assumed in most of the medical and satellite imaging applications. Medical X-ray, CT and PET images, microscopic (confocal and fluorescence) and telescopic images are said to be contaminated by data-dependent Poisson noise. It is essential to improvise these models in terms of the detail preservation (viz. textures and fine-details) and faster convergence so as to put them in place in a real-time image restoration system.

This thesis is structured towards the restoration of different data-dependent noise distortions which are common in several important imaging fields such as medical and satellite imaging. For the proper diagnosis and analysis in these fields, the images should be restored efficiently. The Bayesian theory has been used in this work to solve the image restoration problem since it can efficiently approximate the solution.

## 1.8 PERFORMANCE MEASURES

The qualitative analysis has to be done to ensure the restoration capability of the model. Visual and qualitative together determines the performance of the restoration technique. There have been several approaches which are used to measure the quality of the resultant image for instance Signal to Noise Ratio (SNR), which calculates the noise removal capability of the restoration model. Most of the quality metrics need the noiseless image to calculate the performance. This section gives the details of the quality metrics

used in this thesis.

1. Signal to Noise Ratio: Calculates the noise removal capacity of the restoration model. The high value of SNR represents the high noise removal capability of the model, but sometimes causes the over-smoothing. SNR is calculated as given in the equation below,

$$SNR(u, \hat{u}) = 10 \log_{10} \left( \frac{\sum_i \sum_j u(i, j)^2}{\sum_i \sum_j (u(i, j) - \hat{u}(i, j))^2} \right), \quad (1.49)$$

where  $u$  can be an output or a noisy image,  $\hat{u}$  is the original or reference image.

2. Mean Squared Error (MSE): Calculates the error between the original and an estimated data. The resultant value is always non-negative. The value close to zero represents better whereas higher value results in poor estimation.

$$MSE(u, \hat{u}) = \frac{1}{|\Omega|} \int_{\Omega} (\hat{u} - u)^2 dx, \quad (1.50)$$

where  $\Omega$  represents image domain and  $|\Omega|$  stands for the number of pixels in discrete domain.

3. Peak Signal to Noise Ratio (PSNR): Gives a real positive value as long as MSE is smaller than  $\max(\hat{u})^2$ , higher the value is better the signal preservation capability of the model under consideration. MSE and PSNR are inverse to each other, as one increases the other one decreases.

$$PSNR(u, \hat{u}) = 10 \log_{10} \left( \frac{\max(\hat{u})^2}{MSE(u, \hat{u})} \right). \quad (1.51)$$

4. Structural Similarity Index Measure (SSIM) (Wang et al. (2004)): Measures structure preservation capability of the restoration model. High SSIM (in the range of 0 to 1) shows high structure preserving ability of the restoration model. SSIM is defined as follows,

$$SSIM(u, \hat{u}) = \frac{(2\mu_u \mu_{\hat{u}} + c_1)(2\sigma_{u\hat{u}} + c_2)}{(\mu_u^2 + \mu_{\hat{u}}^2 + c_1)(\sigma_u^2 + \sigma_{\hat{u}}^2 + c_2)}, \quad (1.52)$$

where  $\mu_u$  and  $\mu_{\hat{u}}$  are the averages of  $u$  and  $\hat{u}$  respectively,  $\sigma_u$  and  $\sigma_{\hat{u}}$  are the variances of  $u$  and  $\hat{u}$ .  $\sigma_{u\hat{u}}$  is the co-variance of  $u$  and  $\hat{u}$ .  $c_1 = (k_1 L)^2$  and  $c_2 = (k_2 L)^2$  are two variables to stabilize the division with the weak denominator,  $L$  is the dynamic range of the pixel values and  $k_1 = 0.01$ ,  $k_2 = 0.02$  by default.

## 1.9 RESEARCH OBJECTIVES

The complete recovery of an image from a distorted observation is not practically feasible. Also, the solution is dependent on the initial data. Hence the problem is an ill-posed inverse problem in its actual form. There have been several approaches proposed to get an approximated solution to the ill-posed problems. Theory such as penalization does the error minimization to get a better approximation, but it does not care about the degradation models in general. Bayesian theory models the degradation as a probabilistic approach and by using the prior information, the posterior probability is maximized (using MAP estimator) to get a much better approximation for the desired data. So the primary goal of this thesis work is to mathematically model the data-dependent degradation in the real-life imaging scenarios. Once the perturbation is properly modeled, the next step is to choose a relevant approach to solve it. Since we deal with the variational framework, energy minimization functional has to be defined. The functional should feature both regularization as well as data fidelity aspects. The regularizer reduces the fluctuations in an image (due to noise) by smoothing the homogeneous areas, whereas data fidelity controls the smoothing process by adding back the lost details. The overall objectives can be summarized as follows:

- To devise variational frameworks to handle data-correlated noise distributions and analyze them thoroughly in terms of theoretical and practical aspects.
- To tune the regularization and data-fidelity terms so as to handle the data-correlated noise distributions such as Chi, Rayleigh, and Poisson, while preserving important information (like textures, edges and finer details) present in the data which are essential for further analysis and diagnosis.
- Fine-tune the models to make it adaptive and less sensitive to the input noise parameters so as to yield the optimal solutions.
- Improving the convergence rate by modeling them using the faster numerical approaches in order to fit them in a real-time restoration scenario. And also to yield stable solutions which are independent of the chosen time step and regularization parameters.

- Analyzing the performance (qualitatively and quantitatively) and comparing it with the state of the art restoration models using real time models in medical and satellite imaging applications.

## **1.10 ORGANIZATION AND CONTRIBUTIONS OF THE THESIS**

The remaining chapters in this thesis are organized as follows:

### **Chapter 2: Nonlocal Total Bounded Variation approach to restore multiple-coil MRI data**

In this chapter, a variational model is proposed for restoring multiple-coil magnetic resonance images (MRI) corrupted by non-central *Chi* distributed noise. The energy functional corresponding to the restoration problem is derived using the maximum a posteriori (MAP) estimator. The non-local total bounded variation prior is being used as the regularization term in the functional derived using the MAP estimation process. Further, the split-Bregman iteration scheme is being followed for fast numerical computation of the model.

### **Chapter 3: Nonlocal Total Variational Restoration Models for Restoring Rayleigh data**

Restoration of images corrupted by data-correlated Rayleigh noise distribution has not been studied much extensively in the literature, unlike the other noise distributions. In this chapter, the degradation analysis is done on data-correlated Rayleigh noise and a linear blurring artifact. Further, a variance stabilization approach and two variational approaches for restoring images from their noisy and blurred observations have been introduced. The split-Bregman iterative scheme is used for numerically solving the models to improve their convergence rates. Furthermore, non-local total variation and non-local total bounded variation priors are being used as regularizers in these models to improve their restoration efficiency.

## **Chapter 4: Nonlocal variational approach to restore Poissonian images**

Poisson noise (also known as shot or photon noise) arises due to the lack of information during the image acquisition phase, it is quite common in the field of microscopic or astronomical imaging applications. In this chapter, a non-local total variation regularization framework has been proposed with a  $p$ -norm driven data-fidelity for denoising Poissonian images. In precise, the energy functional is derived using a Maximum A Posteriori (MAP) estimator of the Poisson probability density function (PDF). The diffusion amounts to a non-local total variation minimization process, which eventually preserves fine structures while denoising the data. The numerical solution is sought under a fast converging split-Bregman iterative scheme.

## **Chapter 5: Conclusions and Future Directions**

This chapter contains the conclusions about the proposed schemes and avenues of future research. Since the image restoration is an ill-posed problem, the obtained result will always be an approximation to the original image. As the outcome of the restoration is close to the original data, further analysis becomes easy and accurate. Since the image restoration is one of the most important tasks in image processing, there is always a need for a better restoration algorithm. Adoption of fast solvers improves the efficiency of the model, thus extends their software portability.

## **Appendix**

Some of the mathematical definitions, derivations and sample MATLAB codes used for the implementation are included in this section for improving the readability of the thesis and to ensure its completeness.





## Chapter 2

# NONLOCAL TOTAL BOUNDED VARIATION APPROACH TO RESTORE MULTIPLE-COIL MRI DATA

### 2.1 INTRODUCTION

The main intention of image restoration is to extract the original image from the given noisy image. The target image is assumed to be degraded by some degradation phenomenon. So, the restoration techniques are oriented toward modeling the noise phenomena and applying one of the recovering processes to restore the original image. The additive noise which follows a Gaussian distribution is a widely appearing degradation in the literature. An active imaging system such as medical CT, MRI, ultrasound, satellite etc is found to be corrupted by data-correlated noise. Performing image restoration of such images without considering the noise distribution will cause over smoothing, which subsequently leads to data loss. Ill-posedness of the restoration problem is caused due to the non-existence of the unique solution or the continuous dependence of the restored data on the initial data. The variational formulation is one of the widely used regularization techniques to solve such ill-posed problems, which has already been discussed in the previous chapter.

In most of the medical image modalities, it is observed that the noise is source dependent, say for instance, MR imaging. This chapter mainly focuses on removing data-correlated noise from MR images which follows either a Rician or a non-central *Chi* distribution. The variational formulation is being derived considering the noise

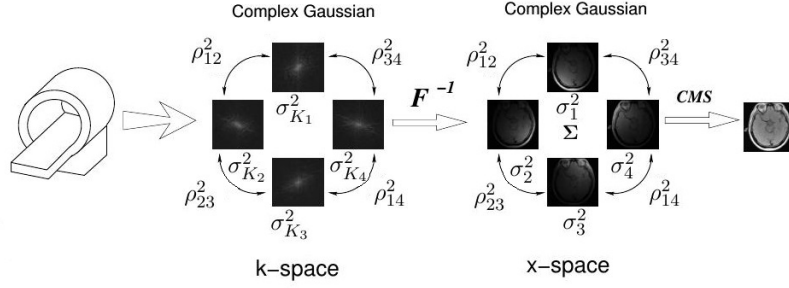


**Figure 2.1** MRI formation from the k-space for multiple-coil setup (courtesy: Fernandez and Vega (2013)). Here each  $\rho_{i,j}$  denotes correlation coefficient,  $\sigma$  denotes the covariance,  $\Sigma$  stands for the covariance matrix,  $F^{-1}$  is the inverse Fourier Transform and CMS is expanded as the composite magnitude signal.

distribution present in the data using the MAP estimator. Two degradation scenarios are being considered in this chapter, they are,

- **Case 1:** Image with noise and without blur (operator  $K$  is set as identity)
- **Case 2:** Image with both noise and linear shift-invariant blur.

Optimizing the functionals for both these cases yield solutions, which correspond to the restored versions of the noisy images. The non-local total bounded variation prior is being used as the regularization term in the functional derived using the MAP estimation process. Further, the split-Bregman iteration scheme is being followed for fast numerical computation of the model. The results are compared with the state of the art MRI restoration models using visual representations and statistical measures.

Medical MRI has become the state of the art non-invasive imaging technique for prompt diagnosis of disorders in the human body. MR Images are usually high-contrast images formed in a complex domain. The image formation is given in Figure 2.1.

## 2.2 NOISE FORMULATION

MR images are formed in the spatio-frequency domain (also called as the k-space) contain real and imaginary components. The points in the k-space (a complex space, where the image is formed (Fernandez and Vega (2013))) measured from MRI scanners are

thus independent samples of the radio frequency signal received by each coil. The data in this complex domain will be affected by random thermal fluctuations which are uniform and independent of the frequency components. So these thermal fluctuations can be considered as additive white Gaussian noise with variance  $\sigma_n^2$ . These random fluctuations will affect both real and imaginary components of the k-space image (on each slice at each coil). The desired MR image is thus formed by applying linear inverse Discrete Fourier Transform (iDFT) on the k-space data. Since the Fourier transform and its inverse are linear and unitary, the noise in the image is still the additive Gaussian. Now the final magnitude MR image is obtained by taking the Composite Magnitude of the complex Signal/image (CMS). In this image, the noise distribution gets modified because the magnitude function is non-linear. So the image contains transformed noise, which is data-dependent and it is generally Rician distributed (Fernandez et al. (2009)). In case of the multiple-coil setup, the image is generated by taking the square root of the sum of the magnitudes of the complex data over all the gradient coils. Therefore, the data independent Gaussian noise added in the real and imaginary components of the complex MR data also gets squared and added and finally, the square-root of this data gives the final magnitude MR image. The noise pattern in the complex image domain may be seen as a complex multivariate (one variable per coil) additive white Gaussian noise (AWGN) process, with zero mean and covariance matrix  $\Sigma$ . When the coil count is one, the noise distribution becomes Rician (Fernandez et al. (2009)) as already mentioned. However, for coil count greater than one, it follows a non-central *Chi* distribution. Since the final magnitude image is formed using sum of square method, (which is similar to averaging) this leads to blurring artifacts in the resultant image. Figure 2.2 shows the Probability Density Functions (PDF) for Rician and non-central *Chi* distribution.

### 2.2.1 Theory

The complex image formed at  $l^{th}$  coil is

$$u_{0l}(x) = u_l(x) + n_l(\sigma^2), \quad (2.1)$$

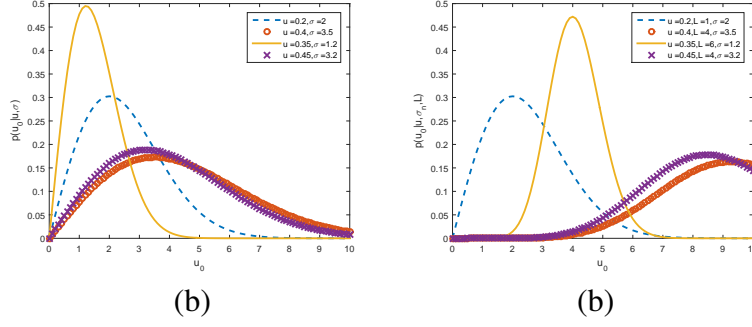


**Figure 2.2** Probability Density Function of (a) Rician distribution and (b) Non-central *Chi* distribution.

where  $u_l(x) \in \mathbb{R}^2$  is the original signal at  $l^{\text{th}}$  coil,  $u_{0l}(x) \in \mathbb{C}^2$  is the noisy complex signal at  $l^{\text{th}}$  coil and  $n_l(\sigma^2) = n_{lr}(x; \sigma^2) + j n_{li}(x; \sigma^2)$  is the complex noise in real ( $n_{lr}$ ) and imaginary planes (with equal variances). In case of multiple-coil MRIs ( $L$ -coils) the final image is formed by summing the magnitude images in each coil i.e.

$$u_0(x) = \sqrt{\sum_{l=1}^L |u_{0l}(x)|^2}. \quad (2.2)$$

As already mentioned above, the k-space images are corrupted with data-uncorrelated Gaussian noise  $\mathcal{N}(0, \sigma^2)$  in each of their domain, while taking the magnitude data, summing it from  $L$  coils and then taking its square-root makes the noise non-central *Chi* distributed (as root of sum of squares of Gaussian distributed random variables are *Chi* distributed). The PDF for the *Chi* distribution is

$$P(u_0|u, \sigma, L) = \frac{u^{L-1}}{\sigma_n^2} u_0^L e^{\left(-\frac{u_0^2+u^2}{2\sigma_n^2}\right)} I_{L-1}\left(\frac{u_0 u}{\sigma_n^2}\right) \mathcal{H}(u_0), \quad (2.3)$$

where  $\mathcal{H}(u_0)$  denotes the Heaviside function defined as

$$\mathcal{H}(x) = \begin{cases} 1 & \text{if } x \geq 0 \\ 0 & \text{elsewhere,} \end{cases}$$

and  $I_n(\cdot)$  is a modified  $n^{\text{th}}$ -order Bessel function of the first kind (see Fernandez and Vega (2013)). On the other hand in the background MRI, where the signal to noise ratio is considerably low i.e.  $\mu/\sigma^2 \approx 0$ , the noise is observed to follow a central *Chi* distribution with PDF

$$P(u_0|u, \sigma_n, L) = \frac{2^{L-1}}{\Gamma(L)} \frac{u_0^{2L-1}}{\sigma_n^{2L}} e^{-\frac{u_0^2}{2\sigma_n^2}} \mathcal{H}(u_0). \quad (2.4)$$

When  $L = 1$ , (2.3) and (2.4) become Rician distributed with PDF

$$P(u_0|u, \sigma_n) = \frac{u_0}{\sigma_n^2} e^{-\frac{u_0^2+u^2}{2\sigma_n^2}} I_0\left(\frac{u_0 u}{\sigma^2}\right) \mathcal{H}(u_0) \quad (2.5)$$

and Rayleigh distributed with PDF

$$P(u_0|u, \sigma) = \frac{u_0}{\sigma_n^2} e^{-\frac{u_0^2}{2\sigma^2}} \mathcal{H}(u_0), \quad (2.6)$$

in foreground and background images, respectively. Hereafter let us denote the noise variance with  $\sigma^2$  instead of  $\sigma_n^2$  without losing generality.

### 2.3 OVERVIEW OF MRI RESTORATION

Many papers have appeared in the recent literature for restoring single-coil magnitude MR images corrupted by Rician distributed noise, see Fernandez et al. (2009); Fernandez and Vega (2013). In Manjo et al. (2008), the model uses the non-local means(NLM) algorithm for restoring magnitude MR images, assuming the noise as a data independent Gaussian. A variational approach has been introduced in Liu et al. (2014) using the MAP estimation model for Rician distributed noise. A Variance Stabilization Transform (VST) makes the data un-correlated and subsequently unbiased, making it resemble a data-independent Gaussian, see Foi (2011). However, a MAP estimation method (Liu et al. (2015)) duly considering the noise distribution provides a better restoration compared to the VST based methods, as the noise distribution is being considered for removing the noise in the previous case and the data-dependent nature of the noise is being assumed throughout the restoration process.

While performing the image denoising, preserving of fine structures and edges are very important for the diagnosis of abnormalities in a medical image. Non-parametric neighborhood statistical information is being used in Awate and Whitaker (2005) for restoring MR images. 3D MR denoising is considered in Mukherjee and Qiu (2011), using local smoothing under non-parametric regression preserves edges and details to a larger extent. Wavelet based image restoration is commonly done for MR image denoising. In wavelet approaches, images are represented in a scale-space domain and the wavelet hard thresholding is applied to remove unwanted information in the image data (Wood and Johnson (1999)). An advanced averaging method which replaces each patch in the image by the mean of similar patches in a search window known as Non-Local

Means(NLM) has become one of the popular techniques in image denoising (Buades et al. (2005)). 3D non-local restoration method for MR images can be seen in Chang et al. (2015). Motivated by the well known Perona Malik anisotropic diffusion model (Perona and Malik (1990)), Krissian et al. (2005) proposed a similar model for Rician distributed noise. The coefficient of diffusion of this model is derived based on the Linear Minimum Mean Square Error (LMMSE) method, proposed by Aja-Fernandez et al. (2008) for denoising Rician distributed data. One of the common methods followed for MR image restoration is the bias removal technique(Sijbers and den Dekker (2004)). Since the magnitude image is formed by squaring and summing the magnitude data, the Rician distribution yields a constant bias term, i.e.  $2\sigma^2$ , which may be removed easily (see Sijbers et al. (1999)), i.e:

$$E(u_0) = E(u) + 2\sigma^2. \quad (2.7)$$

Statistical estimation methods have been proposed for MR image restoration. These models estimate the parameters using the Maximum Likelihood (ML) estimation and using these estimated parameters the bias removal is performed by the LMMSE model to retrieve the uncorrupted approximation of the image (Sijbers and den Dekker (2004)). Most recently an SNR adapted non-local LMMSE model was also proposed in Golshan et al. (2013) for MRI denoising and its recursive version can also be seen in the literature.

There are some models proposed for multiple-coil MR images corrupted by non-central Chi distributed noise, see Rajan et al. (2012) and Aja-Fernandez et al. (2013). In Rajan et al. (2012), the authors use an NLM approach to restore the multiple-coil MR image. The LMMSE approach on the magnitude image of each coil is used to get the desired output in Aja-Fernandez et al. (2013). Both are statistical models and they rely on estimating the underlying true signal based on the likelihood estimate of the non-local neighborhood selected based on the similarity among the pixels (in terms of the Euclidean similarity measure within the chosen neighborhood). The extended version of LMMSE with NLM denoising can be seen in Soumya et al. (2016). From the next section onwards, the formulation of a variational restoration model to handle multiple-coil MR images is discussed.

## 2.4 RESEARCH WORK

Many of the models discussed so far were designed for single coil MR data where the noise is found to follow a Rician PDF (Fernandez et al. (2009); Fernandez and Vega (2013)). Nevertheless, there are some initiatives in the direction of multiple-coil MR data restoration considering non-central *Chi* distribution (Rajan et al. (2012); Aja-Fernandez et al. (2013)), but their performance is limited as they tend to neglect the noise distribution and its data-correlated nature. This motivates us to propose a new approach to restore the multiple-coil as well as the single coil MR images (since the non-central *Chi* distribution becomes Rician distribution when the number of coils is set to one) duly caring the noise distribution and nature of the noise interference. A variational approach to denoise the multiple-coil MR image is being discussed in this chapter. The non-local total variation technique is used as a diffusion term. The fidelity term is derived using the MAP estimator of the non-central *Chi* distribution. For the numerical implementation, the split-Bregman iterative method, which is one of the faster converging schemes, is being used. Further, the condition for uniqueness of the solution is analyzed in Appendix A.

Non-local methods and their details have already been discussed in the first chapter. Here, non-local Total Bounded Variation (TBV) norm is being proposed in the place of non-local TV for a better restoration (Liu and Huang (2011)). The TBV norm is defined as  $\|u\|_{BV} = \|\nabla u\|_1 + \frac{\theta}{2}\|u\|_2^2$ , where the first term in the expression denotes the usual TV-norm and  $\theta \in [0, 1]$  is a scalar parameter which controls the magnitude of the two norms on the expression. The TBV norm imposes a constraint on the functional which ensures that the  $L^2$  norm of the image function is minimum along with the TV norm, which eventually performs better than normal TV while restoring the images.

### 2.4.1 Energy functional using MAP estimator

The methodology of deriving a MAP estimator by using the PDF of a noise distribution is explained in the first chapter. MAP estimator for the non-central *Chi* distribution is

derived in Appendix B.1. The final formulation is given by,

$$\min_u \{-\log P(u|u_0)\} = \min_u \left\{ (L-1) \log(u) + \frac{u^2}{2\sigma^2} - \log \left( I_{L-1} \left( \frac{u_0 u}{\sigma^2} \right) \right) + \gamma \phi(u) \right\}. \quad (2.8)$$

Now replacing  $\phi(\cdot)$  with non-local total variation-prior ( $J_{NLTV}$ ) we get the energy functional

$$\min_u \{-\log P(u|u_0)\} = \min_u \left\{ \int_{\Omega} (L-1) \log(u) + \frac{u^2}{2\sigma^2} - \log \left( I_{L-1} \left( \frac{u_0 u}{\sigma^2} \right) \right) dx dy + \frac{\gamma}{2} J_{NLTV}(u) \right\}. \quad (2.9)$$

Further considering the special case, when  $L = 1$  or assuming a Rician distribution of the noise in the data, we get

$$\min_u \{-\log P(u|u_0)\} = \min_u \left\{ \int_{\Omega} \frac{u^2}{2\sigma^2} - \log \left( I_0 \left( \frac{u_0 u}{\sigma^2} \right) \right) dx dy + \frac{\gamma}{2} J_{NLTV}(u) \right\}. \quad (2.10)$$

Now considering the  $J_{NLTV}(u)$  as the non-local bounded variation scheme and omitting the  $-\log$  function from the LHS of above equation (since it is a monotonic function), we get the functional in the form,

$$\min_u P(u|u_0) = \min_u \left\{ (L-1) \log(u) + \frac{u^2}{2\sigma^2} - \log \left( I_{L-1} \left( \frac{u_0 u}{\sigma^2} \right) \right) + \frac{\gamma}{2} \left( \|\nabla_{NL} u\|_1 + \frac{\theta}{2} \|u\|_2^2 \right) \right\}. \quad (2.11)$$

When we consider the image  $u$  which is corrupted by linear blur with the Gaussian blurring kernel  $K$ , the above equation becomes,

$$\min_u P(u|u_0) = \min_u \left\{ (L-1) \log(Ku) + \frac{(Ku)^2}{2\sigma^2} - \log \left( I_{L-1} \left( \frac{u_0 Ku}{\sigma^2} \right) \right) + \frac{\gamma}{2} \left( \|\nabla_{NL} u\|_1 + \frac{\theta}{2} \|u\|_2^2 \right) \right\}. \quad (2.12)$$

The above equation can be solved using Gradient descent time marching scheme, but it takes a long time to converge. Here, the split Bergman approach is being used for faster convergence.

## 2.4.2 Split-Bregman Iteration Method

The Bregman iteration is a technique used for solving of unconstrained minimization problems which is given below,

$$\min_u J(u) \quad \text{subject to} \quad H(u) = 0, \quad (2.13)$$



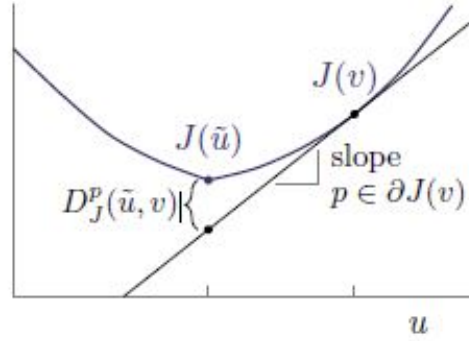


**Figure 2.3** The Bregman distance  $D_J^p(\tilde{u}, v)$  (image courtesy, Getreuer (2012a))

where  $J$  and  $H$  are convex functionals defined on Hilbert space. More details about analysis and applications can be seen in Bregman (1967) , Osher et al. (2005) , Wotao et al. (2008) and Jia et al. (2009) . The assumption is, there exists a minimizing of  $H$  for  $H(u) = 0$  and  $J(u) < \infty$ . The main idea used here is the *Bregman distance*. The diagram in Figure 2.3 gives the visual definition of the Bregman distance. The Bregman distance is defined as,

$$D_J^p(u, v) := J(u) - J(v) - \langle p, u - v \rangle, \quad p \in \partial J(v). \quad (2.14)$$

The Bregman distance compares the value of  $J(u)$  with tangent plane  $J(v) + \langle p, u - v \rangle$ . Figure (6) shows the distance in one-dimension. The curve denotes  $J(u)$  and the line is tangent to the plane  $J(v) + \langle p, u - v \rangle$ .  $\partial J$  is sub differential of  $J$ , (for more details see Lemarechal and Hiriart Urruty (1996)) which is defined as

$$\partial J(v) := \{p : J(u) \geq J(v) + \langle p, u - v \rangle \forall u\}. \quad (2.15)$$

Bregman distance is not symmetric. It satisfies following definitions and convexity of  $J$  (refer Osher et al. (2005)).

- $D_J^p(v, v) = 0$ .
- $D_J^p(u, v) \geq 0$ .
- $D_J^p(v, v) + D_J^{\tilde{p}}(v, \tilde{v}) = \langle p - \tilde{p}, v - u \rangle$ .

Considering a starting point  $u^0$ , and setting parameter  $\lambda > 0$ , minimizing functional of

Bregman iteration will be (see Bregman (1967)),

$$u^{k+1} = \arg \min_u D_J^{p^k}(u, u^k) + \lambda H(u), \quad p^k \in \partial J(u^k). \quad (2.16)$$

This gives,

$$u^{k+1} = \arg \min_u J(u) - \langle p^k, u - u^k \rangle + \lambda H(u). \quad (2.17)$$

Goldstein and Osher (2009), considered  $H(u) = \frac{\lambda}{2} \|Au - b\|_2^2$ . Where A is a linear operator and b is a vector. The simplified iteration scheme is as follows,

$$u^{k+1} = \arg \min_u J(u) + \frac{\lambda}{2} \|Au - b^k\|_2^2, \quad (2.18)$$

$$b^{k+1} = b^k + b - Au^k. \quad (2.19)$$

The considered minimization functional for diffusion was,  $J(u) = \int_{\Omega} \phi(u) dx dy$  (as detailed in the section 1.5.1), which can be any regularizer (such as TV minimization) and the minimization problem defined is,

$$\min_{u,d} \|d\|_1 + H(u) \quad \text{subject to} \quad d = \phi(u). \quad (2.20)$$

Using (2.18) and (2.19), the split-Bregman iteration scheme is given as follows,

$$(u^{k+1}, d^{k+1}) = \arg \min_{u,d} \|d\|_1 + H(u) + \frac{\lambda}{2} \|d - \phi(u) - b^k\|_2^2, \quad (2.21)$$

$$b^{k+1} = b^k + (\phi(u^{k+1}) - d^{k+1}). \quad (2.22)$$

$u$  and  $d$  in (2.21) can further be split as follows,

$$u^{k+1} = \arg \min_u H(u) + \frac{\lambda}{2} \|d - \phi(u) - b^k\|_2^2, \quad (2.23)$$

$$d^{k+1} = \arg \min_u \|d\|_1 + \frac{\lambda}{2} \|d - \phi(u) - b^k\|_2^2. \quad (2.24)$$

The generalized split-Bregman iterative algorithm is given in Algorithm 1.

---

**Algorithm 1** split-Bregman Algorithm

---

**Input:** Noisy image:  $u_0$ .

**Output:** Restored image:  $u$ .

```
1: Initialize  $\lambda, tol = 10^{-4}$ .
2: while do  $\|u^k - u^{k-1}\|_2 > tol$ 
3:
4:   for do  $n = 1$  to  $N$ 
5:      $u^{k+1} = \arg \min_u H(u) + \frac{\lambda}{2} \|d - \phi(u) - b^k\|_2^2$ 
6:      $d^{k+1} = \arg \min_d \|d\|_2 + \frac{\lambda}{2} \|d - \phi(u) - b^k\|_2^2$ 
7:   end for
8:    $b^{k+1} = b^k + (\phi(u^{k+1}) - d^{k+1})$ 
9: end while
```

---

### 2.4.3 Formulated model using split-Bregman iteration scheme

In the numerical implementation, the proposed model is derived for the two degradation scenarios,

- **case 1:** Image corrupted with noise (Blurring operator  $K$  is set to identity).
- **case 2:** Image corrupted with noise and linear shift-invariant blur.

**Case 1:** First let us consider the degraded image without blur. So the energy functional in (2.11) must be solved using split-Bregman iteration scheme. The total BV norm was used for image restoration with split Bregman iteration scheme for additive noise in Liu and Huang (2011). Since we deal with multiple-coil MR data, the denoising mechanism for the non-central *Chi* distributed noise is being detailed. The revised formulation under the total BV norm appears as

$$\min_{u \in BV(\Omega)} \left\{ \int_{\Omega} (L-1) \log(u) + \frac{u^2}{2\sigma^2} - \log I_{L-1} \left( \frac{u_0 u}{\sigma^2} \right) dx dy + \int_{\Omega} \frac{\gamma}{2} \left( \|\nabla_{NL} u\|_1 + \frac{\theta}{2} \|u\|_2^2 \right) dx dy \right\}. \quad (2.25)$$

Let us define

$$H(u) \triangleq \sum \left( (L-1) \log(u) + \frac{u^2}{2\sigma^2} - \log I_{L-1} \left( \frac{u_0 u}{\sigma^2} \right) \right),$$

for a discrete image let us drop the integration and assume a summation (without losing the generality, we are further dropping the summation sign to avoid abuse in notation

and attaching the regularization parameter  $\gamma$  with the data fidelity  $H$ ) and adding the constraint  $z = u$  as the penalty term, this gives

$$\min_z \left\{ \frac{\gamma}{2} H(u) + \|\nabla_{NL} z\|_1 + \frac{\theta}{2} \|z\|_2^2 + \frac{\beta}{2} \|z - u\|_2^2 \right\}, \quad (2.26)$$

where  $\beta \in [0, 1]$  is a scalar parameter.

$$(z^{k+1}, u^{k+1}) \triangleq \arg \min_{z, u} \left\{ \frac{\gamma}{2} H(u) + \|\nabla_{NL} z\|_1 + \frac{\theta}{2} \|z\|_2^2 + \frac{\beta}{2} \|z - u\|_2^2 \right\}. \quad (2.27)$$

Now splitting the above expression into two sub-problems we get  $u$ -subproblem and  $z$ -subproblem, respectively i.e.,

$$\min_u \left\{ \frac{\gamma}{2} H(u) + \frac{\beta}{2} \|z - u\|_2^2 \right\}, \quad (2.28)$$

and

$$\min_z \left\{ \|\nabla_{NL} z\|_1 + \frac{\theta}{2} \|z\|_2^2 + \frac{\beta}{2} \|z - u\|_2^2 \right\}. \quad (2.29)$$

Further adding the constraint  $d = \nabla_{NL} z$  in the above  $z$ -subproblem gives

$$\min_{z, d} \left\{ \|d\|_1 + \frac{\theta}{2} \|z\|_2^2 + \frac{\beta}{2} \|z - u\|_2^2 + \frac{\lambda}{2} \|d - \nabla_{NL} z - b^{k+1}\|_2^2 \right\}, \quad (2.30)$$

where  $b^{k+1} = b^k - (d^{k+1} - \nabla_{NL} z^{k+1})$  and  $\lambda \in [0, 1]$  is a scalar parameter. By further splitting the above problem into two subproblems we have ( $d$ -subproblem and  $z$ -subproblem, respectively)

$$\min_d \left\{ \|d\|_1 + \frac{\lambda}{2} \|d - \nabla_{NL} z - b^{k+1}\|_2^2 \right\}, \quad (2.31)$$

and

$$\min_z \left\{ \frac{\theta}{2} \|z\|_2^2 + \frac{\beta}{2} \|z - u\|_2^2 + \frac{\lambda}{2} \|d - \nabla_{NL} z - b^{k+1}\|_2^2 \right\}. \quad (2.32)$$

Now taking the first variation of the above functional with respect to  $z$  gives

$$z^{k+1} = \frac{1}{(\theta I + \beta I - \lambda \Delta_{NL})} (\beta u + \lambda \nabla_{NL} \cdot (d - b^k)), \quad (2.33)$$

and using Gauss-Seidel method (as  $\theta I + \beta I - \lambda \Delta_{NL}$  is diagonally dominant and  $\Delta_{NL}$  is the graph Laplacian which is positive semi-definite) we get solution for  $z$ . The  $d$ -subproblem can be solved using the shrinkage operator as:

$$d^{k+1} = \frac{\nabla_{NL} z + b^k}{|\nabla_{NL} z + b^k|} \max \left( |\nabla_{NL} z + b^k| - \frac{1}{\lambda}, 0 \right), \quad (2.34)$$

and  $u$  subproblem is solved using the Newtons method ( $u_{n+1} = u_n - f(x)/f'(x)$ ). With these formulations we can solve the optimization problem in (2.25) with split-Bregman scheme in an efficient manner.

**Case 2:** In the energy functional in (2.12) the image is considered with a linear blur. Split-Bregman deconvolution scheme for the Gaussian additive noise can be seen in

Zhang et al. (2010). Here, denoising and deblurring mechanisms are simultaneously done for the non-central *Chi* distributed noise. The revised formulation under the TBV norm appears as

$$\min_{u \in BV(\Omega)} \left\{ \int_{\Omega} (L-1) \log(Ku) + \frac{(Ku)^2}{2\sigma^2} - \log I_{L-1} \left( \frac{u_0 Ku}{\sigma^2} \right) dx dy + \int_{\Omega} \frac{\gamma}{2} \left( \|\nabla_{NL} u\|_1 + \frac{\theta}{2} \|u\|_2^2 \right) dx dy \right\}. \quad (2.35)$$

Let us define

$$H(u) \triangleq \sum \left( (L-1) \log(Ku) + \frac{(Ku)^2}{2\sigma^2} - \log I_{L-1} \left( \frac{u_0 Ku}{\sigma^2} \right) \right).$$

Image having both blur and noise can be restored by using the modified version of minimization problem defined in Zhang et al. (2010) as follows

$$v^{k+1} = u^k - \delta H'(u), \quad (2.36)$$

$$u^{k+1} = \arg \min_u \left\{ \|\nabla_{NL} u\|_1 + \frac{\theta}{2} \|u\|_2^2 + \frac{1}{2\delta} \|u - v^{k+1}\|_2^2 \right\}, \quad (2.37)$$

$$f^{k+1} = f^k + u_0 - Ku^{k+1}, \quad (2.38)$$

where  $\delta$  is a constant. By using the above constraint and putting a constraint  $d = \nabla_{NL} u$ , let us define the new unconstrained minimization problem

$$(u^{k+1}, d^{k+1}) = \arg \min_{u, d} \|d\|_1 + \frac{\lambda}{2} \|u - v\|_2^2 + \frac{\mu}{2} \|d - \nabla_{NL} u - b^{k+1}\|_2^2, \quad (2.39)$$

where  $\lambda = 1/\delta$  and

$$b^{k+1} = b^k + (\nabla_{NL} u - d^{k+1}). \quad (2.40)$$

Further the above problem can be split into two subproblems

*u-subproblem*

$$\min_u \frac{\lambda}{2} \|u - v\|_2^2 + \frac{\theta}{2} \|u\|_2^2 + \frac{\mu}{2} \|d - \nabla_{NL} u - b^{k+1}\|_2^2, \quad (2.41)$$

*d-subproblem*

$$\min_d \|d\|_1 + \frac{\mu}{2} \|d - \nabla_{NL} u - b^{k+1}\|_2^2. \quad (2.42)$$

Now the taking the first variation of  $u$  in the above u-subproblem, we have:

$$0 = \lambda(u - v) + \theta u + \mu \nabla_{NL}(d - b^k) - \mu \Delta_{NL} u, \quad (2.43)$$

$$u^{k+1} = \frac{\lambda v - \mu \nabla_{NL}(d - b^k)}{(\lambda + \theta)I - \mu \Delta_{NL}}, \quad (2.44)$$

since the matrix  $(I - \Delta_{NL})$  is diagonally dominant one can opt Gauss-Seidel method for solving it. Similarly, the *d-subproblem* can be solved using the *shrinkage* operator as

follows:

$$d^{k+1} = \text{shrink}(\nabla_{NL}u + b^k, 1/\mu),$$

where

$$\text{shrink}(x, y) = \frac{x}{|x|} * \max(|x| - y, 0). \quad (2.45)$$

Now considering a non-local TV in place of normal TV we can rewrite the above sub-problems by just replacing  $\nabla$  and  $\Delta$  with  $\nabla_{NL}$  and  $\Delta_{NL}$ , where  $\nabla_{NL}$  and  $\Delta_{NL}$  denotes the non-local gradient and Laplacian (as already defined earlier), respectively.

#### 2.4.4 Algorithm for the proposed scheme

**Case 1:** The split-Bregman iterative algorithm for multiple-coil MRI corrupted with *Chi* noise distribution (without blur) is detailed below

---

**Algorithm 2** Split-Bregman algorithm for non-central *Chi* distributed noise.

---

**Input:**  $u_0 \leftarrow$  Image corrupted by *Chi* noise distribution.

**Output:** Restored image  $u$ .

- 1: Initialize all parameters  $\lambda, \beta, \gamma$  etc.
  - 2: Initialize  $u^0, z^0, d^0$  and  $b^0$
  - 3: **while do not converged**
  - 4:     Solve the  $z$  – *subproblem* to get  $z^{k+1}$  using (2.32) (Gauss-Seidel Method)
  - 5:     Solve the  $d$  – *subproblem* to get  $d^{k+1}$  using (2.31) (Shrinkage Operator)
  - 6:     Solve the  $u$  – *subproblem* to get  $u^{k+1}$  using (2.28) (Newtons method)
  - 7:      $b^{k+1} = b^k + (\nabla_{NL} z - d^{k+1})$
  - 8: **end while**
- 

**Case 2:** The algorithm for the proposed MR image restoration scheme for the non-central *Chi* distributed noise with linear blur can be stated as follows

## 2.5 EXPERIMENTAL RESULTS

For the testing purpose, the images being used are downloaded from the Brain Web (URL: [http://brainweb.bic.mni.mcgill.ca/brainweb/selection\\_normal.html](http://brainweb.bic.mni.mcgill.ca/brainweb/selection_normal.html)). To check

---

**Algorithm 3** Split-Bregman algorithm for non-central *Chi* distributed noise and linear blur.

---

**Input:**  $u_0 \leftarrow$  Image corrupted by *Chi* noise distribution.

**Output:** Restored image  $u$ .

- 1: Initialize  $k = 1, u^1 = u_0, u^0 = 0, f^1 = u_0$ .
  - 2: **while do**  $\frac{|u^k - u^{k-1}|}{|u^k|} \geq \varepsilon$
  - 3:      $v^{k+1} = v^k - \delta H'(u)$
  - 4:      $u^{k+1} = \frac{\lambda v^{k+1} - \mu \nabla_{NL}(d - b^k)}{(\lambda + \theta)I - \mu \Delta_{NL}}$
  - 5:      $f^{k+1} = f^k + u_0 - Ku^{k+1}$
  - 6:      $d^{k+1} = \mathit{shrink}(|\nabla_{NL}u + b^k|, 1/\mu)$
  - 7:      $b^{k+1} = b^k + (\nabla_{NL}u - d^{k+1})$
  - 8:      $u^k = u^{k+1}, k \leftarrow k + 1$
  - 9: **end while**
- 

the restoration capability of our restoration model, three types of MR images have been considered, namely MRI T1-Weighted, T2-Weighted and PD-Weighted. The slice thickness is selected as 3mm. The intensity values are transformed to the range [0,1] (or normalized) for all test images. The non-central *Chi* distributed data is generated in the multiple-coil setup. We have tested all recent and relevant methods proposed for MRI noise removal(both for single and multiple-coil MR data) in the literature. Most of the methods in the literature works well for the single coil MR images which contain Rician distributed noise. When we tried to apply those methods for the multiple-coil MR images, the outcome was not as good as single coil case. The noise distribution in foreground data is observed as *Chi* and background is Rayleigh. Since background is zero SNR region we focus on the foreground region where the noise is non-central *Chi* distributed. The noise parameters for original MR images can be estimated from the zero SNR background region where the signal contribution is negligible. The magnitude of the image formed in  $k$  - space for each coil(total number of coils=6) can be seen in Figure 2.4. The final magnitude image is formed using SoS (sum of square) of the magnitudes (or CMS) at each coil. The magnitude images used for testing are shown in its original form in Figure 2.5. For the comparison purpose, mainly six models from the literature have been chosen, which are shown below,

- **Model 1:** LMMMSE by Aja-Fernandez et al. (2008)
- **Model 2:** variance stabilization for Rician by Foi (2011)

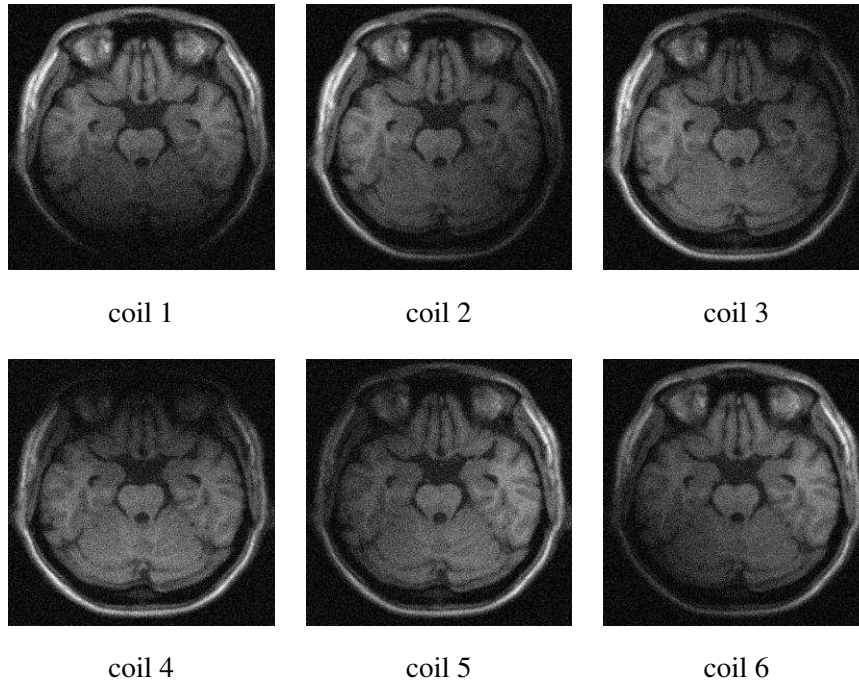


**Figure 2.4** Brain MRI from BrainWeb, 17<sup>th</sup> slice with 3mm thickness, simulated as multiple-coil with 6 coils. Above figure shows magnitude of image in k-space

- **Model 3:** non-local TV by Liu et al. (2015)
- **Model 4:** non-local means for Rician by Manjo et al. (2008)
- **Model 5:** LMMSE for multiple-coil MRI by Aja-Fernandez et al. (2013)
- **Model 6:** non-local filtering for multiple-coil MRI by Rajan et al. (2012)

Parameters used in each algorithm to get the optimum results in terms of visual perception are given in Table 2.1. Results of comparison for single coil MR images without blur are given in Figure 2.8 and with the linear blur are given in Figure 2.9. For multiple-coil MR images without blur, results of various methods are given in Figure 2.10 and the results for both the noise and blurry images are given in Figure 2.11 . The results shown in terms of figures highlight the restoration capability of the proposed model, as evident from these figures, the model has restored the data with due respect to the structures, edges, and details present in it. Moreover, the blurring effects are reduced considerably in the proposed strategy.



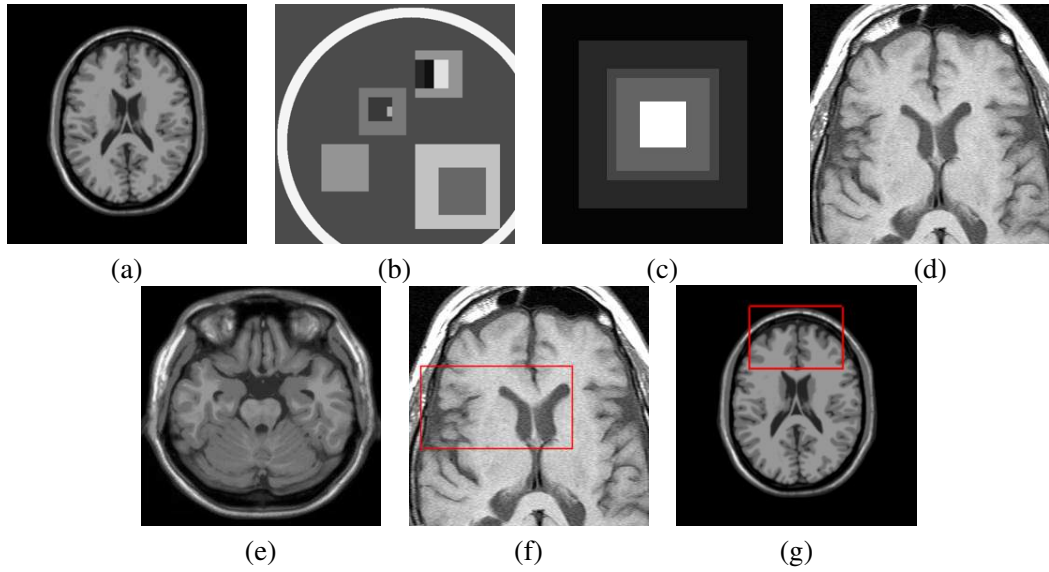


**Figure 2.5** Images (a), (b), (c), (d) and (e) in their original form (magnitude image generated from 8 coils using Sum of Squares (SoS)) used for testing and (f), (g) highlighted portions of the image (in red rectangular representation) enlarged after applying various restoration methods

To show that the proposed model works efficiently compared to other models, a quantification is necessary, so a statistical analysis is performed. Let us consider two common image statistical metrics: SNR and SSIM (see Section 1.8 for more details). Table 2.2 (for the noisy image) and Table 2.3 (for the image with noise and blur) shows the SNR values calculated for various Rician restoration models considered and the proposed one. In the similar way, Table 2.4 and 2.5 shows the SSIM values calculated for different models with the proposed scheme.

Table 2.6 (for noisy image) , Table 2.7 (image with noise and blur) and Table 2.8 (image with non-central *Chi* distributed noise), Table 2.9 (image with non-central *Chi* distributed noise and blur) shows the SNR and SSIM comparison of the proposed model with Model 5 and Model 6 respectively. The performance of the proposed model is superior to the other comparative ones in terms of SSIM values, therefore the model has retained structures and details present in the data while performing the restoration. As we can observe in Table 2.2, which shows the results of SNR evaluated for the degradation model in case-1, the SNR for other methods are higher than the proposed model, this is because the proposed model is designed to handle non-central *Chi* distribution, whereas the noise distribution in single-coil MR images is Rician. Therefore, the mod-

els designed for Rician distribution performs better noise elimination than the proposed one. But the proposed scheme shows the better structural preserving capability, which is evident in Table 2.4. However, for case-2 degradation model, the proposed model gives better results for both SNR and SSIM irrespective of coil count.

An enlarged portion of the MR image from Figure 2.5 (f) (highlighted using a RED rectangle) is shown in Figure 2.6 and 2.12 for Rician and *Chi* noise distributions (i.e, single and multiple-coil MR data) respectively. The expanded portion of MR image from Figure 2.5 (g) is shown in Figure 2.7 and 2.13 for Rician and *Chi* noise distributions with linear blur respectively. As all the resultant images are enlarged, the structural and edge preservation capability of the proposed model is evident. The split-Bregman solver employed here makes the iterative model to converge in 3 to 5 iterations, whereas the other models take at least 15 to 20 iterations. The gradient descent approach takes minimum 50 iterations to give the desired result. The fast converging capability of the proposed model makes it suitable to employ for real-time imaging applications. The uniqueness of the solution is analyzed in Appendix A.3, which completes the theoretical analysis.

## 2.6 Summary

A restoration model has been devised in this chapter to handle the data-dependent *Chi* distributed noise, which is one of the pertinent needs in the field of medical MR imaging. For the single coil case, average SNR of Model 1 and Model 4 are 23.17 and 24.3 respectively, which are higher than the other models. Model 1 uses a MAP estimation of the Rice distribution for deriving the data fidelity term and a TV functional is used as a regularizer. The higher SNR value (on an average) of the model is justified by the magnitude of diffusion, which eventually results in smooth structures while penalizing the details. Therefore, the average SSIM value (i.e, 0.54) is slightly on the lower side. Model 4 uses NLM method which is efficient in both smoothing and edge preserving, so results in a better value of SNR (average of 24.3) as well as SSIM (average of 0.61). Since, the noise is considered as data independent, the average SSIM is less than the proposed one. Model 2 stabilizes the variance of the data, making it independent of the noise. Subsequently, a restoration model for additive white Gaussian noise is employed

**Table 2.1** The parameter values used for various methods.

Parameter	Model 1	Model 2	Model 3	Model 4	Model 5	Model 6	Proposed
$\lambda$	-	0.1	-	-	-	-	70
$\delta$	-	-	-	-	-	-	30
$\Delta r$	-	0.25	0.25	-	-	-	-
$\gamma$	-	-	0.02	-	-	-	0.02
$\beta$	-	-	0.5	-	-	-	17.5
Search patch size	-	-	-	5	-	3	-
Search window size	7	-	-	7	7	5	-

to retrieve the final data. This causes high smoothing effect and gives better average SNR value of 22.36, but the fine edges and structures are penalized severely and thus results in average SSIM of 0.55. Model 3 and the proposed model gives similar average SNR (21.51 and 21.59 respectively) as well as SSIM (0.8). This is due to the fact that, *Chi* PDF becomes Rician PDF when the coil count is one, causing the restoration models to perform similar. Model 5 uses LMMSE method which uses the mean of local patches to minimize the mean square error which eventually reduces the noise, resulting in the average SNR of 19.51 and better average SSIM of 0.71. Nevertheless, the noise distribution is neglected in this model, thus results in inferior performance compared to the proposed model. Meanwhile, Model 6 extends NLM method to multiple coil case, resulting in better smoothing (average SNR of 20.17) but below average performance in preserving fine details (average SSIM of 0.63). The proposed one uses the noise PDF to derive the restoration model and uses the efficient NLTBV diffusion scheme that helps in achieving a better approximation to the desired data. The average SNR of 20.12 and average SSIM of 0.77 produced by the proposed model shows that it outperforms the other models.

The next chapter deals with the restoration of data-correlated Rayleigh noise, which commonly occurs in ultrasound and SAR imaging applications.

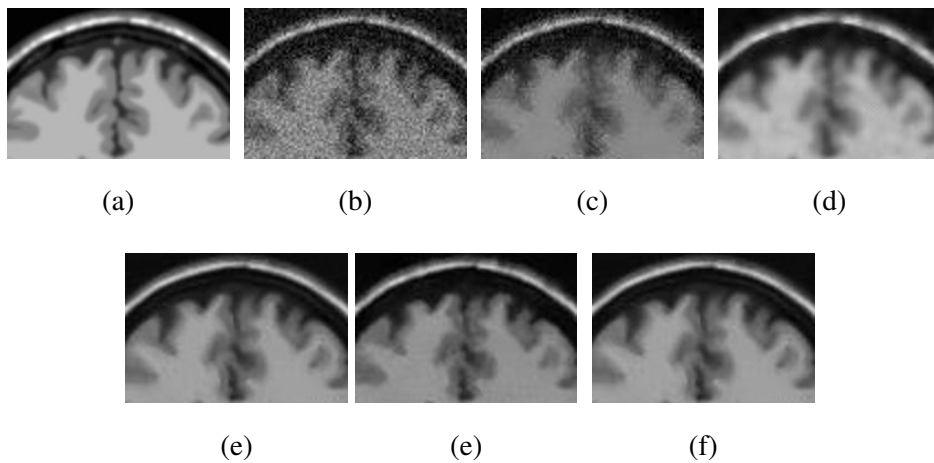


**Figure 2.6** (a) Original PMRI Image (b) Image with Rician noise  $\sigma=25$ ,  $SNR=13.47$  (c)Model 1,  $SNR=17.89$  (d)Model 2,  $SNR=18.62$  (e) Model 3,  $SNR=16.45$  (f) Model 4,  $SNR=20.57$  (g) The proposed model,  $SNR=15.09$

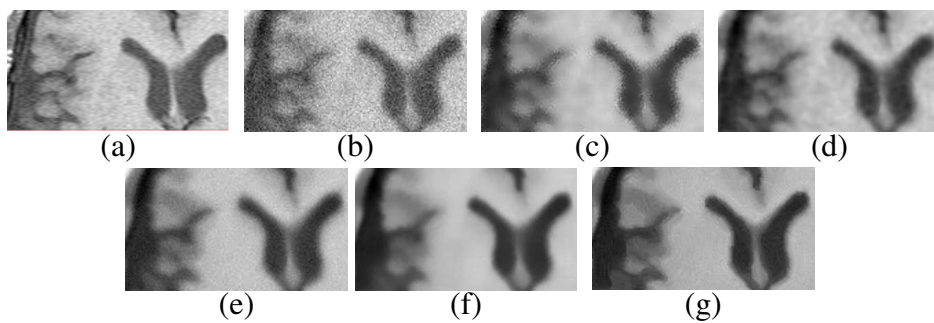


**Figure 2.7** (a) Original MRI test Image (b) Image with Rician noise of variance=18, blur of  $\sigma=2.0$ ,  $SNR=15.10$  (c)Model 1,  $SNR=17.13$  (d)Model 2,  $SNR=16.97$  (e) Model 3,  $SNR=15.23$  (f) Model 4,  $SNR=15.92$  (g) The proposed model,  $SNR=17.23$

**Table 2.2** SNR tabulated for the single-coil data (Rician distributed noise) of different models considered in this chapter for noise variance (15,25), respectively

Image name	Noisy	Model 1	Model 2	Model 3	Model 4	Proposed
Synthetic	(12.07, 7.38)	(21.17, 16.62)	(15.16, 11.73)	(14.78, 11.76)	(15.64, 10.32)	(15.05, 11.96)
Phantom MRI	(18.43, 14.12)	(22.78, 20.67)	(21.35, 20.71)	(21.23, 20.02)	(26.07, 21.87)	(21.44, 20.40)
MRI T1w	(17.82, 13.47)	(22.39, 19.96)	(24.04, 20.6)	(22.86, 16.71)	(25.02, 20.72)	(22.66, 18.87)
MRI T2w	(17.58, 13.19)	(20.99, 17.89)	(21.62, 18.62)	(20.98, 16.45)	(23.96, 20.57)	(22.13, 15.09)
MRI PDw	(22.46, 17.91)	(28.55, 25.94)	(29.64, 26.36)	(27.71, 20.16)	(30.84, 27.47)	(26.67, 20.33)

**Table 2.3** SNR tabulated for the single-coil data (Rician distributed noise and linear blur) of different models considered in this chapter for noise variance (18,25) with Gaussian blur of sigma (2.0,0.8) respectively

Image name	Noisy	Model 1	Model 2	Model 3	Model 4	Proposed
Phantom MRI	(15.61, 13.91)	(18.77, 20.13)	(19.15, 20.67)	(16.11, 16.34)	(16.78, 20.17)	(19.46, 20.97)
Synthetic	(13.99, 13.53)	(14.56, 14.34)	(16.43, 19.14)	(16.41, 18.07)	(19.24, 21.69)	(18.48, 22.12)
MRI T1w	(15.10, 14.34)	(17.13, 19.28)	(16.97, 18.02)	(15.23, 15.89)	(15.92, 18.68)	(17.23, 18.59)

**Table 2.4** SSIM tabulated for the single-coil data (Rician distributed noise) of different models considered in this chapter for noise variance (15,25), respectively

Image name	Noisy	Model 1	Model 2	Model 3	Model 4	Proposed
Synthetic	(0.09, 0.05)	(0.15, 0.11)	(0.17, 0.16)	(0.69, 0.52)	(0.18, 0.11)	(0.70, 0.45)
Phantom MRI	(0.48, 0.32)	(0.62, 0.54)	(0.51, 0.46)	(0.59, 0.48)	(0.75, 0.6)	(0.78, 0.63)
MRI T1w	(0.47, 0.3)	(0.66, 0.54)	(0.71, 0.6)	(0.83, 0.67)	(0.74, 0.58)	(0.87, 0.70)
MRI T2w	(0.51, 0.39)	(0.66, 0.58)	(0.71, 0.61)	(0.87, 0.74)	(0.73, 0.62)	(0.90, 0.75)
MRI PDw	(0.36, 0.12)	(0.60, 0.46)	(0.67, 0.56)	(0.83, 0.64)	(0.66, 0.49)	(0.87, 0.65)

**Table 2.5** SSIM tabulated for the single-coil data (Rician distributed noise and linear blur) of different models considered in this chapter for noise variance (18,25) with Gaussian blur of sigma (2.0,0.8) respectively

Image name	Noisy	Model 1	Model 2	Model 3	Model 4	Proposed
Phantom MRI	(0.29, 0.31)	(0.44, 0.51)	(0.49, 0.58)	(0.61, 0.6)	(0.34, 0.55)	(0.55, 0.61)
Synthetic	(0.15, 0.18)	(0.26, 0.31)	(0.21, 0.25)	(0.7, 0.74)	(0.24, 0.3)	(0.72, 0.76)
MRI T1w	(0.23, 0.28)	(0.33, 0.41)	(0.35, 0.45)	(0.51, 0.57)	(0.33, 0.45)	(0.59, 0.58)

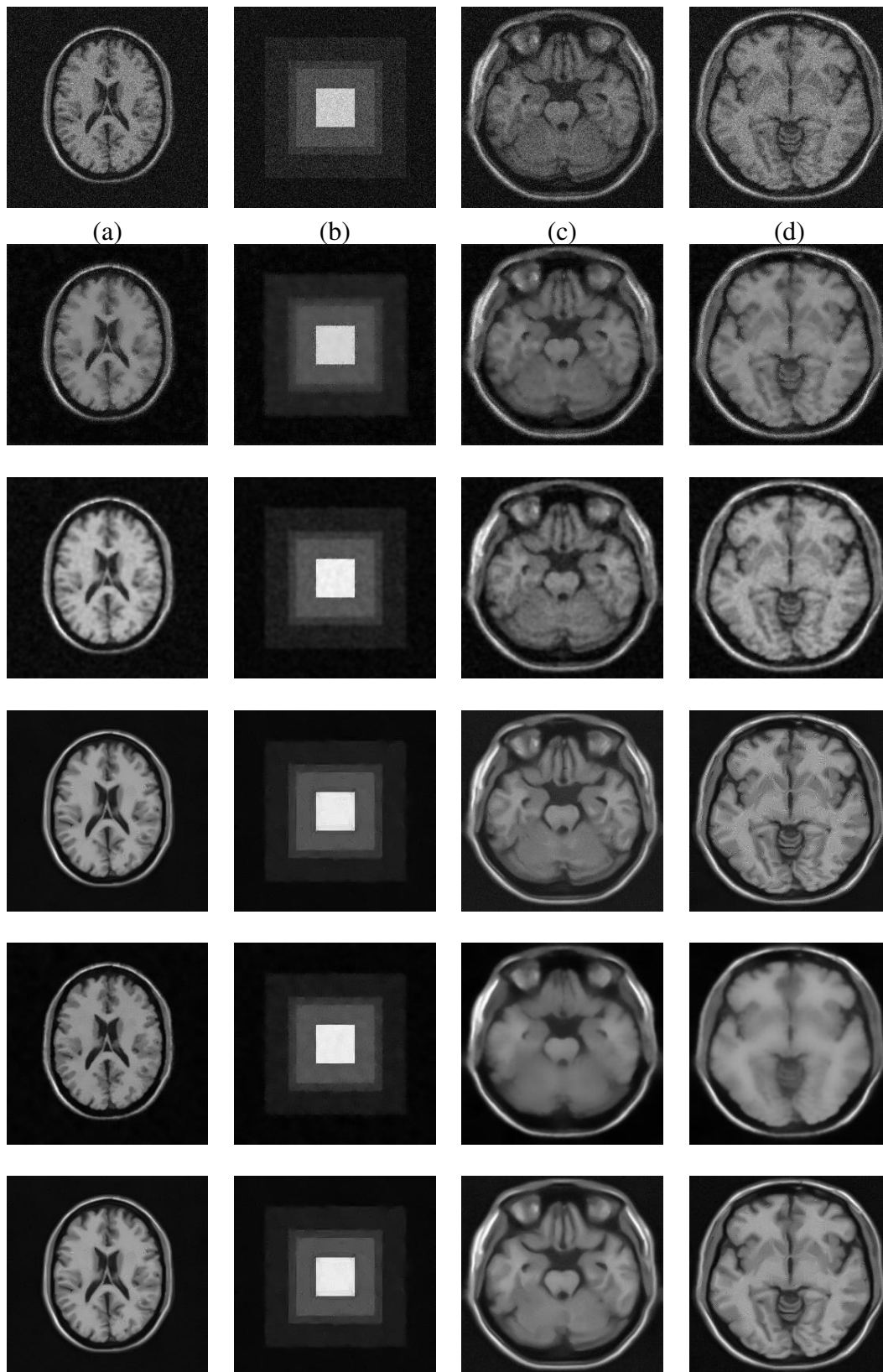


**Figure 2.8** Row 1:(a), (b) and (c) are noisy images corrupted by Rician noise and (d) Real MRI image; Rows 2,3,4,5 and 6: show image restored using Model-1, Model-2, Model-3, Model-4 and The proposed model

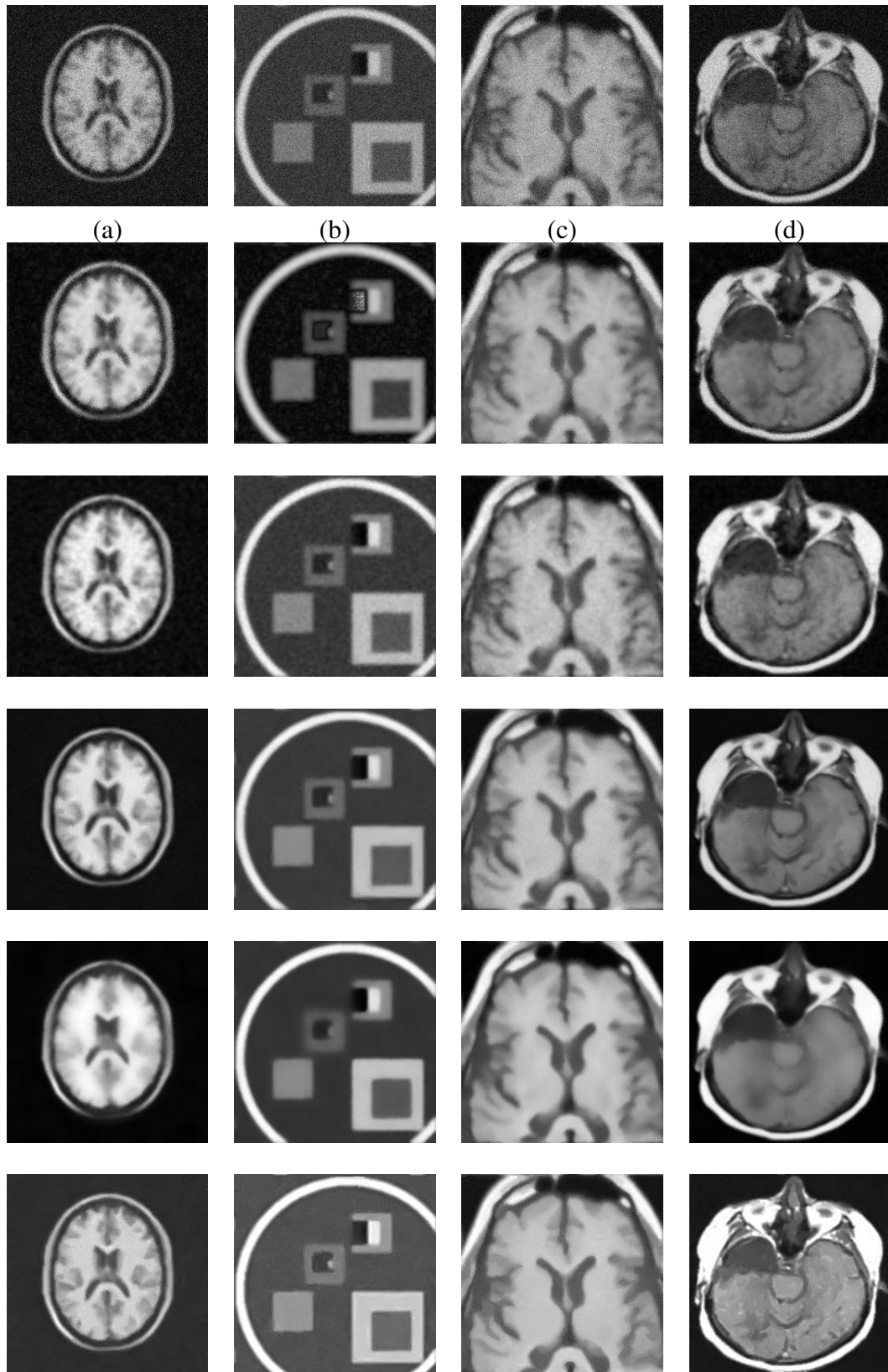


**Figure 2.9** Row 1:(a), (b) and (c) are noisy images corrupted by Rician noise and linear blur, and (d) Real MRI image; Rows 2,3,4,5 and 6: show image restored using Model-1, Model-2, Model-3, Model-4 and The proposed one

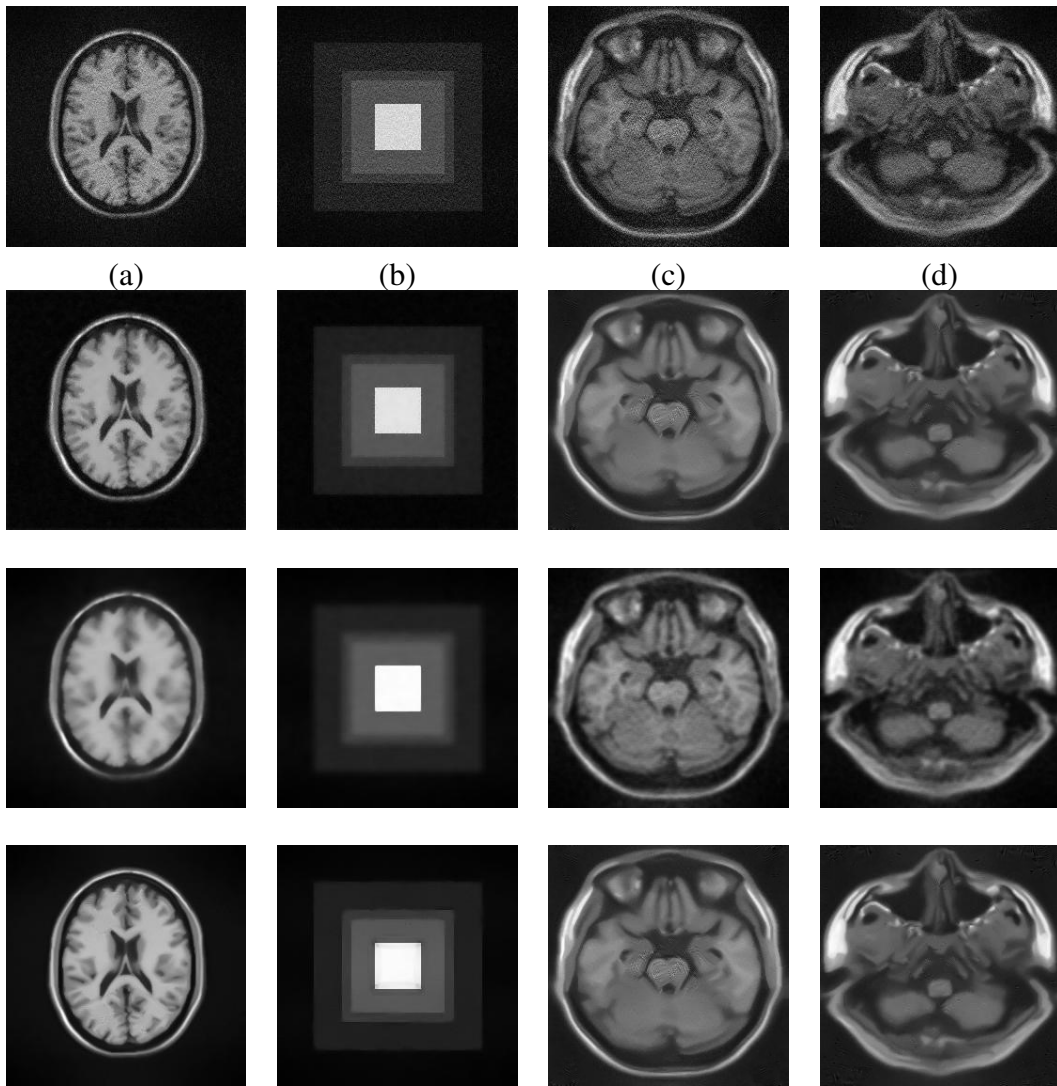


**Figure 2.10** Row 1:(a), (b) and (c) are noisy images corrupted by Non-central Chi distribution and (d) Real Multiple-coil Magnitude image of 6-coils. Rows 2,3 and 4: show image restored using Model-5, Model-6 and The proposed model



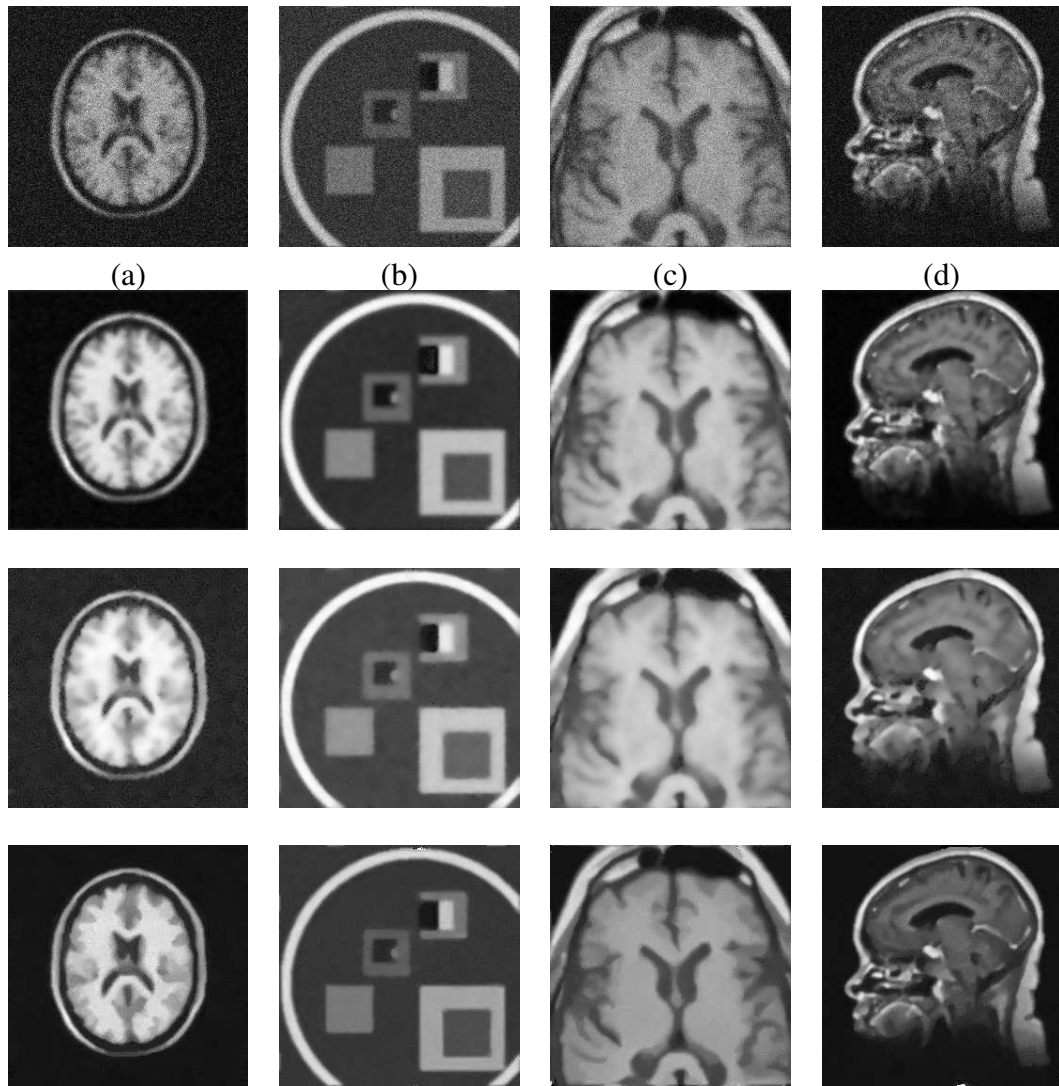


**Figure 2.11** Row 1:(a), (b) and (c) are noisy images corrupted by Non central Chi distribution with 8 coils and linear blur, (d) Real Multiple-coil Magnitude image of 8-coils. Rows 2,3 and 4: show image restored using Model-5, Model-6 and The proposed model

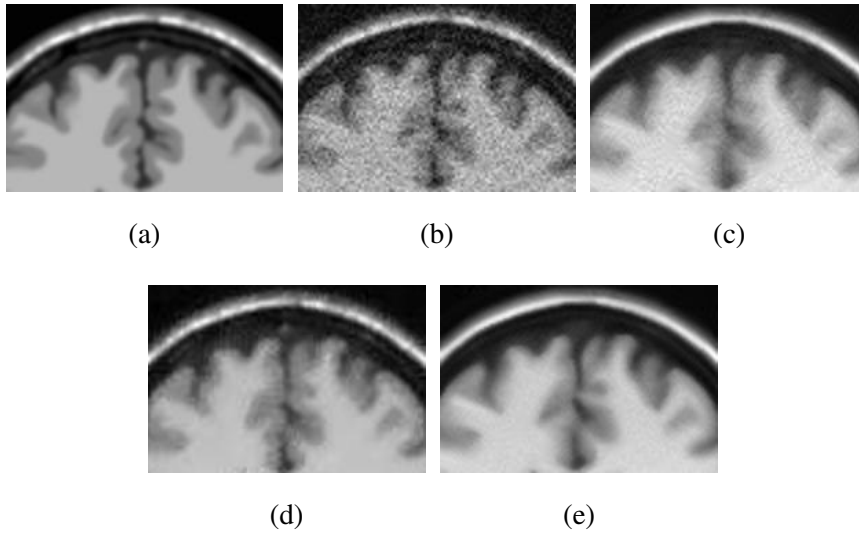


**Figure 2.12** (a) Original PMRI Image (b)Image with multiple-coil *Chi* noise sigma=75, coils=6, SNR=18.74 (c) Model 5, SNR=19.3 (d) Model 6, SNR=19.29 (e) The Proposed model, SNR=20.3

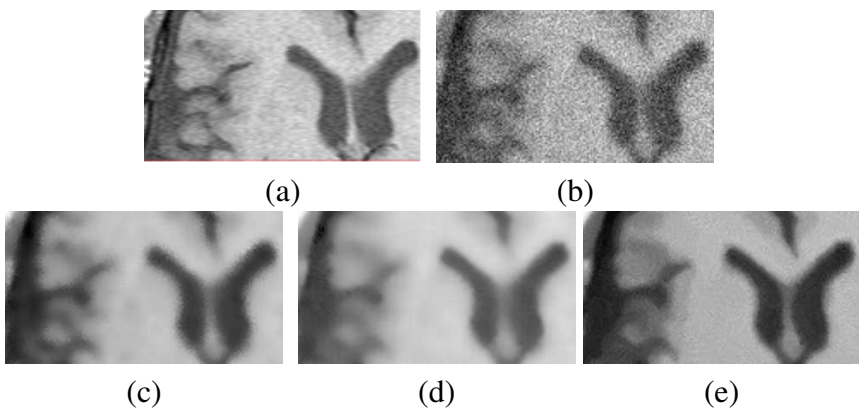


**Figure 2.13** (a) Original PMRI Image (b)Image with multiple-coil-*Chi* noise sigma=45, coils=8, blur of sigma=1.2 and SNR=16.8 (c) Model 5, SNR=26.26 (d) model 6, SNR=25.01 and (e) Proposed model, SNR=25.45

**Table 2.6** SNR tabulated for the multiple-coil data (Chi-distributed noise) of different models considered in this chapter for noise variance (40,75), respectively

Image name	Sigma	No. of coils	Noisy	Model 5	Model 6	Proposed
Synthetic	40	6	13.47	18.99	16.87	15.44
	75	2	13.54	17.59	15.37	17.15
Phantom MRI	40	6	20.72	18.27	23.14	21.5
	75	2	18.74	19.15	20.21	20.3
MRI T1w	40	6	21.71	21.27	20.51	23.44
	75	2	15.34	19.88	19.06	20.84

**Table 2.7** SNR tabulated for the multiple-coil data (Chi-distributed noise and linear blur) of different models considered in this chapter for noise variance (45,65) and Gaussian blur with sigma (1.2,1.8) and 8 coils respectively

Image name	Sigma	Blur	Noisy	Model 5	Model 6	Proposed
Phantom MRI	45	1.2	14.89	28.17	23.35	24.61
	65	1.8	15.66	24.98	24.36	25.91
Synthetic	45	1.2	14.74	23.32	26.53	25.97
	65	1.8	15.59	18.06	25.59	24.45
MRI T1w	45	1.2	16.8	26.26	25.01	25.45
	65	1.8	17.73	26.87	24.45	26.59

**Table 2.8** SSIM tabulated for the multiple-coil data (Chi-distributed noise) of different models considered in this chapter for noise variance (40,75), respectively

Image name	Sigma	No. of coils	Noisy	Model 5	Model 6	Proposed
Synthetic	40	6	0.14	0.72	0.46	0.67
	75	2	0.1	0.79	0.36	0.78
Phantom MRI	40	6	0.65	0.65	0.66	0.82
	75	2	0.49	0.57	0.63	0.79
MRI T1w	40	6	0.64	0.78	0.77	0.83
	75	2	0.38	0.73	0.71	0.72

**Table 2.9** SSIM tabulated for the multiple-coil data (Chi-distributed noise and linear blur) of different models considered in this chapter for noise variance (45,65) and Gaussian blur with sigma (1.2,1.8) and 8 coils respectively

Image name	Sigma	Blur	Noisy	Model 5	Model 6	Proposed
Phantom MRI	45	1.2	0.24	0.7	0.64	0.72
	65	1.8	0.31	0.66	0.69	0.7
Synthetic	45	1.2	0.2	0.42	0.41	0.52
	65	1.8	0.21	0.34	0.38	0.48
MRI T1w	45	1.2	0.28	0.72	0.7	0.75
	65	1.8	0.34	0.68	0.65	0.74



## Chapter 3

# NON LOCAL TOTAL VARIATION REGULARIZATION MODELS FOR RESTORING RAYLEIGH NOISE

### 3.1 INTRODUCTION

Restoration of images under data-correlated noise distribution is a challenging task. To model an efficient method to restore such kind of distortion, one has to consider the noise distribution that corrupts the image data (see Rudin et al. (1992); Weickert (1997); Milanfar (2013) for more details). Most of the practical imaging modalities produce data-correlated noise. This had been a matter for concern over the last couple of decades. For these kinds of noise models, Variance Stabilization Transformation (VST) and MAP restoration models are more popular in the literature. VST stabilizes the variance; subsequently, the data gets transformed to a domain where the samples are uncorrelated. The MAP estimation techniques maximize the posterior probability of the data and in the sequel, it gives an energy functional whose minimum is the desired solution. VST methods have been proposed for Poisson and Poisson-Gaussian noise distributions in Azzari and Foi (2016); Makitalo and Foi (2013a), respectively. A similar analysis is done for data-dependent Rician distribution as well, see Foi (2011). For Rayleigh distributed noise, VST combined with non-local TV is proposed by Makitalo et al. (2010). MAP estimation methods are also proposed for Gaussian, Gamma, Poisson and Rician distributions by Rudin et al. (2003); Aubert and Aujol (2008); Le et al. (2007); Liu et al. (2015), respectively. In these works, an energy functional is

being derived based on maximizing the posterior probability of the density function. The total variation prior is being assumed in the aforementioned works. In this chapter, an image restoration model has been introduced, which can remove the data-correlated multiplicative noise whose PDF is Rayleigh distributed. Such kinds of high amplitude multiplicative noise fluctuations are also known as speckles. In the next section, we highlight some speckle reduction techniques cited in the recent literature.

### **3.1.1 Speckle reduction in brief**

There are some models proposed for restoring images under data-correlated speckle noise (following a Gamma distribution) Aubert and Aujol (2008); Yu and Acton (2002); Krissian et al. (2007); Fernandez and Lopez (2006); Suna et al. (2004); Bini and Bhat (2014). Similar studies are reported for Rayleigh noise removal as well in the literature. An NLTV model to restore Rayleigh data has been proposed in Shuai et al. (2015). Thresholding in the transformed domain (such as wavelet, Fourier etc) reduces the noise remarkably, which has been done in Sarode and Deshmukh (2011). Yahya et al. (2014) derived a linear optimal estimator, which helps to reduce speckle noise while preserving fine structures. Maximum likelihood bilateral filter to restore ultrasound images corrupted by Rayleigh noise was proposed by Li et al. (2017). However, not much extensive analysis relating to the Rayleigh distribution has been done in the literature. Besides, none of the models proposed so far for the Rayleigh noise distribution (which use the fast solver such as split-Bregman scheme) consider the linear blurring artefacts along with the noise. Further, as observed in some previous works, the ultrasound (US) and Synthetic Aperture Radar (SAR) data are generally corrupted by speckles (granule-like structures) and at a high scatter density these speckles are found to follow a Rayleigh distribution Jin and Yang (2011b). This motivates us, to propose an efficient model to overcome the Rayleigh distributed speckles commonly found in US and SAR imagery.

### **3.1.2 Ultrasound image**

Ultrasound is a sound wave with frequency higher than those audible to humans (> 20,000 Hz). In medical diagnosis, ultrasound imaging is one of the common and harm-

less techniques. In this method, images of human internal body structures such as tendons, muscles, joints, blood vessels, and internal organs are formed. Firstly, pulses of ultrasound (using a transducer) are passed into internal body tissues. From these different kinds of tissues, various echoes are recorded and displayed as an image to the viewer. The transducer contains an array of individual ultrasound sources and the frequency of sound waves is usually between 1 to 15 MHz (Smith and Webb (2010)). During the acquisition process, these probes produce parallel beam of ultrasound waves which are passed through the section of a human body. When the ultrasound is passed through the boundary of a tissue, it reflects a small amount of sound energy, which is further recorded by the transducer. Depending on the time gap between releasing and capturing of the signal, the distance to each tissue boundary is calculated, hence the methodology is similar to the radar techniques. Due to the constructive and destructive interference of sound waves, the pattern of dark and white dots are seen in the resultant image, which is speckle in nature (Abbott and Thurstone (1979)). Figure 3.1 shows the mechanism of ultrasound imaging. The sound travels through a tissue with the speed of 1540 meters per second approximately, hence the acquisition of an entire image takes place within the fractions of a second.

## **Applications**

Among all the medical imaging techniques ultrasound is widely used and least expensive. It can be done with lower or no safety concerns. The applications include morphology, blood flow measurements, to form structural informations etc. Due to the technological improvements in both software and hardware, the ultrasound image quality has been improved drastically in past decade. However, the images formed by ultrasound system are still speckled.

### **3.1.3 Synthetic Aperture Radar image**

Normal digital cameras use light sensors to form the image of an object placed at a small distance from the camera. But in case of satellite imaging the object is far away from the camera, hence the sensors should be strong enough to capture remote objects. Such imaging methodology is called as the remote sensing (Lillesand et al. (2014)),

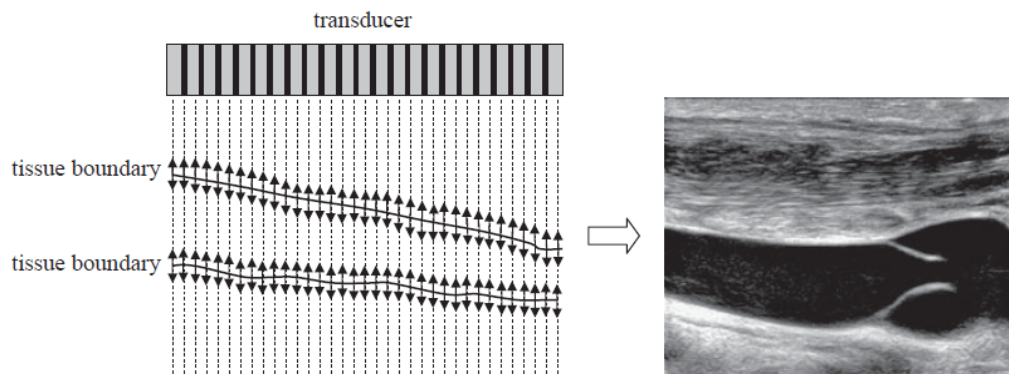


**Figure 3.1** Ultrasound imaging mechanism (image courtesy: Smith and Webb (2010))

which uses Light Detection and Ranging (LiDAR) to form an image of the earth surface. There are mainly two types of LiDAR systems: active and passive. Radio signals are transmitted to the target object/area to form an image using the reflected response waves in case of an active LiDAR, whereas a passive LiDAR records the echoes of the sunlight, hence it works only during the daytime. Synthetic Aperture Radar (SAR) imaging uses a RADAR (**R**Adio **D**etection **A**nd **R**anging) to form an image of the earth surface. Between the two types of LiDAR systems, SAR falls in the category of active LiDAR system. In the SAR system, successive pulses of radio waves are transmitted to the target land and echoes are recorded, which will vary depending on the particles which the rays are hit (Chan and Koo (2008)). These recorded waves are converted into the desired image. Hence, in SAR imagery the image can be formed at any time and any weather conditions. A basic radar system contains a switch, antenna, transmitter, receiver and recorder as shown in Figure 3.2. Switch is connected to both the antenna and the receiver, helps in sending a pulse through the antenna as well as receiving an echo by the receiver. An electromagnetic wave is sent to the target land and the reflected waves are collected back by the antenna which is transmitted to the receiver. As the size of the antenna is bigger, more data can be collected in one capture. Further, these response waves are converted into a digital form and recorded by the recorder. These stored data are further processed to form a digital image. The electromagnetic signals transmitted from the antenna have the least effect of surroundings, but the received signals vary due to scattering of waves on the hitting object, varying depth of earth's



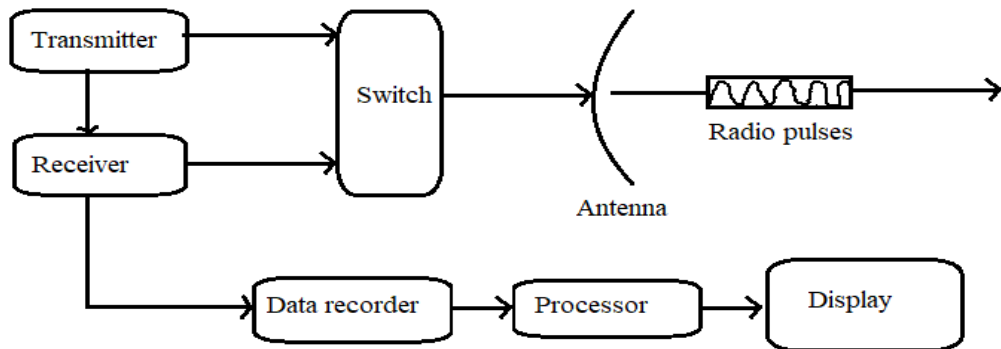


**Figure 3.2** Block diagram of SAR imaging system (image courtesy: Chan and Koo (2008)).

surface and movement of the antenna. Random fluctuations in the returned signal due to these reasons cause noise in the formed image which is speckled in nature (Porcello et al. (1976)).

### **Applications of SAR**

SAR is the widely used imaging system in satellite imagery. Tracking of movement of ships on the ocean can be done using SAR imaging. Also, illegal or accidental oil spills in an ocean by the ships or industries can be detected by the radars. At the high latitudes, SAR imaging helps to determine the ice formation which helps in navigation. weather forecasting such as cloud movements can be well determined by SAR imaging. On the land, SAR imaging helps in finding suitable land for forestry and agriculture purposes.

Due to the wide variety of applications, the image enhancement is crucial for proper analysis in SAR imaging. From the next section onwards the formulated speckle reduction method is explained.

### **3.2 RESEARCH WORK**

In this section, three models are being introduced for restoring images corrupted by data-correlated Rayleigh noise and linear blurring artefacts. The first one is based on the variance stabilization transform, which transforms the data to a domain where the noise variance is constant. The second and third models are based on the variational framework whose energy functional is designed based on the MAP estimator of the

noise PDF. The first among them uses a non-local total variational regularization prior whereas the second one uses a non-local total bounded variational regularization prior. Fast numerical solver using the well-known split-Bregman iterative scheme is proposed for the implementation. The condition for the existence of a unique minimizer is analyzed in Appendix A.4. A detailed experimental analysis is carried out using various statistical metrics.

### 3.2.1 Variance stabilizing transform for Rayleigh distribution

Stabilization of the variance makes the noise uncorrelated with the data. Subsequently, the distribution approaches an additive Gaussian. The main idea behind stabilizing the variance is, defining a transform function that makes the variance a constant in the transformed domain. This function is assumed to be monotonic. Here a variance stabilization transform for Rayleigh noise has been derived as in Mäkitalo et al. (2010).

#### Model I

Let us assume  $Y$  be a random sample selected from a Rayleigh distribution having the probability density function (PDF)

$$p(x; \sigma) = \frac{x}{\sigma^2} e^{-\frac{x^2}{2\sigma^2}}, \quad (3.1)$$

where  $\sigma > 0$  is the scale parameter and  $x \in [0, \infty)$ . The mean of the PDF is

$$\mu = \sigma \sqrt{\frac{\pi}{2}} \quad (3.2)$$

and variance

$$\text{var}(Y) = g(\mu) = \left(\frac{4 - \pi}{2}\right) \sigma^2. \quad (3.3)$$

Let  $h(Y)$  be a monotonic function which transforms the data to a domain in which the variance is constant. By using Taylor expansion, one can write

$$h(Y) = h(\mu) + h'(\mu)(Y - \mu), \quad (3.4)$$

$$(h(Y) - h(\mu))^2 = (h'(\mu))^2 (Y - \mu)^2, \quad (3.5)$$

$$\text{var}(h(Y)) = (h'(\mu))^2 \text{var}(Y). \quad (3.6)$$

Since the variance is one in the transformed domain i.e.  $\text{var}(h(Y)) = 1$ , from the above expression we have,

$$h'(\mu) = 1/\sqrt{g(\mu)}. \quad (3.7)$$

In case of a Rayleigh distribution, the mean and variance are given in (3.2) and (3.3), respectively. So

$$g(\mu) = 2\sigma^2 - \mu^2, \quad (3.8)$$

substituting  $\sigma^2 = (2/\pi)\mu^2$  in the above expression we get

$$g(\mu) = \left(\frac{4-\pi}{\pi}\right)\mu^2. \quad (3.9)$$

Let us define  $C = \frac{4-\pi}{\pi}$ , so we have

$$h'(\mu) = \frac{1}{\sqrt{C}\mu}, \quad (3.10)$$

therefore

$$h(\mu) = \frac{1}{\sqrt{C}}\log(\mu). \quad (3.11)$$

In general the forward VST is

$$h(u) = \frac{1}{\sqrt{C}}\log(u), \quad (3.12)$$

where  $u$  denotes the input data. Let us define  $h(u) = D$ , the transformed input, in which the variance is stabilized. Now the noise is un-correlated with data, in the sequel the distribution resembles an additive Gaussian distribution. Therefore, we can apply the models proposed for additive Gaussian noise to remove the data-independent noise from the image. Here, a non-local TV model by Gilboa and Osher (2008) is used along with split-Bregman iteration scheme for restoring images while preserving the local gradient variations in the image. Now the restoration is performed in the transformed domain, therefore the data has to be transformed back to the original domain by the inverse variance stabilizing transform. An algebraic inverse for the VST can be written as

$$\hat{u} = e^{h(u)\sqrt{C}}, \quad (3.13)$$

where  $\hat{u}$  is the restored version of the data.

### 3.2.2 The formulated variational models for Rayleigh distributed noise

Variational methods, non-local regularizers, and their features have already been discussed in the Section 1.5. The variational approaches for data independent noise models have been already discussed in previous chapters. Moreover, non-local TV based methods using split Bergman formulation are proposed for additive as well as multiplicative noise set-ups, see Getreuer (2012b); Dong et al. (2012), respectively. Precisely, in Dong et al. (2012) the authors consider a multiplicative Gamma noise distributed

image from ultrasound and radar applications. In this section, models to handle data-dependent multiplicative Rayleigh noise distribution along with linear blurring artifact that are commonly found in ultrasound medical images and radar images (due to the image averaging process) are introduced. Two non-local variational frameworks have been designed for restoring images from Rayleigh distributed noise and linear blurring defects. The PDF for a Rayleigh distribution was given in (3.1).

### Model II

The energy formulation for a Rayleigh distribution from the MAP estimate can be written as: (see Appendix B.2 for the derivation of the MAP estimate)

$$\min_u \left\{ \int_{\Omega} \left( \frac{u_0^2}{2u^2} + 2\log u \right) dx dy + \frac{\lambda}{2} \int_{\Omega} \phi(u) dx dy \right\}. \quad (3.14)$$

Assuming regularization as  $J_{NLTV}(u)$  (see Section 1.5.3), we can rewrite the above expression as

$$\min_u \left\{ \int_{\Omega} \left( \frac{u_0^2}{2(u)^2} + 2\log(u) \right) dx dy + \frac{\lambda}{2} J_{NLTV}(u) \right\}. \quad (3.15)$$

Let us define  $H(u) = \frac{u_0^2}{2(u)^2} + \log(u)$ , for denoising problem and  $H(u) = \frac{u_0^2}{2(Ku)^2} + \log(Ku)$ , for denoising and deblurring problem. Here  $Ku$  denotes a linear convolution of Gaussian kernel  $K$  with image  $u$ , as linearity and shift invariance is assumed for the operator  $K$  under the Fredholm's first kind integral equation. The gradient descent equation for (3.15) is:

$$u_{n+1} = u_n + \Delta t (-\lambda \nabla_{NL}(\nabla_{NL} u \phi'(|\nabla_{NL} u|^2(x))) + H'(u)), \quad (3.16)$$

where  $H'(u) = K^* \left( -\frac{u_0^2}{(Ku)^3} + \frac{1}{Ku} \right)$ . Here we note that the regularization parameter  $\lambda$  generally appears in the data-fidelity term (though it has been attached to the regularization term in the above expression), in later part, it will be attached to the data-fidelity term. However, the position of this parameter does not affect the evaluation process. A close observation of the above model reveals the fact that the fidelity term (first term in the functional (3.15)) is conditionally convex which leads to a suboptimal solution or we may get stuck in a local minima eventually. The proposed model is analyzed for the existence of a unique solution in Appendix A.4.

### Model III

The total BV norm was used for image restoration with split Bergman iteration scheme for additive noise in Liu and Huang (2011). Here, let us borrow the concepts to redefine

the regularization term for restoring multiplicative Rayleigh distributed noisy data. The revised formulation under the non-local TBV norm appears as

$$\min_{u \in BV(\Omega)} \left\{ \int_{\Omega} \left( \frac{u_0^2}{2(Ku)^2} + 2 \log(Ku) \right) dx dy + \frac{\lambda}{2} \|\nabla_{NL} u\|_1 + \frac{\theta}{2} \|u\|_2^2 \right\}. \quad (3.17)$$

Assume  $z = \log(u)$  and consider the image in the log domain (also attach the regularization parameter  $\lambda$  to the fidelity term as usually done) and further define  $H(z) = \lambda \sum_i e^{2(z_{0i} - Kz_i)} + 2Kz_i$ , (for a discrete image), for a discrete image let us drop the integration and assume a summation (without losing the generality we are further dropping the summation sign to avoid abuse in the notation). So we have

$$\min_z \left\{ H(z) + \|\nabla_{NL} z\|_1 + \frac{\theta}{2} \|z\|_2^2 \right\}. \quad (3.18)$$

The steepest descent/artificial time-marching scheme used for providing the solution to the minimization problem converges slowly and further the convergence depends heavily on the parameter  $\lambda$  in (3.16) and (3.17). In the following section, to overcome these drawbacks, split-Bregman numerical approach (for convex minimization problems) has been introduced.

### 3.2.3 Split-Bregman iteration scheme for the proposed models

As discussed earlier, one of the major issues with gradient descent/time marching scheme is its slow convergence rate and the dependency of the solution on the regularization parameter  $\lambda$ . The optimal choice of  $\lambda$  is crucial in getting the desired output. These issues were addressed to a considerable extent in subsequent works. Faster numerical solvers are being analyzed over the last few years to solve TV optimization model, which have already been discussed in Section 2.4.2, Chapter 2. Split-Bregman method neutralizes the effect of the regularization parameter and provides a faster convergence (Goldstein et al. (2010)). These properties make it a good choice. In this section, the split-Bregman scheme is formulated for the Rayleigh noise under two different regularization priors, the details of split-Bregman formulation is found in Goldstein et al. (2010). Split-Bregman scheme for the additive Gaussian noise model has been used in Model I.

#### Model II

The MAP estimation for Rayleigh noise has already been derived in the previous section, to ensure continuity we recall the expression in case of a non-local TV regulariza-

tion:

$$\min_{u \in BV(\Omega)} \left\{ \int_{\Omega} \left( \frac{u_0^2}{2(Ku)^2} + 2 \log(Ku) \right) dx dy + \frac{\lambda}{2} J_{NLTV}(u) \right\}. \quad (3.19)$$

Now to make the fidelity term in the above expression convex, let us define  $Kz = \log Ku$ . As we know that the Rayleigh distribution is multiplicative, we have  $u_0 = (Ku)n$ , therefore  $\log(u_0) = \log(Ku) + \log(n)$  which implies  $z_0 = Kz + n$ , this leads to the following formulation

$$\min_u \left\{ \int_{\Omega} \lambda e^{2(z_0 - Kz)} + 2Kz dx dy + \|\nabla_{NL} z\|_1 \right\}. \quad (3.20)$$

Since we deal with discrete images  $z_i$  let us define  $H(z) = \lambda \sum_i e^{2(z_0 - Kz_i)} + 2Kz_i$ , (here the regularization parameter  $\lambda$  is attached with the data-fidelity term), so we have

$$\min_z \left\{ H(z) + \|\nabla_{NL} z\|_1 \right\}. \quad (3.21)$$

Proceeding further with the Bregman iteration scheme formulation as mentioned above, we get the unconstrained minimization problem:

$$\min_{p, z} \left\{ H(z) + \|\nabla_{NL} p\|_1 + \frac{\gamma}{2} \|p - z\|_2^2 \right\}, \quad (3.22)$$

(here we note that the constraint  $p = z$  was added to the above functional, as it is tedious to derive the split-Bregman process for the non-linear function “ $\log u$ ”). It follows that

$$(p^{k+1}, z^{k+1}) = \min_{p, d} \left\{ H(z) + \|\nabla_{NL} p\|_1 + \frac{\gamma}{2} \|p - z\|_2^2 \right\}, \quad (3.23)$$

where  $\gamma \in (0, \infty)$ . Now by splitting the above problem into two subproblems  $p$ -subproblem and  $z$ -subproblem, respectively we have

$$p^{k+1} = \min_p \|\nabla_{NL} p\|_1 + \frac{\gamma}{2} \|p - z\|_2^2, \quad (3.24)$$

$$z^{k+1} = \min_z H(z) + \frac{\gamma}{2} \|p - z\|_2^2. \quad (3.25)$$

Now further adding one more constraint to the  $p$ -subproblem i.e.  $\nabla_{NL} p = d$ , we get

$$(p^{k+1}, d^{k+1}) = \min_{d, p} \left\{ \|d\|_1 + \frac{\gamma}{2} \|p - z\|_2^2 + \frac{\beta}{2} \|d - \nabla_{NL} p - b^k\|_2^2 \right\}, \quad (3.26)$$

where  $b^{k+1} = b^k + (\nabla_{NL} p - d^{k+1})$  and  $\beta$  is a positive scalar parameter. By further splitting the above problem into  $p$ -subproblem and  $d$ -subproblem we have

$$p^{k+1} = \min_p \left\{ \frac{\gamma}{2} \|p - z\|_2^2 + \frac{\beta}{2} \|d - \nabla_{NL} p - b^k\|_2^2 \right\}, \quad (3.27)$$

$$d^{k+1} = \min_d \left\{ \|d\|_1 + \frac{\beta}{2} \|d - \nabla_{NL} p - b^k\|_2^2 \right\}. \quad (3.28)$$

The minimizer for  $p$ -subproblem can be found by taking the first variation of the expression with reference to  $p$  i.e

$$0 = \beta \nabla_{NL} (d - \nabla_{NL} p - b^k) + \gamma(p - z), \quad (3.29)$$

where  $\nabla_{NL}$  denotes the non-local divergence, therefore we have

$$p^{k+1} = \frac{1}{\gamma I - \beta \Delta_{NL}} (\gamma z^{k+1} - \beta \sqrt{w_{i,j}} (d_{i,j} - d_{j,i} - b_{i,j}^k + b_{j,i}^k)). \quad (3.30)$$

Since the matrix in the denominator of the above expression is diagonally dominant it can be solved using Gauss-Seidel iteration scheme. On the other-hand the  $d$  - *subproblem* is solved using the shrinkage operator

$$d^{k+1} = \text{shrink}(\nabla_{NL} p + b^k, 1/\beta), \quad (3.31)$$

where shrink operator is

$$\text{shrink}(x, y) = \frac{x}{|x|} \max(|x| - y, 0). \quad (3.32)$$

Now the  $z$  - *subproblem* can be solved by taking the first variation of the subproblem in (3.25) with reference to  $z$  i.e,

$$0 = H'(z) - \gamma(p - z). \quad (3.33)$$

Now one can use the Newton method ( $z^{n+1} = z^n - f(z)/f'(z)$ , for a function  $f(z)$ ) to find the solution for the above problem i.e.

$$z^{k+1} = z^k - \frac{H'(z) - \gamma(p - z)}{H''(z) + \gamma}. \quad (3.34)$$

### Model III

A split-Bregman formulation for the total bounded variation expression (given in (3.18)) is designed here. To this end let us introduce an auxiliary constraint that is  $p = z$ .

Adding the constraint as a  $L^2$  penalty term in (3.18) gives

$$(z^{k+1}, p^{k+1}) = \min_{z, p} \left\{ H(z) + \|\nabla_{NL} p\|_1 + \frac{\theta}{2} \|p\|_2^2 + \frac{\gamma}{2} \|p - z\|_2^2 \right\}. \quad (3.35)$$

Now splitting this into two sub-problems we get  $z$  - *subproblem* and  $p$  - *subproblem*:

$$\min_z \left\{ H(z) + \|p - z\|_2^2 \right\}. \quad (3.36)$$

$$\min_p \left\{ \|\nabla_{NL} p\|_1 + \frac{\theta}{2} \|p\|_2^2 + \frac{\gamma}{2} \|p - z\|_2^2 \right\}, \quad (3.37)$$

further adding the constraint  $d = \nabla_{NL} p$  in the above  $p$  - *subproblem* we get

$$\min_{p, d} \left\{ \|d\|_1 + \frac{\theta}{2} \|p\|_2^2 + \frac{\gamma}{2} \|p - z\|_2^2 + \frac{\beta}{2} \|d - \nabla_{NL} p - b^k\|_2^2 \right\}, \quad (3.38)$$

where  $b^{k+1} = b^k + (\nabla_{NL} p - d^{k+1})$ . By splitting the above problem into two subproblems we have

$$\min_d \left\{ \|d\|_1 + \frac{\beta}{2} \|d - \nabla_{NL} p - b^k\|_2^2 \right\}, \quad (3.39)$$

and

$$\min_p \left\{ \frac{\theta}{2} \|p\|_2^2 + \frac{\gamma}{2} \|p - z\|_2^2 + \frac{\beta}{2} \|d - \nabla_{NL} p - b^k\|_2^2 \right\}. \quad (3.40)$$

Now taking the first variation of the above functional with respect to  $p$  gives,

$$\theta p + \gamma p - \gamma z + \beta \nabla_{NL}(d - b) - \beta \Delta_{NL} p = 0, \quad (3.41)$$

i.e.

$$p^{n+1} = \frac{1}{(\theta I + \gamma I - \beta \Delta_{NL})}(\gamma z - \beta \nabla_{NL}(d - b^{k+1})), \quad (3.42)$$

and using Gauss-Seidel method we get a solution for  $p$ -subproblem. The  $d$ -subproblem can be solved using the shrinkage operator (in (3.32)) and  $z$ -subproblem is solved using the Newtons method as done in (3.34). With these formulations we can solve the optimization problem in (3.17) with split-Bregman scheme in an efficient manner.

### 3.2.4 Algorithm to implement the methods

The algorithms for both the methods (Variance stabilization and MAP estimation) introduced in this work are described below. Let us describe three algorithms to design the three proposed models (Model I, Model II and Model III)

---

#### Algorithm 4 Algorithm to implement VST method (Model I)

---

**Input**  $u_0 \leftarrow$  Image corrupted by Rayleigh noise

**Output** Restored image  $u$

- 1: Initialize parameters  $\lambda, \mu$  (scalar positive values)
  - 2:  $\varepsilon \leftarrow$  small scalar positive value ( $\varepsilon$  is assigned a value 0.004, empirically).
  - 3: Initialize  $u^0, d^0, f^0$  and  $b^0$
  - 4: Perform variance stabilization using (3.12)
  - 5: **while do**  $\|u^k - u^{k-1}\| / \|u^k\| < \varepsilon$
  - 6:      $v^{k+1} = u^k - \delta K^*(Ku^k - f^k)$
  - 7:      $u^{k+1} = \frac{\lambda v^{k+1} - \mu \nabla_{NL}(d^k - b^k)}{\lambda I - \mu \Delta_{NL}}$
  - 8:      $f^{k+1} = f^k + u_0 - Ku^{k+1}$
  - 9:      $d^{k+1} = \text{shrink}(\nabla_{NL}u + b^k, \frac{1}{\mu})$
  - 10:      $b^{k+1} = b^k + (\nabla_{NL}u - d^{k+1})$
  - 11:      $u^{k+1} = u^k$
  - 12: **end while**
  - 13: Perform an inverse variance stabilization technique in (3.13).
-



---

**Algorithm 5** Split-Bregman iteration algorithm for NLTV (Model II)

---

**Input**  $u_0 \leftarrow$  Image corrupted by Rayleigh noise

**Output** Restored image  $u$

- 1: Initialize  $p^0, z^0, d^0, b^0$
  - 2: Initialize the constants  $\gamma, \beta, \lambda$
  - 3: **while** *do not converged*
  - 4: 
$$p^{k+1} = \frac{1}{\gamma I - \beta \Delta_{NL}} (\gamma z^{k+1} - \beta \nabla_{NL}(d^k - b^k)).$$
  - 5: 
$$z^{k+1} = z^k - \frac{H'(z) - \gamma(p-z)}{H''(z) + \gamma}.$$
  - 6: 
$$d^{k+1} = \text{shrink}(\nabla_{NL} p + b^k, \frac{1}{\mu})$$
  - 7: 
$$b^{k+1} = b^k + (\nabla_{NL} p - d^{k+1}).$$
  - 8: **end while**
- 

---

**Algorithm 6** Split-Bregman iteration algorithm for NLTBV (Model III)

---

**Input**  $u_0 \leftarrow$  Image corrupted by Rayleigh noise

**Output** Restored image  $u$

- 1: Initialize  $p^0, z^0, d^0, b^0$
  - 2: Initialize the constants  $\gamma, \beta, \lambda$  and  $\theta$
  - 3: **while** *do not converged*
  - 4: 
$$p^{n+1} = \frac{1}{(\theta I + \gamma I - \beta \Delta_{NL})} (\gamma z - \beta \nabla_{NL}(d - b^{k+1}))$$
  - 5: 
$$z^{k+1} = z^k - \frac{H'(z) - \gamma(p-z)}{H''(z) + \gamma}.$$
  - 6: 
$$d^{k+1} = \text{shrink}(\nabla_{NL} p + b^k, \frac{1}{\mu})$$
  - 7: 
$$b^{k+1} = b^k + (\nabla_{NL} p - d^{k+1}).$$
  - 8: **end while**
-

### 3.3 EXPERIMENTAL RESULTS

The models introduced in this work are being numerically tested with a large volume of input images belonging to various categories. A detailed experimental evaluation is performed on this input data both quantitatively and qualitatively. The visual comparison is done for a selected set of input images corrupted with Rayleigh noise and linear blur. Furthermore, statistical analysis is performed in terms of SNR and SSIM (see Section 1.8 for details). The Rayleigh noise was incorporated (using multiplicative model) in some synthetic images to quantify the performance of various methods and for their cross comparisons. Before making the image noisy, a linear shift-invariant Gaussian blurring was performed with a preset Gaussian kernel spread. The test results are verified using a large set of images however, the results have been shown for seven different images in this work explicitly to make the explanation precise. The test images used are shown in Figure 3.3 in their original form. Different images have shown to represent different characteristics like, texture, finer details, constant intensity regions etc. An original ultrasound medical image and a SAR images are also included in the test results to verify the restoration capacity of the models with respect to the real noisy input data.

We use the following models for comparative purpose:

- Model A: The method for restoring images corrupted with Rayleigh Noise using MAP estimator and TV ( modified Aubert Ajol Model Aubert and Aujol (2008))
- Model B : The method for restoring images corrupted with Rayleigh noise using MAP estimator with NLTV and Split Bergman Shuai et al. (2015)
- Model C : The method for restoring images using MAP, Bounded-TV, Split-Bregman Liu and Huang (2011)
- Model D : Block Matching 3D filtering Dabov et al. (2007)
- Model I : The method based on Variance Stabilization, NLTV (Additive noise) and split-Bregman as in Algorithm 4

- Model II : The method for restoring Rayleigh noise using MAP Estimator, NLTV, Split-Bregman with log computation as in Algorithm 5.
- Model III : The method for restoring Rayleigh noise using MAP Estimator, Total Bounded NLTV, split-Bregman with log computation as in Algorithm 6.

The seven test images belonging to different categories i.e. “Barbara” and “peppers” (natural gray and color images), two synthetic images (artificial cartoon type images), a real ultrasound image and a real SAR image (obtained from “Sandia National Laboratories, Airborne ISR” <http://www.sandia.gov/RADAR/imagery/>) are used for the comparative study. In all these test images (except the original ultrasound/SAR images) multiplicative Rayleigh noise and Gaussian linear blur <sup>1</sup> are artificially incorporated to study the behavior of these models with reference to their response to these input images. In Figure 3.4 the restored version of the image using the proposed variance stabilization transform is provided. The PDF of the noisy and transformed images are shown in the sub-figures. As evident from these distribution functions, the variance transformed data follows an additive Gaussian distribution. The performance of various methods are demonstrated using visual representations in Figures 3.5, 3.6, 3.7 and 3.8 for images “Barbera”, “peppers” (gray-level) and two artificial images, respectively. The Barbara image has more fine structures and edges compared to other images. In Figure 3.5 we can see the restoration results of Barbara image corrupted with Rayleigh noise. The enlarged version (to show the edge and fine structure preservation) of Barbara image is shown in Figure 3.13. From these figures it is evident that all the three proposed models are successful in preserving the fine details and edges in the image. Peppers image has different levels of uniform intensity regions, in figure 3.6 results of peppers image corrupted by Rayleigh noise are shown. An enlarged portion of the image peppers is shown in Figure 3.12. The edge and structure preservation capability of various models are shown explicitly in this figure. The proposed Models II and III perform better edge and structure preservation compared to the other models as evident in these enlarged portions. To show the edge preservation two synthetic images

---

<sup>1</sup>In case of the multi-channel (color) image, the noise and blur are incorporated in each color channel separately before combining them to form the final degraded image.

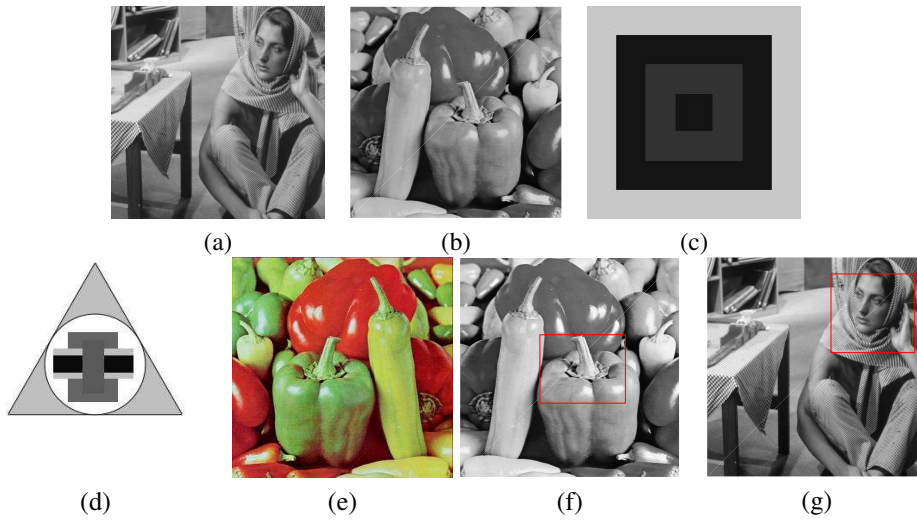


**Figure 3.3** (a),(b),(c), (d) and (e) : Test images in their original form, (f) Highlighted peppers image, (g)Highlighted Barbara image

are used, results of these images are shown in 3.7 and 3.8. For these images, all the proposed models give better results in terms of edge-preserving and sharpening. In the same manner the responses of different models to a real ultrasound image and a real SAR image are shown in Figures 3.9 and 3.10, respectively. These (real) images are found to be corrupted by Rayleigh distributed noise. For the ultrasound image in Figure 3.9, result of Model I seems to be sharper compared to others. Model II and model III successfully removed the noise in both foreground and background. In Figure 3.10, results of Lynx Synthetic Aperture Radar (SAR) image (of a railroad bridge over the Rio Grande River near Belen, NM) are shown. The rail bridge and the river are more clearly restored in all the proposed models. We note that the results shown in Figure 3.11 (“peppers”) is a RGB color/vector image (i.e  $u \in R^3$ ) and the sub-figures show the performance of various filters with reference to this multi-channel image. In similar lines we can apply these methods for the other multi-channel or multi-spectral images (from medical/satellite imagery) as well. From these visual representations it is pretty evident that proposed strategies outperform the other models in terms of noise reduction

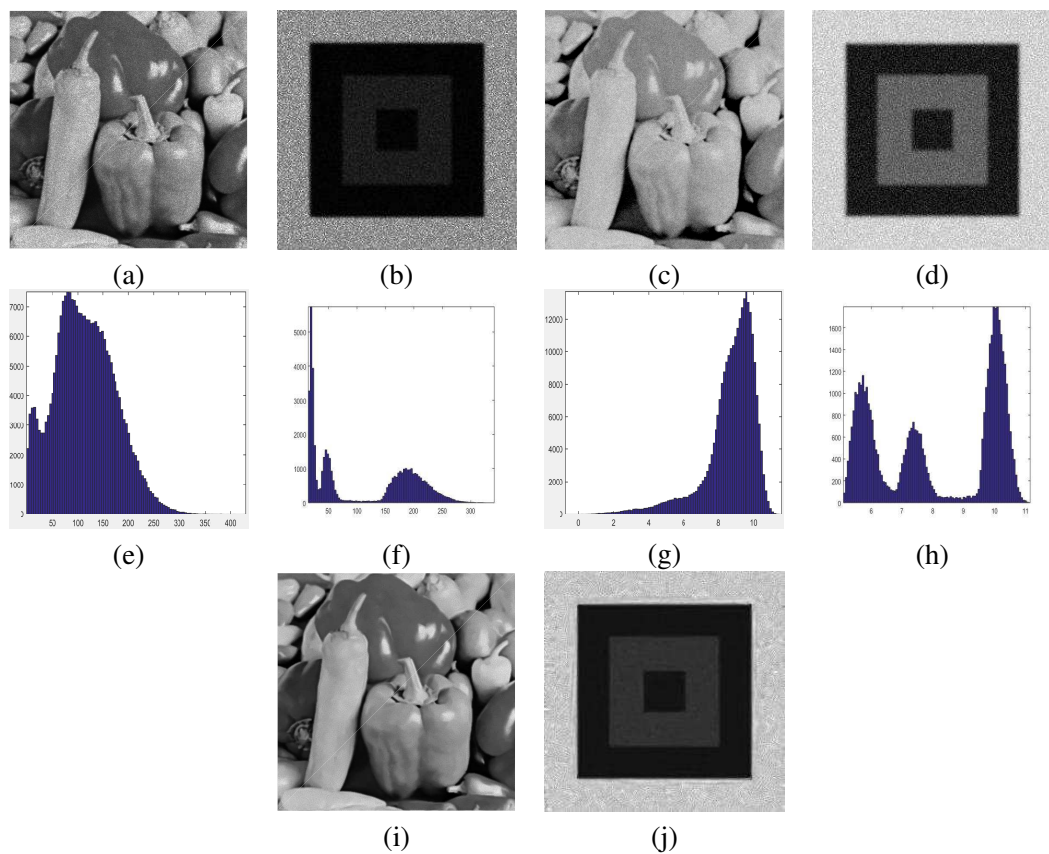


**Figure 3.4** Variance Stabilization Transform (Multiplicative Rayleigh noise variance 0.15 and blur with sigma 1.2 are incorporated to the input data): (a),(b) Input (noisy and blurry) Images (e),(f) Histograms of (a) and (b), respectively; (c),(d) Images after Variance stabilization, (g),(h) Histograms of images in (c) and (d), respectively; (i),(j) Restored images after stabilizing the variance and using NLTV



**Figure 3.5** Image “Barbara” restored using various methods (multiplicative Rayleigh noise variance of input image is 0.15 and standard deviation of blurring kernel is 1.2): (a): Noisy image; images restored using (b) Model A; (c) Model B ;(d) Model C ;(e) Model D (f) Model I (g) Model II and (h) Model III

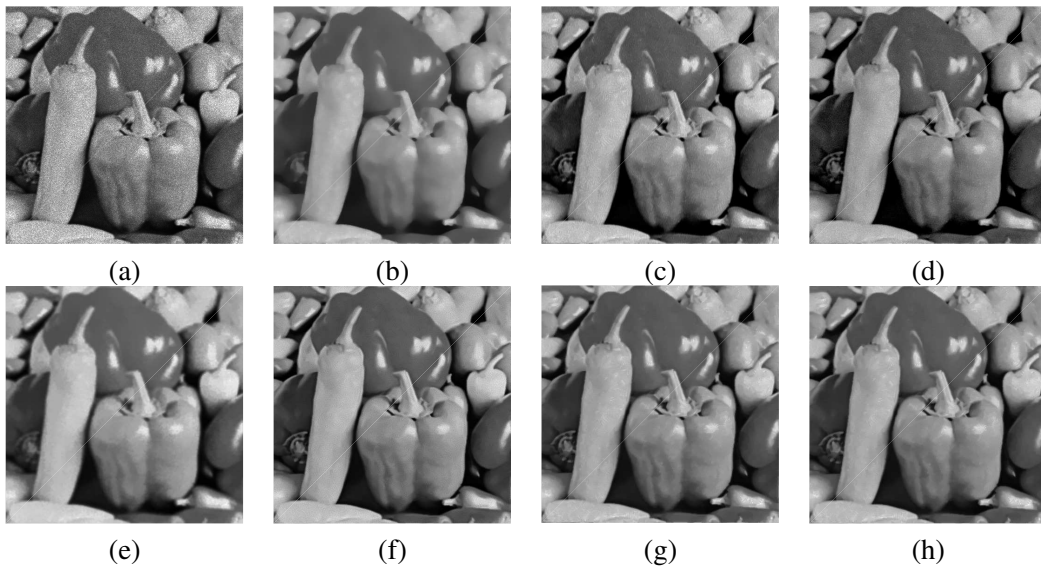


**Figure 3.6** Image “Pepper” (gray-level) restored using various methods (multiplicative Rayleigh noise variance of input image is 0.15 and standard deviation of blurring kernel is 1.2): (a): Noisy image; images restored using (b) Model A; (c) Model B ;(d) Model C ;(e) Model D (f) Model I (g) Model II and (h) Model III

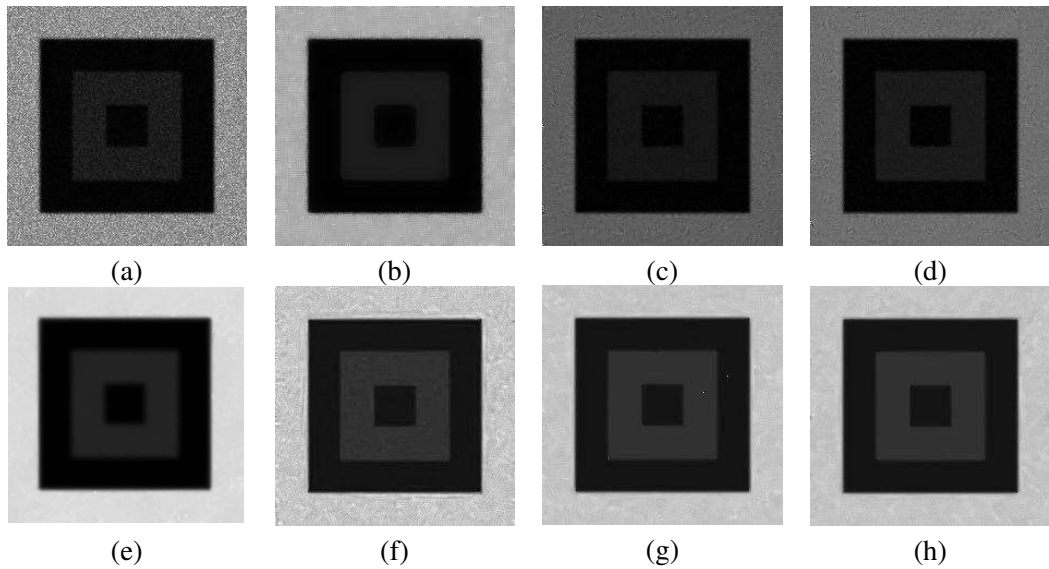


**Figure 3.7** Image “Synthetic Image 1” restored using various methods (multiplicative Rayleigh noise variance of input image is 0.15 and standard deviation of blurring kernel is 1.2): (a): Noisy image; images restored using (b) Model A; (c) Model B ;(d) Model C ;(e) Model D (f) Model I (g) Model II and (h) Model III

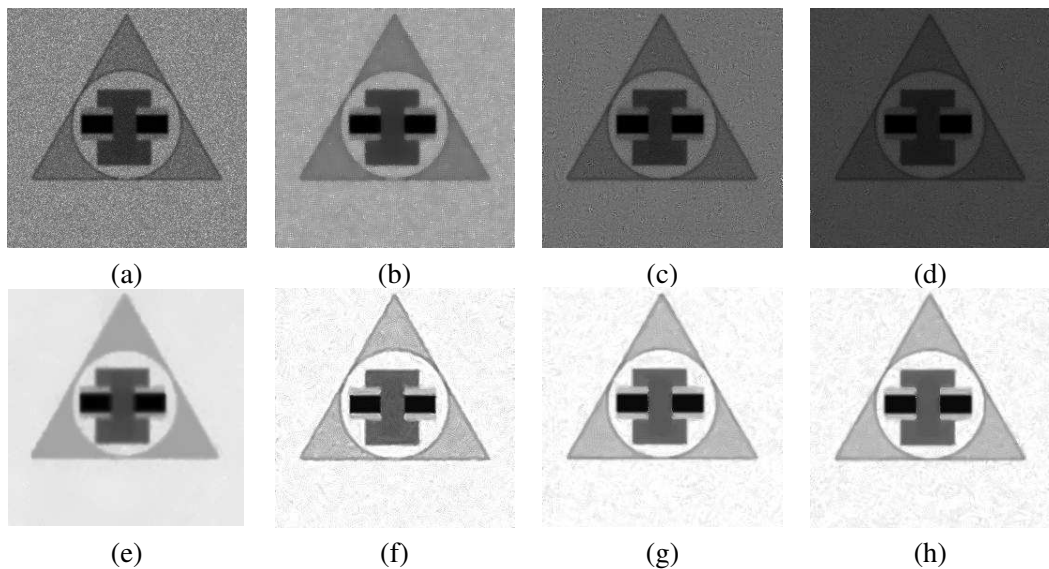


**Figure 3.8** Image “Synthetic Image 2” restored using various methods (multiplicative Rayleigh noise variance of input image is 0.15 and standard deviation of blurring kernel is 1.2): (a): Noisy image; images restored using (b) Model A; (c) Model B ;(d) Model C ;(e) Model D (f) Model I (g) Model II and (h) Model III

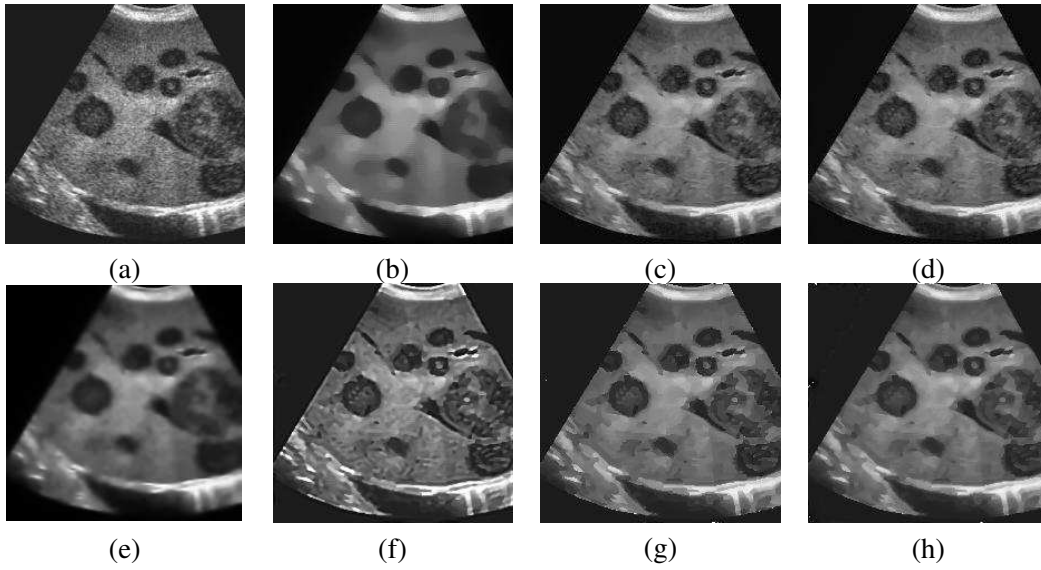


**Figure 3.9** Image “Real ultrasound image” restored using various methods: (a): Noisy image ; Images restored using (b) Model A; (c) Model B ;(d) Model C ;(e) Model D (f) Model I (g) Model II and (h) Model III

and detail preservation.

Further, a statistical analysis is performed with regards to the statistical measure (SNR) described in Section 1.8. The response of various methods for the statistical measure SNR (in dB) is shown in Table 3.1. The SNR values corresponding to the proposed methods (Model I, Model II and Model III) are higher than the comparative models (Model A, B and C). Among the proposed ones, Model I has slightly better SNR value (in an average case) because stabilization of the variance makes the noise data uncorrelated before the regularization process, eventually leading to a higher smoothing. Similarly the mean-SSIM values ([0-1]) give a notion of structure, contrast and edge preservation capability of the model under consideration (here the value 1 stands for an ideal preservation). The SSIM values are tabulated in Table 3.2. From these values one can infer that the proposed models (Model I, II and III) illustrate a good performance in terms of structure preservation along with the denoising. Though the Models II and III performs slightly on the lower side in terms of SNR, they perform better in terms



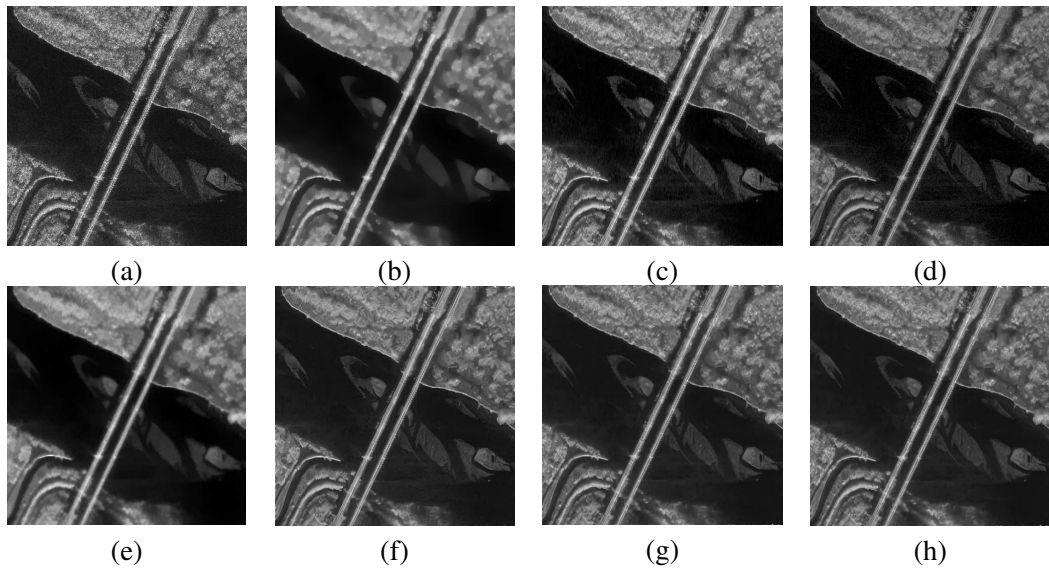


**Figure 3.10** Image “Real SAR image-2” (Lynx Synthetic Aperture Radar (SAR): Courtesy of Sandia National Laboratories, Airborne ISR ) restored using various methods: (a): Noisy image ; images restored using (b) Model A; (c) Model B ;(d) Model C ;(e) Model D (f) Model I (g) Model II and (h) Model III

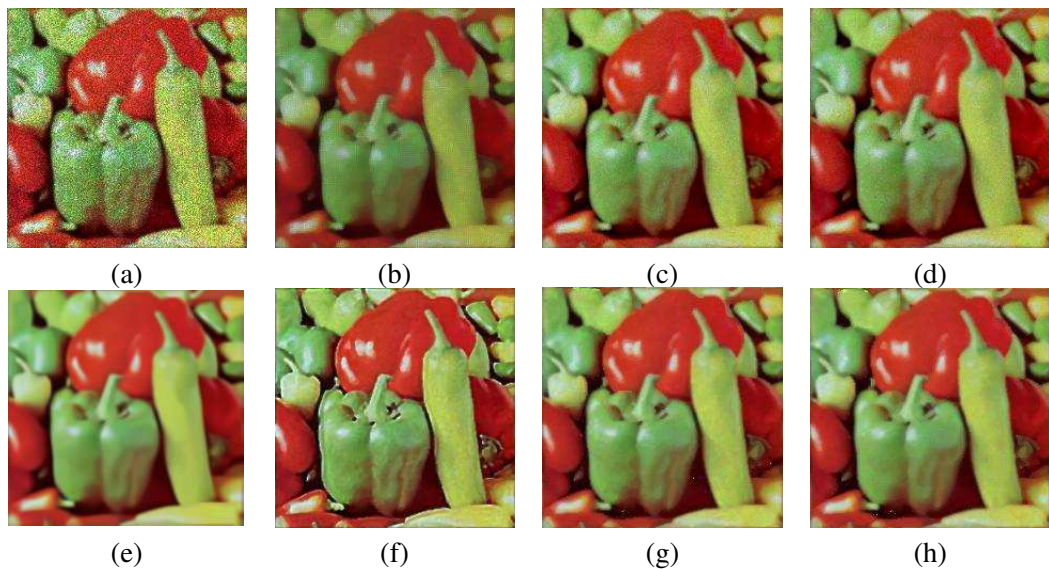


**Figure 3.11** Vector Image “color image” restored using various methods: (a): Noisy image ; image restored using (b) Model A; (c) Model B ;(d) Model C ;(e) Model D (f) Model I (g) Model II and (h) Model III

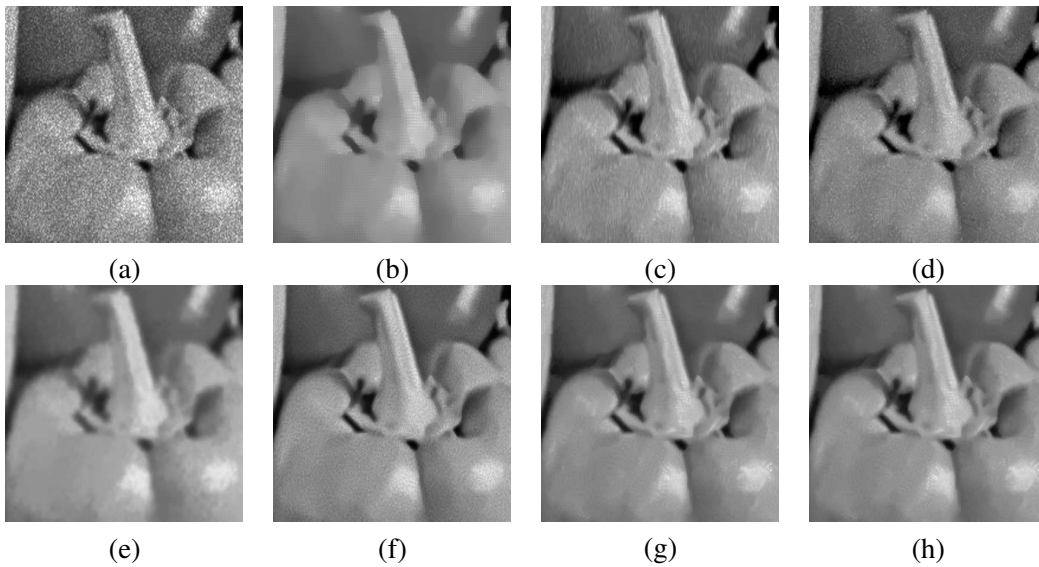


**Figure 3.12** Enlarged portion of the image peppers highlighted in Figure 3.3, (a)Input image corrupted with noise variance of 0.15, linear blur of  $\sigma=1.2$ , restored using (b) Model A; (c) Model B ;(d) Model C ;(e) Model D (f) Model I (g) Model II and (h) Model III

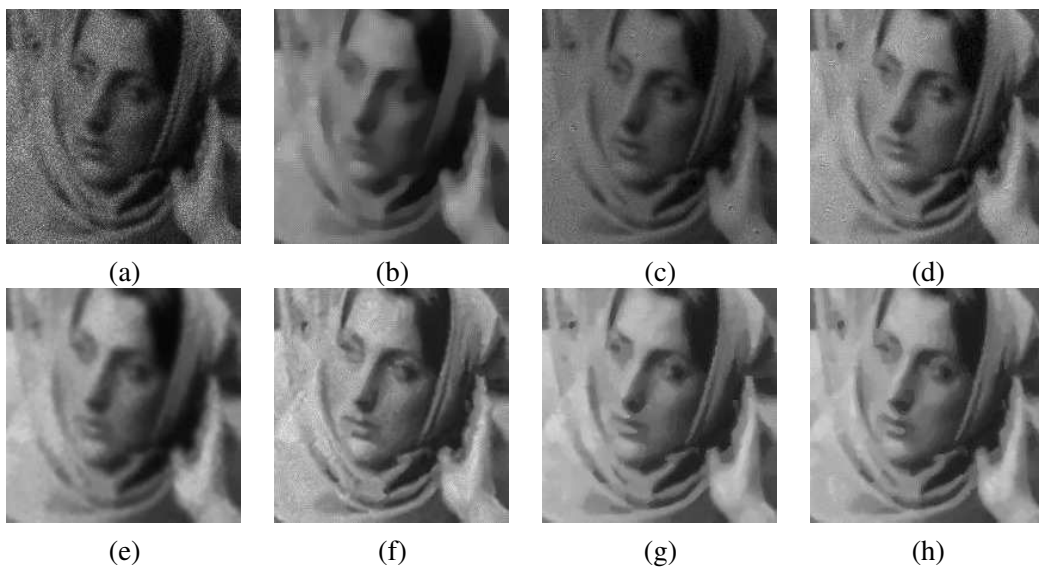


**Figure 3.13** Enlarged portion of the image 'Barbara': (a)Input image corrupted with noise variance of 0.15, linear blur of  $\sigma=1.2$ , restored using (b) Model A; (c) Model B ;(d) Model C ;(e) Model D (f) Model I (g) Model II and (h) Model III

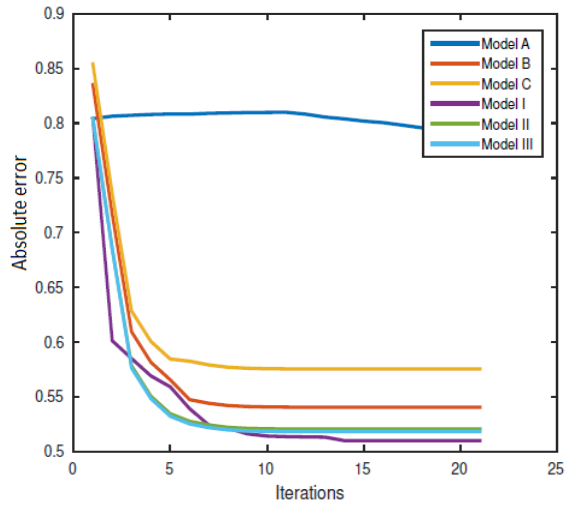


**Figure 3.14** Absolute Error verses iterations

of structure preservation. So the overall performance of the Model III is better than the other models considered for the comparative study.

The convergence analysis of various models are shown in Figure 3.14. The plot shows the variations of absolute error against each iteration of various methods for “Synthetic image 1”. The proposed Models 5 and 6 converges faster compared to the other models and the decay in error or increase in energy are found to be stable along the iterative process. The plot for models 5 and 6 almost overlays on one another (as the process is almost similar except the regularization term) so it is not explicitly visible in the plot. Further a box plot of various methods for SNR is shown in Figure 3.15. Here, 100 different test images (falling in different image categories) are used to perform the box-plot analysis. All these images are corrupted by a Rayleigh noise with noise variance 0.2. The red lines in the plot indicate the median values and the red crosses indicate the outliers. The parameters (interquartile range (IQR), whisker value etc.) are set by default in the MATLAB box-plot function. The IQR gives an indication of the dispersion of the data. From the plots shown in these figures, it is evident that the proposed models (Model II and III) give a compact plot with a median value higher than the other models (Model A-C) as mentioned earlier. The outliers are relatively less in the plots corresponding to the proposed Models II and III. Similarly, the average SNR is

**Table 3.1** SNR (in dB) evaluated for various restoration methods for different images. (The Rayleigh noise variances of the input images are {0.2, 0.1} with blur of sigma {0.8,1.5})

Image Name	Noisy Data	Model A	Model B	Model C	Model D	Model I	Model II (VST)	Model III
Barbara	{13.25, 15.90}	{16.55, 16.90}	{18.07, 17.04}	{17.75, 17.21}	{20.34, 21.04}	{17.59, 17.29}	{17.55, 17.39}	{17.66, 17.37}
Peppers (Gray-level)	{12.73, 15.09}	{15.8, 17.1}	{17.48, 19.56}	{17.92, 19.75}	{17.48, 16.93}	{19.27, 20.58}	{19.21, 20.06}	{19.81, 20.31}
Synthetic 1	{13.65, 17.64}	{18.95, 20.69}	{19.94, 18.18}	{19.75, 19.46}	{22.08, 20.39}	{21.22, 21.10}	{20.85, 20.51}	{20.86, 20.64}
Synthetic 2	{13.74, 18.20}	{17.95, 21.36}	{21.26, 19.26}	{21.10, 21.29}	{22.26, 22.2}	{21.88, 21.67}	{21.31, 22.28}	{21.65, 21.36}
Man	{13.44, 16.41}	{16.87, 17.75}	{18.55, 19.96}	{18.67, 19.98}	{20.11, 22.57}	{18.21, 19.98}	{18.89, 20.02}	{19.22, 20.34}
Girl face	{13.9, 19.06}	{21.22, 22.34}	{21.5, 22.55}	{21.5, 22.43}	{19.51, 19.81}	{19.86, 20.21}	{22.37, 22.61}	{22.41, 22.8}
Bridge	{13.25, 15.37}	{15.56, 16.23}	{15.53, 18.67}	{16.85, 19.98}	{17.26, 20.76}	{17.67, 18.75}	{16.32, 19.27}	{16.21, 19}
Baboon	{12.21, 13.6}	{14.69, 14.8}	{18.55, 20.12}	{18.63, 19.42}	{18.13, 22.03}	{18.22, 21.22}	{18.38, 19.12}	{18.02, 19.11}

**Table 3.2** SSIM evaluated for various restoration methods for different images. (The Rayleigh noise variances of the input images are {0.2, 0.3}) with blur of sigma {0.8,1.5}

Image Name	Noisy	Model A	Model B	Model C	Model D	Model I	Model II	Model III
Barbara	{0.40, 0.29}	{0.29, 0.28}	{0.51, 0.50}	{0.51, 0.5}	{0.65, 0.6}	{0.49, 0.43}	{0.52, 0.50}	{0.53, 0.50}
Peppers (Gray-level)	{0.51, 0.41}	{0.52, 0.39}	{0.58, 0.48}	{0.61, 0.5}	{0.74, 0.72}	{0.64, 0.58}	{0.68, 0.53}	{0.71, 0.58}
Synthetic 1	{0.16, 0.13}	{0.20, 0.18}	{0.22, 0.21}	{0.24, 0.22}	{0.75, 0.71}	{0.23, 0.22}	{0.25, 0.22}	{0.26, 0.23}
Synthetic 2	{0.13, 0.10}	{0.14, 0.10}	{0.21, 0.14}	{0.27, 0.22}	{0.72, 0.69}	{0.2, 0.19}	{0.28, 0.24}	{0.29, 0.24}
Man	{0.32, 0.34}	{0.35, 0.3}	{0.5, 0.54}	{0.41, 0.46}	{0.45, 0.54}	{0.48, 0.52}	{0.55, 0.6}	{0.56, 0.6}
Girl face	{0.2, 0.3}	{0.34, 0.41}	{0.53, 0.68}	{0.55, 0.63}	{0.63, 0.72}	{0.67, 0.74}	{0.62, 0.7}	{0.65, 0.69}
Bridge	{0.41, 0.38}	{0.46, 0.42}	{0.43, 0.45}	{0.44, 0.45}	{0.48, 0.43}	{0.51, 0.43}	{0.41, 0.48}	{0.45, 0.48}
Baboon	{0.3, 0.21}	{0.4, 0.32}	{0.55, 0.53}	{0.55, 0.56}	{0.56, 0.53}	{0.62, 0.63}	{0.64, 0.68}	{0.62, 0.7}

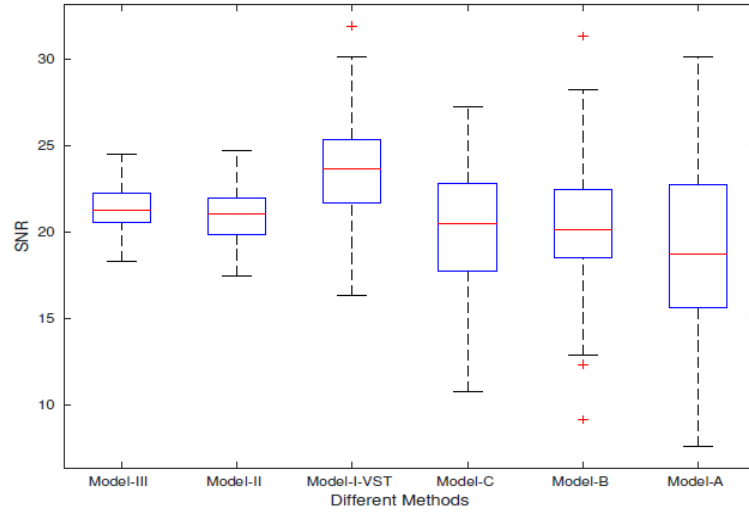


**Figure 3.15** Box-plot for various methods using SNR

high for the proposed Model I but dispersion is more compared to Models II and III. In other words, the proposed Models II and III are more stable and robust in performance when compared with the other models and Model I gives a better smoothing (higher SNR) compared to all other methods.

All the parameters used for various algorithms considered in this work are described in Table 3.3. For non-local numerical implementation, we need to set window and patch size carefully in order to get perform better performance. Usually, patch size should be nearly half of the window size. As the search window size increases, the algorithm needs more time to select similar patches in a search window. The patch size should be at least  $3 \times 3$ , smaller the patch size, better will be the structure preserving. Regularization parameters  $\lambda$  and  $\gamma$  controls the diffusion by adding back lost details in each iteration. Larger the lambda less will be the diffusion. But the very high value of  $\lambda$  and  $\gamma$  leads to less denoising.  $\mu$  controls the smoothing process. A larger value of  $\mu$  leads to over-smoothing, hence the selection of  $\mu$  should be optimal in order to get better results. The algorithm is performed with several values of  $\lambda$ ,  $\gamma$ , and  $\mu$ , the selected values given in Table 3.3 gives better performance in case of smoothing and structure preserving. For the total bounded variation algorithm, the parameter  $\theta$  is used, which also controls the smoothing by preserving fine edges and details in the image.

**Table 3.3** Parameter values used for different methods considered in this work.

Parameter	Model A	Model B	Model C	Model D	Model I	Model II	Model III
$\lambda$	0.05	0.09	0.09	2.7	0.5	20.5	16.5
$\Delta t$	0.5	-	-	-	-	-	-
$\mu$	-	0.9	1	-	0.05	4	4
$\gamma$	-	-	-	-	-	10	8
$\theta$	-	-	0.07	-	-	-	0.02
$\delta$	-	-	-	-	1.9	-	-
Patch size (for non-local TV)	-	3	3	8	3	3	3
Window size (for non-local TV)	-	5	5	-	5	5	5

Increasing the value of  $\theta$  gives better edge preserving but makes denoising poor.

### 3.4 Summary

Three variational restoration models have been proposed in this chapter for restoring ultrasound and SAR images corrupted by Rayleigh noise and linear shift-invariant blur. The Model I uses VST, which yields better smoothing thus results in high SNR values, however, due the assumption that the noise is independent of data, the structure preservation ability is limited. For an efficient smoothing, NLTV is being used in Model I, which uses a non-local scheme instead of a local scheme, thereby resulting in better structure preservation. Model II and III use NLTV and NLTBV respectively for regularizing the solution. From the literature, it may be noted that the NLTBV performs comparatively better in terms of smoothing of the noise while preserving fine details (as discussed in Section 2.4), which makes it an appropriate choice for the restoration model. Also, Model II and III are derived using the MAP estimation of the noise distribution, therefore they perform better in terms of approximation of the data. Log transformation in Model II and III make them more robust in terms of implementation. Split-Bregman iterative scheme is being used in all the proposed models, as the faster numerical schemes are relevant when handling large datasets.

Most popular imaging systems (covering both medical and satellite imagery) and two of the most common data-dependent noise contaminations (*Chi* and Rayleigh) have been discussed in previous and this chapter. Yet another common noise distortion is Poisson, which is common in some medical (X-ray , Computed Tomography(CT) and

Positron Emission Tomography(PET)), microscopic (fluorescence and confocal) and telescopic images where the images are formed as a result of a Poisson process. The next chapter is oriented towards the designing of variational model to restore Poissonian images.





## Chapter 4

# NONLOCAL VARIATIONAL APPROACH TO RESTORE POISSONIAN IMAGES

### 4.1 INTRODUCTION

In some of the important imaging applications such as fluorescence and confocal microscopy, computed tomography and optical astronomy, the camera sensors detect the incident photons in a particular interval of time. All these sensed data are converted into raw data, eventually yielding the images. However, under poor illumination and insufficient information, the sensed images are found to be contaminated by signal-dependent noise, which is normally Poisson distributed ( see Hsieh et al. (2009) for more details). Being data-dependent, the restoration becomes challenging in such scenarios. Recently many researches have been undertaken for Poisson image restoration, see Giryes and Elad (2014); Feng and Chen (2015); Li et al. (2015); Zhang and Hirakawa (2017). It has been observed from the imaging literature that, the image formation in microscopic or astronomical imaging applications resembles a Poisson process, and therefore the noise in such images are observed to follow a Poisson distribution. This chapter is focused on such image data to experimentally verify the restoration capacity of the model. Microscopic imaging applications are quite common in diverse fields, such as medicine, biological research, drug applications and metallurgical applications. Therefore, acquiring clean images is the need-of-the-hour in these applications for proper diagnosis and analysis of the data. This chapter introduces a non-local variational framework for image restoration under a Poisson degradation using an adaptive  $p - norm$  data fidelity term and its split-Bregman formulation is detailed.

### **4.1.1 Computed Tomography**

Among the most broadly used imaging techniques, Computed Tomography(CT) is the one of the technologies which use X-ray radiation to scan internal organs of the human body. The technology was first coined by Hounsfield (1973). The basic idea of CT can be drawn as in Figure 4.1. Mainly, a CT scanner has collimators, X-ray source and detectors which are placed opposite to each other. X-ray beam emitted from the source are narrowed using the collimator and passes through the target (as shown in the Figure 4.1). Some parts of the beam are absorbed or scattered after passing through the target and the rest are detected by the detectors. Next, the scanner moves across the human body and performs the reading continuously to complete one scan, which produces a slice. Further, the scanner is rotated 1 degree and the procedure repeats, and this continues till 180 degree. All the resultant images are then processed and stored in a computer for the diagnosis purpose. One slice of the CT image of a human kidney is shown in Figure 4.2. To obtain the accurate scan, the intensity of the X-ray radiation should be high. But, X-ray is harmful for human body if the dose is more (De Gonzalez et al. (2009)). Hence, the amount of radiation should be less enough to keep the scan safe. Less amount of radiation causes more noise in the raw data collected by the detectors. The number of photons collected by the detectors (under the monoenergetic and non-scattering conditions) follows the Poisson distribution (Hsieh et al. (2009)). So the noise in CT images usually follows a Poisson PDF.

### **Applications of CT**

Being an advanced technology of X-ray radiography, CT imaging helps in differentiating soft tissue structures in the human body such as lung nodules, fat, liver tissues etc. CT also helps in detection of cancer as well as the size and spatial location of a tumor. Defects in a blood vessel, damage of nervous system and also bone fractures can be detected in CT imaging. Due to these applications, image restoration and enhancement has a wide scope in the field of CT imaging.

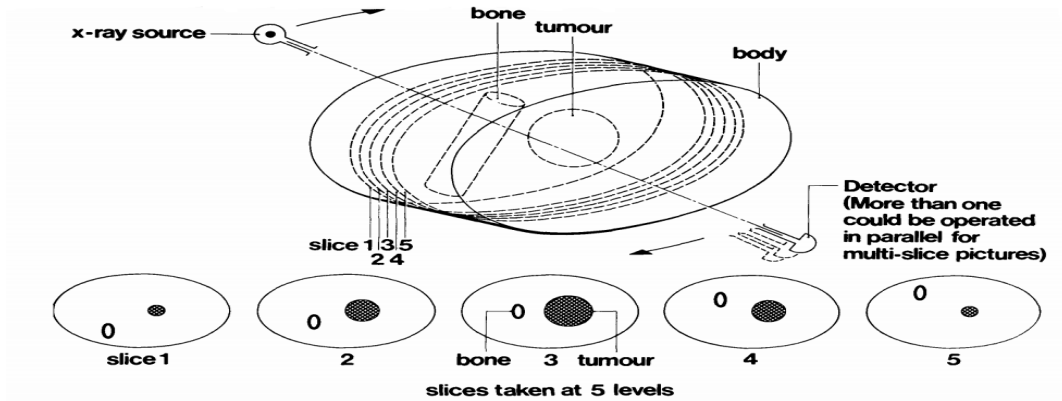


**Figure 4.1** CT imaging technique (image courtesy: Hounsfield (1973))

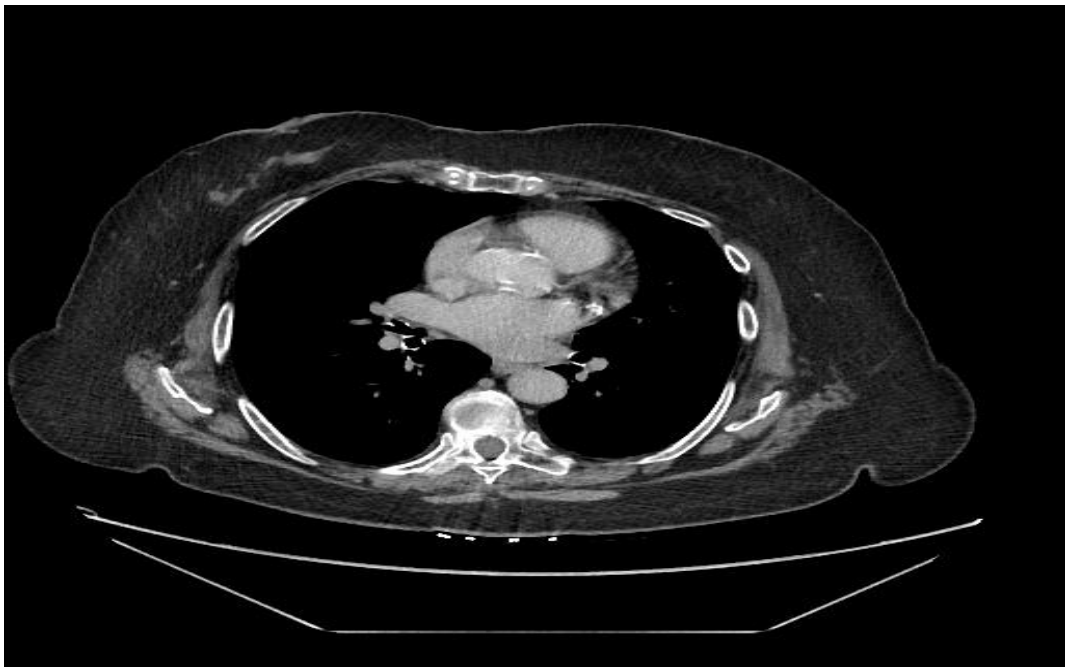


**Figure 4.2** A sample CT image slice of a human kidney (Downloaded from <https://public.cancerimagingarchive.net>)

### 4.1.2 Fluorescence and confocal microscopy

There has been an intense growth of fluorescence spectroscopy in the field of microscopic imaging in the last few decades. Most of the researches in biophysics and biochemistry use this technology. Any substance in the electronically excited state emits the luminescence light (Lakowicz (2006)). Depending on the type of electron excitation, luminescence is subcategorized into two, namely fluorescence and phosphorescence. Usually, in one second,  $10^8$  fluorescence are emitted during the excitement. Substances which emit the fluorescence are called as the fluorophores. The block diagram of a typical fluorescence microscope is given in Figure 4.3, which contains a light source (to illuminate the substance), objective lenses (to focus or spread the light) and a detector (to receive the fluorescence light emitted by the substance) which is usually a CCD camera (expanded as Charge Coupled Device) (Kempen (1999)). A light wave of suitable wavelength is emitted from the source and focused on the target object using the objective lens. The illuminated fluorophore/object emits the fluorescence light which is less intensive than that of the source light. These reflected waves are detected by the CCD camera and converted into a two dimensional image. Due to the low intensity, the output image is usually disturbed by the noise, which is normally Poisson distributed. The wide-field illumination in the fluorescence microscopy helps in capturing the whole sample simultaneously, but since the substance need not to have homogeneous regions, some portions goes out of focus (Kempen (1999)), which leads to blurring in the captured image.

To overcome this drawback of wide-field illumination in fluorescence imaging, the illumination is made into pinpoint by placing a pinhole in front of the detector, which is known as the confocal microscopy. In this methodology, single point of a target substance is scanned at a time, leading to a sharp image in the output. Though the resultant image is sharp in case of confocal microscopy, the axial resolution is less compared to the fluorescence microscope.

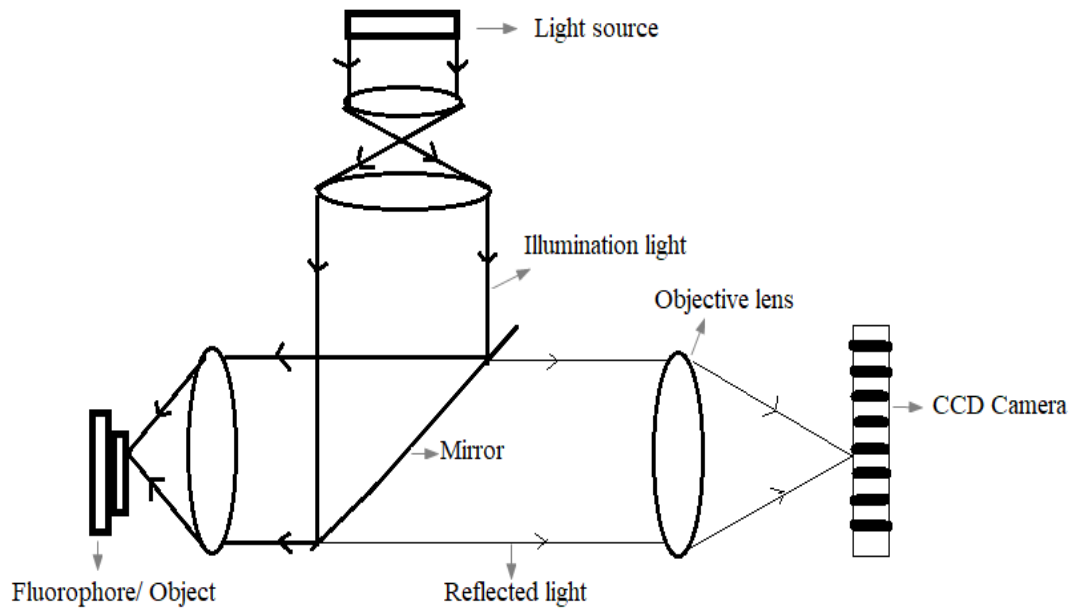


**Figure 4.3** Block diagram of a fluorescence microscope (Kempen (1999))

## Applications

The present technology enhanced the use of fluorescence microscopy to the field of biotechnology, medical diagnostics, DNA sequencing, genetic analysis etc. Since the fluorescence detection is very sensitive, it can replace the radioactive detectors which are much expensive and needs more precautions against the radiation (Mondal and Di-spro (2013)). Microscopy is also commonly used in the field of molecular and cellular imaging. Image restoration in the field of fluorescence/confocal microscopy is a challenging task because the data of interest in these images are very tiny and sensitive. So the scope for image restoration is increasing day by day. Figure 4.4 shows the still image from the collection in which the amoeba is trying to eat yeast cell (image downloaded from <http://www.cellimagelibrary.org/images/12654>).

### 4.1.3 Variational methods for Poisson restoration

As already discussed in the first chapter, data uncorrelated and correlated noise alleviations have been well studied in the image restoration literature under the variational



**Figure 4.4** Fluorescence image of an amoeba

framework. Poisson noise reduction is a major subject of interest in studies reported in the works: Le et al. (2007); Wang and He (2017). A TV minimization using a MAP estimation process is being employed in these works to restore the data. An elaborate review of image restoration under Poisson corrupted noise can be seen in Bertero et al. (2009). Yet another TV regularization combined with Richardson-Lucy algorithm for deblurring 3D confocal images has been introduced in Dey et al. (2006). In the similar lines, an iterative reconstruction algorithm by using maximum likelihood estimator is reported in Benvenuto et al. (2008) for mixed Poisson-Gaussian noise and a deconvolution iterative model using variable splitting is introduced in Chakrabarti and Zickler (2012). The other notable models include the PURE-LET(Poisson-Gaussian Unbiased Risk Estimate - Linear Expansion of Thresholds methodology designed generally for transform-domain thresholding) based denoising model in Luisier et al. (2011), a variance stabilization model by Makitalo and Foi in Makitalo and Foi (2013b) and a variational framework with TV and Kullback-Leibler divergence (for Poisson noise) in Lanza et al. (2014). Furthermore, a comparative study of a combined TV and wavelet restoration for the Poisson noise has been performed in Kais et al. (2016). Another study regarding Poisson noise reduction in low dose CT images using modified ROF

model is provided in Zhu et al. (2012). Similarly, Ferdinand et al. (Deger et al. (2015)) worked on denoising of hyperspectral images corrupted by Poisson noise which occurs due to the photon correction after the acquisition phase.

The state-of-the-art image restoration models are based on the non-local averaging framework introduced in Buades et al. (2005) and its variants Dabov et al. (2007). The non-local variational frameworks for Poisson data include Non-Local Principal Component Analysis (NLPCA) method proposed in Salmon et al. (2014) and the non-local TV restoration model proposed in Zhang et al. (2014). The model in Zhang et al. (2014) uses a  $L^2$  constraint, which results in over-smoothing of the data. Moreover, in Liu et al. (2017) the authors propose a Euler-Elastica based variance stabilization approach for Poisson distribution. This model works reasonably well in low peak noise, but sometimes fails to preserve fine structures in case of high peak noise (a higher peak-value denotes a lower degradation and vice-versa).

Motivated by some of these drawbacks, a non-local  $p - norm$  regularization model to handle Poisson noise for both low and high peak distributions has been derived in this chapter. The diffusion in this model is driven by a  $p - norm$  regularizer which controls the behavior of diffusion, in other words, the diffusion magnitude is characterized by the  $p - norm$  value of the filter.

#### 4.1.4 Non-local $p - norm$ filter

The regularizer considered in this chapter is adapted from the anisotropic non-local  $p - norm$  filter (see Ta et al. (2007) for details). The functional of this model is given by,

$$E(u, u_0, \lambda, p) = J_w(u, p) + \frac{\lambda}{2} (\|u - u_0\|_{L^2}^2 - |\Omega| \sigma^2), \quad (4.1)$$

where

$$J_w(u, p) = \frac{1}{2p} \int_{\Omega \times \Omega} (w_{xy})^{\frac{p}{2}} |u(y) - u(x)|^p dx dy. \quad (4.2)$$

When  $p = 1$ , above functional approaches to a non-local TV proposed in Gilboa and Osher (2008) i.e

$$J_w(u, 1) = \frac{1}{2} \int_{\Omega \times \Omega} \sqrt{w_{xy}} |u(y) - u(x)| dx dy. \quad (4.3)$$

The diffusion approaches a TV when  $p = 1$  and over-smooth the structure when  $p = 2$ . The behavior is studied for  $p$  values less than one and between the open range

(1, 2). The details about the analysis are provided in the subsequent sections. In the next section, we reformulate the above scheme for Poisson noise distribution and seek a solution using fast numerical solver which is devoid of the time step and regularization parameter.

## 4.2 RESEARCH WORK

This section introduces a non-local variational model using the MAP estimator of the Poisson PDF (see Appendix B.3). The solution to the minimization problem in (4.3) is sought under the explicit time marching scheme. This model is derived for a data-dependent Poisson noise, where we try to minimize the  $L^2$  error under the assumption that the noise is random and its spectrum is constant (the noise such as average white noise). Furthermore, the solution is sought using an explicit scheme which results in slow convergence and moreover, the convergence depends on the regularization parameter and the time-step chosen for the model.

### 4.2.1 Non-local variational model for Poisson noise reduction

In this study, we propose to fine-tune the model in (4.1) for Poisson noise distribution and intends to solve the model using fast numerical solver i.e. split-Bregman iteration scheme. The tuning of the model for Poisson noise distribution is performed using the MAP estimator derived using Poisson PDF, please refer Appendix B.2 for the details of the derivation. Now the proposed functional for a Poisson noise process under a non-local framework takes the form

$$\min_{u \in BV(\Omega)} \left\{ \frac{\lambda}{2} \int_{\Omega} (u - u_0 \log u) dx dy + J_w(u, p) dx dy \right\}. \quad (4.4)$$

The E-L equation for above functional is given by,

$$J'_w(u, p) + \lambda \frac{u - u_0}{u} = 0, \quad (4.5)$$

where

$$J'_w(u, p) = \sum_{x \sim y} w_{xy}^{\frac{p}{2}} (|u(y) - u(x)| + \varepsilon)^{p-2} (u(y) - u(x)).$$

The diffusion term  $J'_w(u, p)$  eventually performs the smoothing in noisy regions, whereas the data-fidelity term is responsible for the minimal deviation from the original data. Here we can notice that, when  $0 < p < 1$ , the resultant images are sharper, whereas for



$p > 1$  they are smoother. The effect of  $p$  on the output is experimentally verified in the next section. As known from the literature, as  $p$  value increases the model tries to approximate images with smoother functions, eventually yielding smoother images. The regularization parameter  $\lambda$  controls the noise reduction and data-preservation behavior of the model. Therefore, the selection of  $\lambda$  is crucial in getting the desired output. Here we chose the split-Bregman iteration scheme, for solving the model, due to its fast converging nature. Moreover, the convergence doesn't depend on the time step and the regularization parameter. Now following the split-Bregman scheme, let us define the constraint  $d = \nabla_{NL}^p u$ , and rewrite the proposed minimization problem (by additionally employing an auxiliary parameter  $b$ ):

$$(u^{k+1}, d^{k+1}) = \min_{u,d} \left\{ \|d\|_p^p + \frac{\lambda}{2} \|u - u_0 \log u\|_2^2 + \frac{\beta}{2} \|d - \nabla_{NL}^p u - b\|_2^2 \right\}. \quad (4.6)$$

Further, splitting above equation into  $u, d$  and  $b$  subproblems, we get,

$$u^{k+1} = \min_u \left\{ \frac{\lambda}{2} \|u - u_0 \log u\|_2^2 + \frac{\beta}{2} \|d^k - \nabla_{NL}^p u - b^k\|_2^2 \right\},$$

$$d^{k+1} = \min_d \left\{ \|d\|_p^p + \frac{\beta}{2} \|d^k - \nabla_{NL}^p u - b^k\|_2^2 \right\}, \quad (4.7)$$

$$b^{k+1} = b^k + \nabla_{NL}^p u - d^{k+1}. \quad (4.8)$$

Using Euler-Lagrangian derivative to solve the above minimization problem, we get,

***u-subproblem***

$$\lambda \left(1 - \frac{u_0}{u}\right) + \beta \nabla_{NL}^p \cdot (d^k - \nabla_{NL}^p u - b^k) = 0, \quad (4.9)$$

$$\lambda - \beta \Delta_{NL}^p u = \lambda \frac{u_0}{u} - \beta \nabla_{NL}^p \cdot (d^k - b^k), \quad (4.10)$$

$$u^{k+1} = \frac{\lambda \frac{u_0}{u^k} - \beta \nabla_{NL}^p \cdot (d^k - b^k)}{\frac{\lambda}{u^k} I - \beta \Delta_{NL}^p}. \quad (4.11)$$

Since  $\frac{\lambda}{u^k} I - \beta \Delta_{NL}^p$  is diagonally dominant, Gauss-Seidel method is applied to solve the above subproblem.

***d-subproblem***

$$d^{k+1} = \text{shrink}(\nabla_{NL} u + b^k, 1/\beta), \quad (4.12)$$

the *shrink* function is defined as,

$$\text{shrink}(x, y) = \frac{x}{|x^p|^{\frac{1}{p}}} \max(|x^p|^{\frac{1}{p}} - y, 0). \quad (4.13)$$

### ***b*-subproblem**

$$b^{k+1} = b^k + \nabla_{NL}^p u - d^{k+1}. \quad (4.14)$$

Combining the above formulations, one can define the detailed algorithm for the proposed method as in Algorithm 7.

---

**Algorithm 7** Split-Bregman Algorithm for Poisson denoising

---

**Input:** Noisy image  $u_0$ .

**Output:** Restored Image  $u$ .

- 1: Initialize  $k = 1, u^1 = u_0, u^0 = 0, f^1 = u_0, \varepsilon = 0.0001$ .
  - 2: **while**  $\frac{|u^k - u^{k-1}|}{|u^k|} \geq \varepsilon$  **do**.
  - 3:      $u^{k+1} = \frac{\lambda \frac{u_0}{u^k} - \beta \nabla_{NL}^p \cdot (d - b^k)}{\frac{\lambda}{u^k} I - \beta \Delta_{NL}^p}$
  - 4:      $d^{k+1} = \mathit{shrink}(\nabla_{NL}^p u + b^k, 1/\beta)$
  - 5:      $b^{k+1} = b^k + (\nabla_{NL}^p u - d^{k+1})$
  - 6:      $u^k = u^{k+1}, k \leftarrow k + 1$
  - 7: **end while**
- 

## **4.3 EXPERIMENTAL RESULTS**

For experimental study, three test images (natural images) are selected and they are shown in their original forms in Figure 4.5. These images are synthetically corrupted with the Poisson noise to study the performance in terms of the well known statistical measures. We apply Poisson process to these images with three peak values, 2, 30 and 70, respectively. A further analysis is performed using original Poisson images from CT, confocal and fluorescent imaging applications. The experimental study of these (original) test images are limited to their visual comparison due to non-availability of the ground truth data. Comparative analysis is performed using the recent and relevant Poisson denoising models from the literature along with the proposed one i.e.:

MODEL 1: Fast TV algorithm Wang and He (2017).

MODEL 2: Variance Stabilization Transform(VST) model Azzari and Foi (2016).

MODEL 3: PDE based poisson restoration Srivastava and Srivastava (2013).

MODEL 4: Poisson restoration using non-local PCA Salmon et al. (2014).

MODEL 5: Non-local TV regularization model for Poisson noise. Zhang et al. (2014)

MODEL 6: Poisson Inverse Problems by the Plug-and-Play scheme. Rond et al. (2016)

The proposed scheme is implemented, following the steps given in Algorithm 7. Parameter values used for various methods are given in Table 4.2. In the proposed model,  $\lambda$  controls the diffusion by putting back the lost details. Hence for a low peak noise, value of  $\lambda$  should be slightly higher than that of a high peak noise. Another parameter  $\beta$  controls the smoothing characteristics of the filter, which should be comparatively more for low peak noise than the higher peak one. The value of  $p$  (generally called as smoothness degree) is chosen between 0 and 2 (i.e.,  $0 < p < 2$ ) (because image gets over smoothed beyond the value  $p = 2$ ). All these parameters are set empirically analyzing their results for various values. The statistical analysis performed for the comparative study includes three quality metrics: PSNR, SSIM and MSE (refer Section 1.8 for the details).

Table 4.1 shows the results of statistical analysis for all the test images. PSNR gives the noise removal capability whereas SSIM measures the structure and contrast preserving ability of a model. The error between the restored version and the reference image is evaluated using MSE. It is evident that the proposed model gives better PSNR value while preserving fine details (which results in high SSIM values). Also, the mean squared error is less compared to other techniques.

The Figures 4.6, 4.7 and 4.8 show the results obtained (using various models) for images corrupted with Poisson noise of peak value 70. Whereas Figure 4.9 shows the results of various models in the presence of low peak noise i.e., peak = 2. The proposed model performs better in terms of denoising and edge-preserving as evident from these figures. Since we used  $p$ -norm instead of 2-norm, the algorithm is much more flexible in terms of denoising and sharpening. When  $0 < p < 1$ , the proposed model produces sharper edges, whereas, for the values of  $p$  close to 2, the edges are found to be more smoothed. However, setting  $1 < p < 2$  will help in removing more noise in the presence of low peak noise. Figure 4.13 shows outputs of 1-Dimensional data (150th row of the synthetic image given in Figure 4.5 (c)) for different values of  $p$ . The cropped portion of “Girlface” in Figure 4.5(a) corrupted with Poisson noise (of peak 70) and Gaussian blur (of standard deviation  $\sigma = 1$ ) is tested using different values of  $p$ , and the results are shown in Figure 4.14.

In order to show the effectiveness of the proposed model some images from real-

world applications (such as CT, confocal and fluorescent spectroscopy) were selected and tested. These images are found to be usually corrupted with Poisson noise. The CT image used for testing is obtained from <https://public.cancerimagingarchive.net>. The output results (of various models considered in this paper) for the CT image are shown in Figure 4.10. In Figure 4.11 the results of a real confocal image of zebrafish embryo mitosis (for more details see: <http://cellimagelibrary.org/images/36594>) are shown. Comparative results of fluorescence microscopic image (obtained from the website: [http://cbia.fi.muni.cz/projects/cytopacq-a-simulation-toolbox\\_6.html](http://cbia.fi.muni.cz/projects/cytopacq-a-simulation-toolbox_6.html), for more details, see Svoboda et al. (2016)) are shown in Figure 4.12. The proposed model performs well in all cases as evident from these results. Moreover, the performance of the model in terms of denoising and sharpening, is also evident from all these test results.

#### 4.4 Summary

A detailed analysis of restoration of images corrupted by Poisson noise was performed in this chapter. To this end, a non-local total variational framework with  $L_p$  norm has been proposed to restore the images corrupted by a Poisson process. Image data from some of the important imaging applications such as fluorescence, confocal microscopy, and computed tomography were tested and compared using the proposed framework and the other state-of-the-art Poisson denoising algorithms. As observed from the results, the proposed model is found to perform well in terms of the visual and statistical results. The value of  $p$  can be tuned according to the noise peak value and nature of the desired output data. Model 1 uses the TV norm for the diffusion. this results in over-smoothing and staircase effects. Model 2 uses a VST to stabilize the variance and subsequently performs a BM3D restoration, which results in better smoothing and structure preservation. Since, the restoration is done in the transformed domain, the restored version slightly deviates from the original one. Model 3 uses a PDE in place of TV diffusion in Model 1, which considerably reduces the staircase effect, but edges and fine-details are smoothed-out. Non-local PCA based restoration has been considered in Model 4. This yields a better restoration capability under a low peak noise, but smooths out some important details in case of a high peak noise. The Model 5 uses non-local

scheme with  $L^2$  norm, which causes over-smoothing in case of a low peak noise and thereby results in data loss and blurriness. Restoration in the transformed domain has been employed in Model 6, which uses Anscombe transform to make the noise independent of the data (similar to additive white Gaussian noise), which is yet again inefficient in case of a low peak noise. Whereas, the proposed model uses the non-local  $p$  – norm regularization for the diffusion, which is flexible in terms of smoothing and edge preserving. The values of  $p$  less than one result in sharpening of the data and the values between 1 and 2 performs a diffusion. The use of  $L^p$  norm and NLTV results in efficient restoration in low as well as high peak noise. Also, the proposed model is derived by the noise PDF using the MAP estimator, which gives a close approximation of the desired data (results in low MSE values as evident from Table 4.1). The convergence rate is improved using the split-Bregman scheme, which is crucial while handling huge amount of data in real-time systems. All these features of the proposed scheme make it better than the other schemes.

**Table 4.1** Quality metrics for Poisson noise with peak (2,30,70).

Image name	Metric	Noisy	Model 1	Model 2	Model 3	Model 4	Model 5	Model 6	Proposed
Girlface	PSNR	(20.56, 21.43, 23.75)	(21.25, 28.8, 30.98)	(22.5, 27.69, 30)	(22, 21.41, 24.43)	(22.87, 23.94, 24.82)	(23.03, 29.03, 29.67)	(22.15, 26.45, 28.63)	(23.7, 30.05, 30.66)
	SSIM	(0.06, 0.17, 0.26)	(0.24, 0.51, 0.57)	(0.35, 0.46, 0.56)	(0.23, 0.35, 0.42)	(0.47, 0.52, 0.58)	(0.48, 0.49, 0.55)	(0.42, 0.47, 0.62)	(0.5, 0.51, 0.71)
	MSE	(0.87, 17.25, 39.71)	(0.74, 1.23, 3.99)	(0.24, 1.53, 4.91)	(0.22, 2.4, 8.21)	(0.08, 2.24, 8.41)	(0.07, 1.23, 5.28)	(0.07, 1.63, 6.23)	(0.08, 1.29, 4.41)
Bridge	PSNR	(18.5, 22.50, 23.24)	(19.04, 23.43, 24.86)	(21.2, 23.1, 25.9)	(21.6, 23.4, 26.45)	(21.9, 22.6, 25.05)	(22.45, 24.17, 26.36)	(20.34, 25.69, 27.45)	(21.62, 25, 26.09)
	SSIM	(0.07, 0.45, 0.62)	(0.1, 0.48, 0.55)	(0.26, 0.48, 0.65)	(0.17, 0.46, 0.64)	(0.46, 0.57, 0.64)	(0.52, 0.56, 0.58)	(0.4, 0.41, 0.6)	(0.52, 0.53, 0.67)
	MSE	(0.9, 13.5, 31.11)	(0.8, 4.09, 16.42)	(0.65, 4.39, 15.53)	(0.5, 4.09, 17.86)	(0.48, 4.9, 14.93)	(0.41, 3.51, 13.95)	(0.49, 3.25, 13.27)	(0.46, 3.37, 13.95)
Synthetic	PSNR	(19.08, 22.34, 25.05)	(19.63, 28.05, 31.24)	(20.05, 28, 32.34)	(21.03, 21.33, 24.23)	(20.04, 22.73, 26.01)	(20.36, 29.63, 31)	(20.25, 26.46, 29.77)	(22.45, 30.43, 34.61)
	SSIM	(0.19, 0.39, 0.44)	(0.29, 0.54, 0.57)	(0.43, 0.54, 0.59)	(0.22, 0.49, 0.51)	(0.42, 0.49, 0.51)	(0.4, 0.54, 0.56)	(0.51, 0.61, 0.68)	(0.53, 0.66, 0.78)
	MSE	(1.08, 15.18, 35.15)	(0.88, 1.61, 4.11)	(0.67, 1.56, 3.41)	(0.6, 2.38, 6.65)	(0.18, 2.17, 6.06)	(0.15, 1.2, 4.23)	(0.21, 1.8, 5.2)	(0.1, 0.96, 2.52)

**Table 4.2** Parameter values for different methods for peak (30,70)

Parameter	Model 1	Model 3	Model 4	Model 5	Proposed
$\lambda$	-	-	-	(7, 6)	(5, 5)
$\beta$	(0.5, 0.5)	-	-	(0.7, 0.4)	(0.85, 0.5)
Time step	(0.5, 0.25)	(0.15, 0.15)	-	-	-
Patch size	-	-	(8, 5)	(11, 11)	(21, 21)
(for Non-local TV)	-	-	-	(16, 16)	(9, 9)
Window size	-	-	-	(14, 11)	(8, 5)
(for Non-local TV)	-	-	-	-	-
No. of similar windows	-	-	(14, 8)	(14, 11)	(8, 5)
(For Non-local TV)	-	-	-	-	-

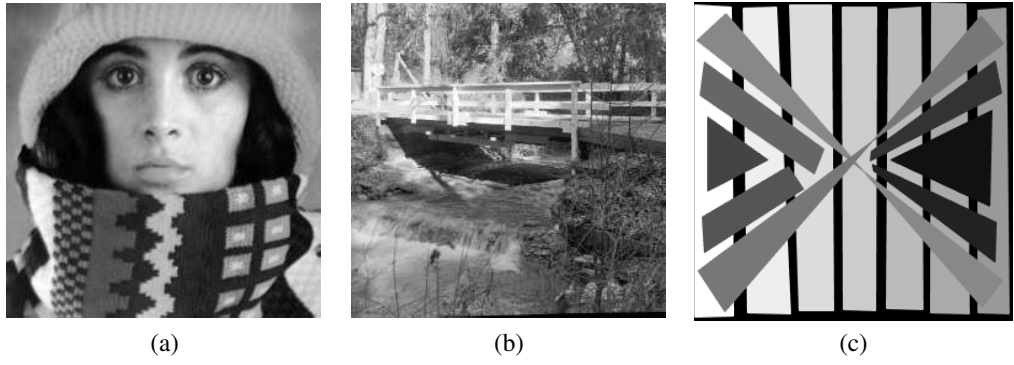


**Figure 4.5** Test images in their original form

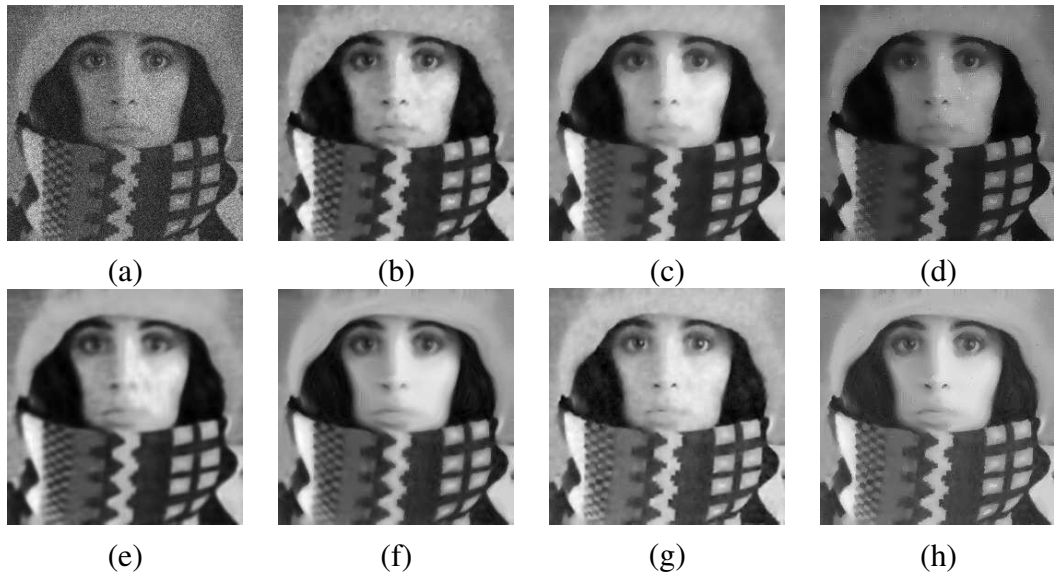


**Figure 4.6** (a) Image “Girlface” corrupted with Poisson noise, peak=70, Restored using (b) Model 1, (c) Model 2, (d) Model 3, (e) Model 4, (f) Model 5, (g) Model 6 and (h) Proposed one with  $p = 0.5$ .

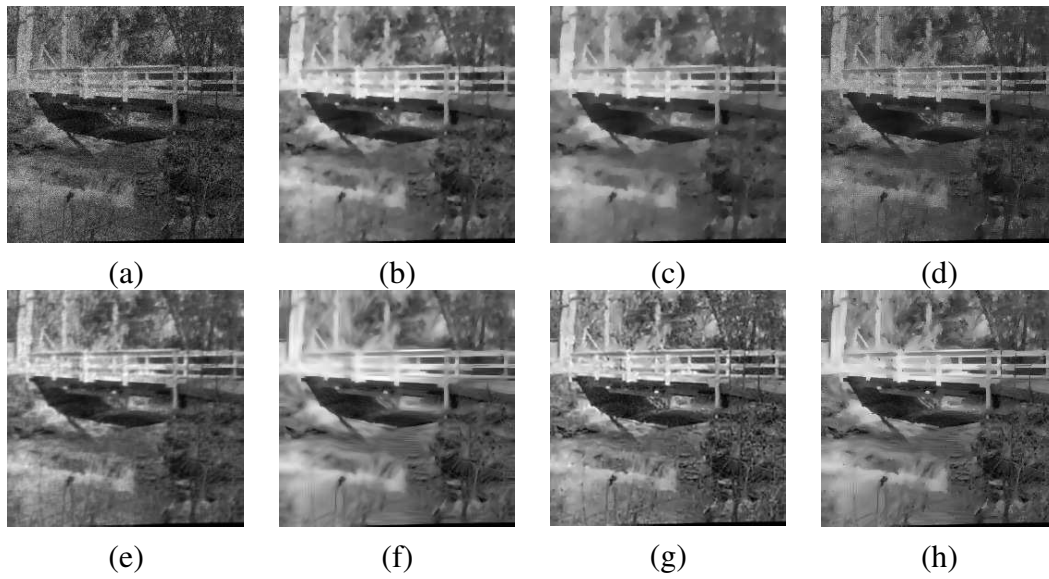


**Figure 4.7** (a) Image “Bridge” corrupted with Poisson noise, peak=70, Restored using (b) Model 1, (c) Model 2, (d) Model 3, (e) Model 4, (f) Model 5, (g) Model 6 and (h) Proposed one with  $p = 0.5$ .

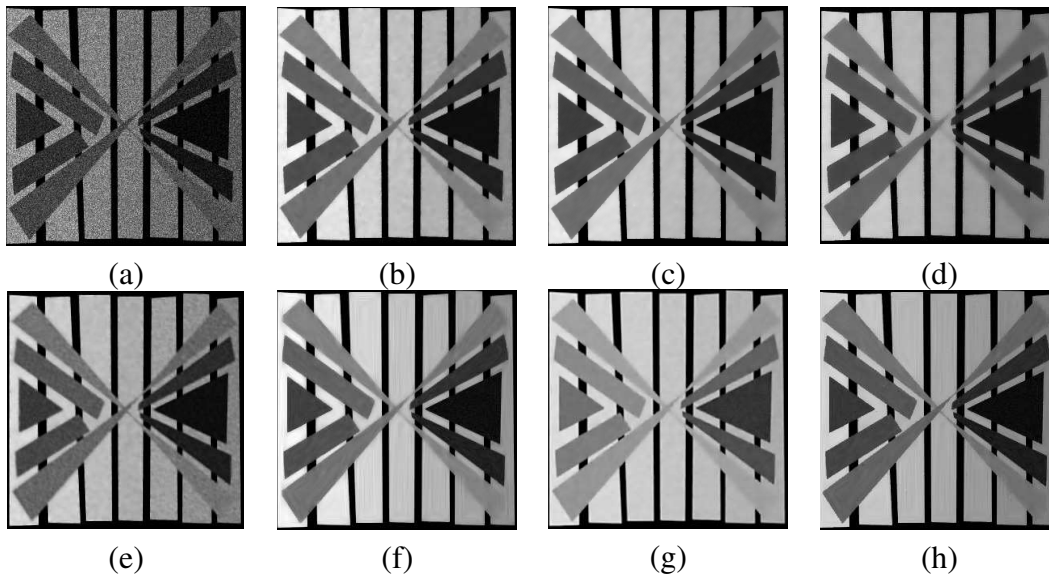


**Figure 4.8** (a) Synthetic image corrupted with Poisson noise, peak=70, Restored using (b) Model 1, (c) Model 2, (d) Model 3, (e) Model 4, (f) Model 5, (g) Model 6 and (h) Proposed one with  $p = 0.5$ .



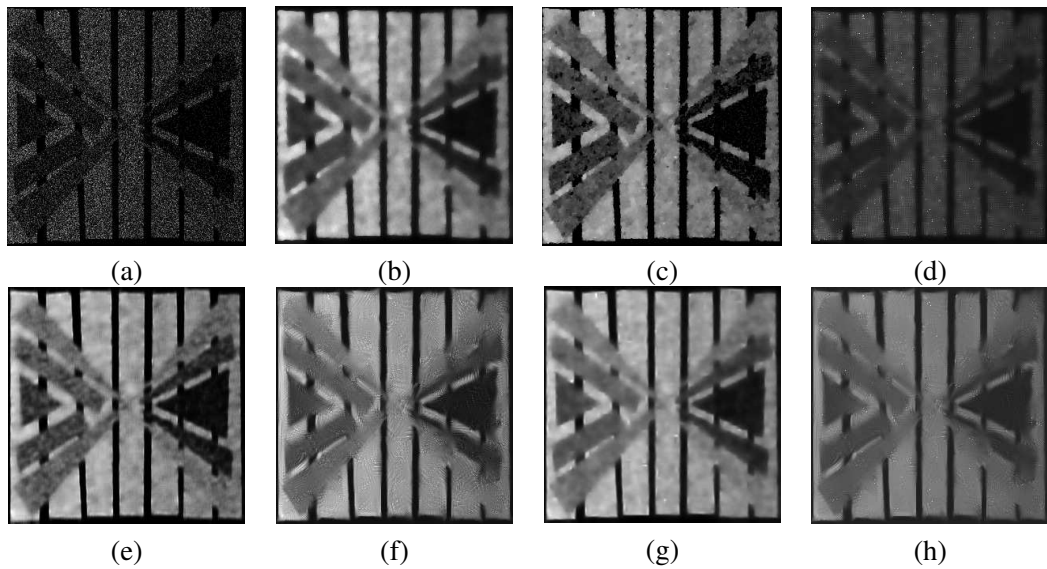


**Figure 4.9** (a) Synthetic image corrupted with Poisson noise of peak=2, Restored using (b) Model 1, (c) Model 2, (d) Model 3, (e) Model 4, (f) Model 5, (g) Model 6 and (h) Proposed one with  $p = 0.5$ .

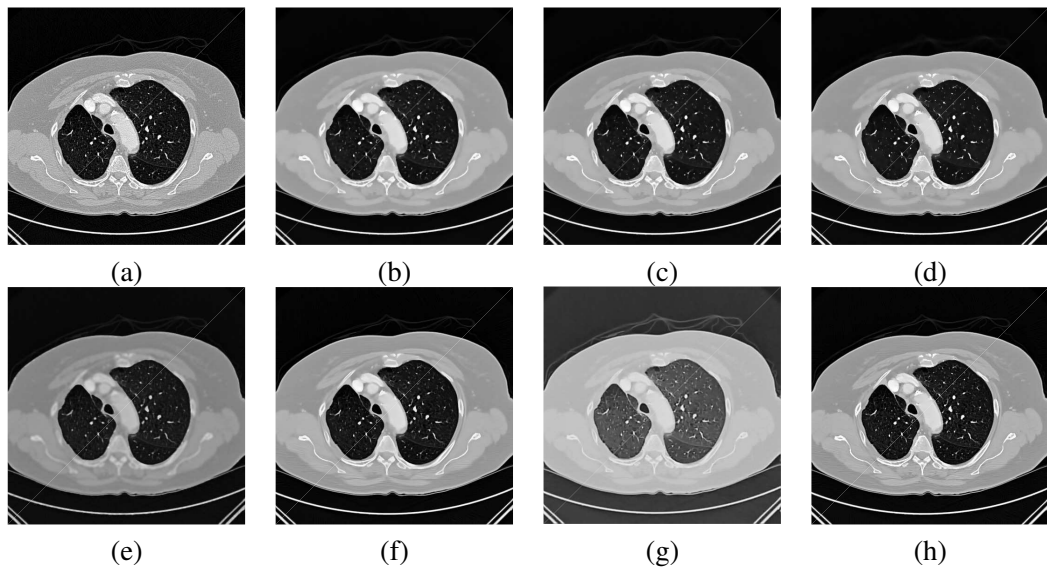


**Figure 4.10** (a) Real CT image corrupted with Poisson noise, Restored using (b) Model 1, (c) Model 2, (d) Model 3, (e) Model 4, (f) Model 5, (g) Model 6 and (h) Proposed one with  $p = 0.5$ .

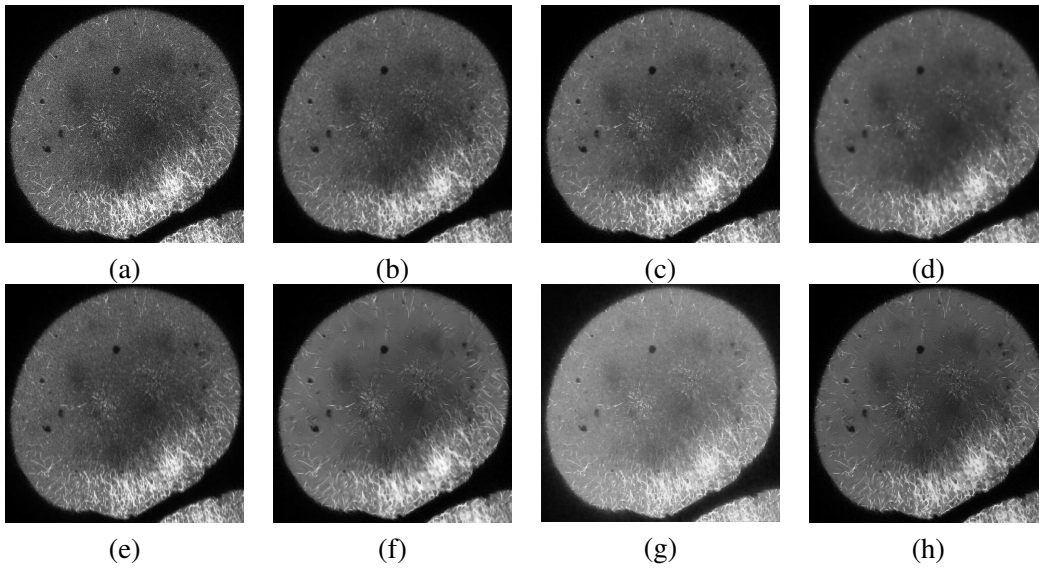


**Figure 4.11** (a) Real confocal image corrupted with Poisson noise, Restored using (b) Model 1, (c) Model 2, (d) Model 3, (e) Model 4, (f) Model 5, (g) Model 6 and (h) Proposed one with  $p = 0.5$ .

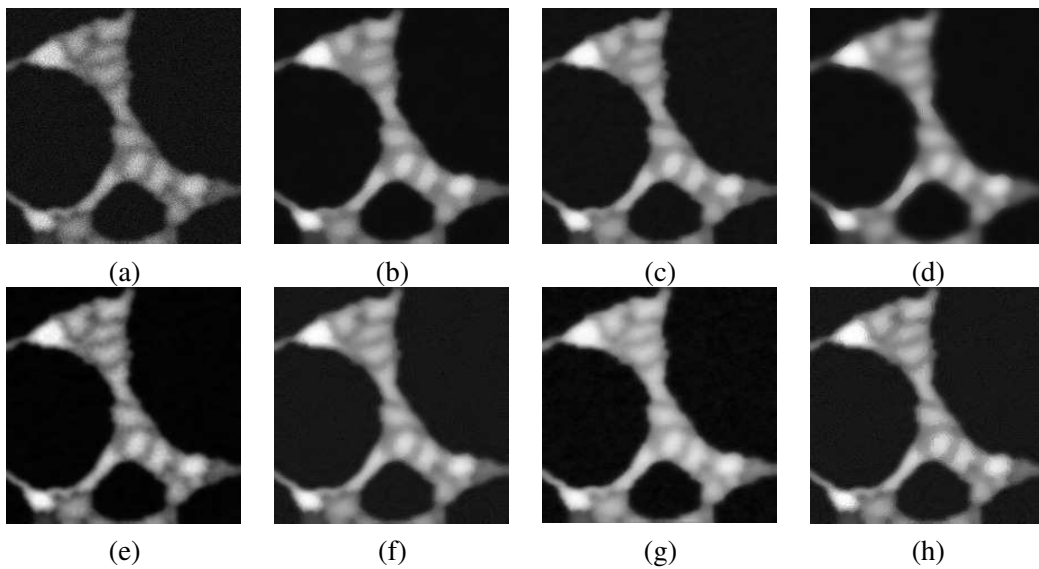


**Figure 4.12** (a) Real fluorescence image corrupted with Poisson noise, Restored using (b) Model 1, (c) Model 2, (d) Model 3, (e) Model 4, (f) Model 5, (g) Model 6 and (h) Proposed one with  $p = 0.5$ .

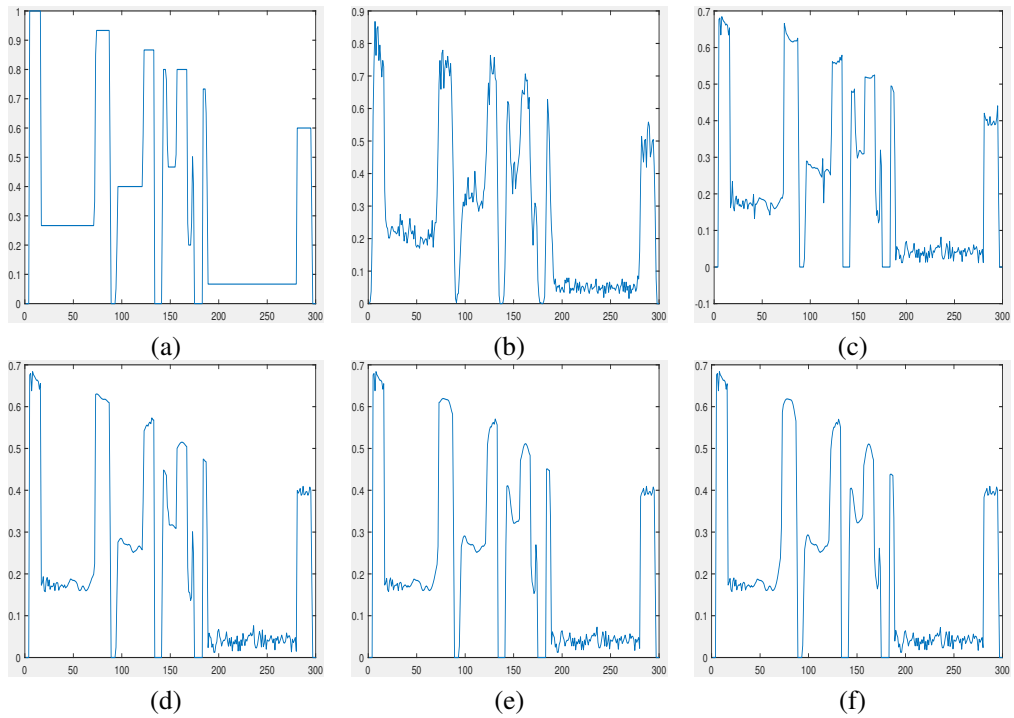


**Figure 4.13** (a) Original 1-D data, (b) Corrupted with Poisson noise of peak 70 and Gaussian blur of  $\sigma=1$ , restored using proposed model with (c)  $p = 0.25$ , (d)  $p = 0.5$ , (e)  $p = 1$  and (f)  $p = 2$ .

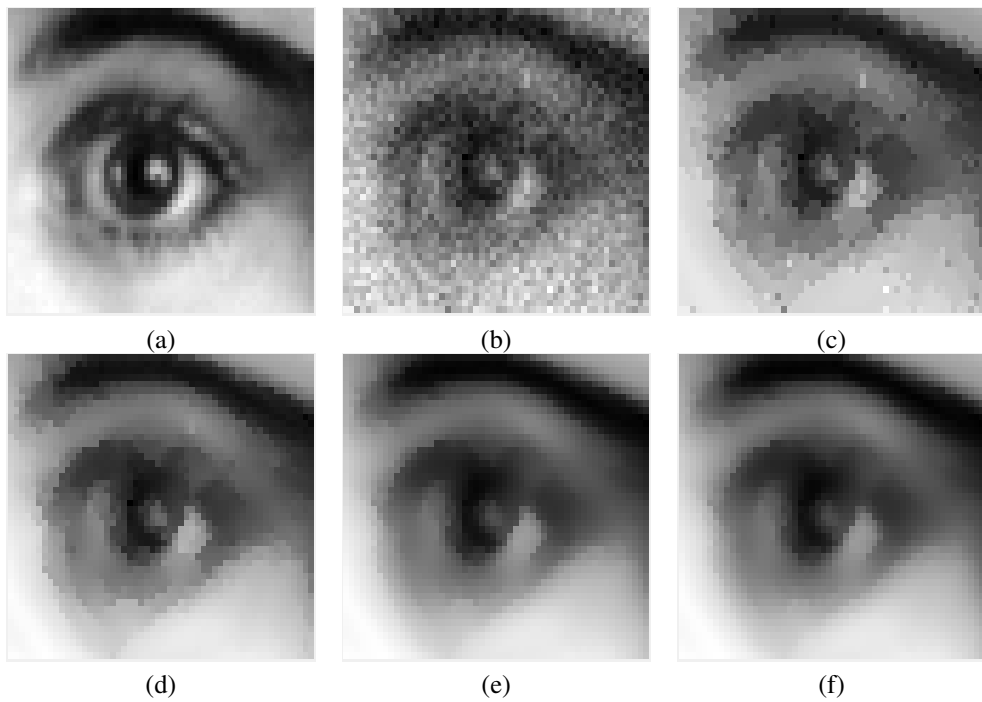


**Figure 4.14** (a) Original cropped portion of “Girlface” image, (b) Corrupted with Poisson noise of peak 70 and Gaussian blur of  $\sigma=1$ , restored using proposed model with (c)  $p = 0.25$ , (d)  $p = 0.5$ , (e)  $p = 1$  and (f)  $p = 2$ .



## Chapter 5

# CONCLUSIONS AND FUTURE SCOPES

### 5.1 CONCLUDING REMARKS

Three variational frameworks have been proposed as a part of the thesis. The first among them is for restoring data-correlated Chi distributed noise commonly found in multiple-coil MR data, the proposed strategy devises the model, solves the same and seeks for the conditions for the existence of a unique solution. The second approach deals with data-correlated multiplicative noise following a Rayleigh distribution. Such degradations are common in ultrasound and SAR imagery. The proposed framework designs a variational approach to accommodate the model and solving the same. Finally, a model to handle Poisson degraded image is being proposed. The model uses an adaptive  $p$  – norm based regularizer to restore the data. All these proposed models thus designed are solved using split-Bregman scheme in-order to improve the convergence rate.

A non-local total bounded variation driven multiple-coil MRI restoration is introduced in Chapter 2. The data-dependent Chi distributed noise present in multiple-coil MR images gets effectively erased by the model in the course of its iteration. The model also works well for single-coil MRI as well by setting the coil count to one. The proposed method is tested on both real and synthetic MR images along with other test images (like natural and synthetic images). The model is compared with the state of the art MRI denoising algorithms both visually and statistically (using well known statistical measures). The proposed strategy is found to perform well in view of the results presented in the work. This model convergences fast due to its reformulation under

split-Bregman iteration scheme. The test results under various parameter adjustments are duly in favor of the robust restoration ability of the proposed model.

In Chapter 3, a thorough study was performed for the restoration of images corrupted by Rayleigh distributed noise and linear blurring artefacts. As a result, three new restoration models were introduced and analyzed in this work. The first model is based on a variance stabilization transform and the other two are based on the maximum a posteriori estimator. The maximum a posteriori estimation based models proposed in this chapter derive convex energy functionals, therefore they eventually converge to unique solutions (in each case separately). A fast numeral approach based on the split-Bregman formulation is employed for solving these models. The proposed methods were compared visually and quantitatively with the state-of-the-art models proposed for Rayleigh distribution in the literature. As observed from the experimental outcomes, the proposed models are found to restore images pretty well compared to the other state-of-the-art models (considered in this work). The maximum a posteriori estimation based models perform better (in terms of preserving the structures present in images) than the variance stabilization models, as the stabilization transform cannot make data completely uncorrelated with the noise. This fact is clearly visible from the tables shown in favor of the statistical measures detailed in the chapter. Furthermore, these models are derived directly from the probability density function of the noise distribution, thus they are more effective in denoising data-correlated noise. Among the proposed maximum a posteriori estimation based models, the model based on non-local total bounded variation performs better than the non-local total variational model as evident from the results. This scenario may be explained with reference to the capability of total bounded variation to restore images pretty well compared to the usual total variation, due to an additional parameter controlled  $L^2$  penalty term. All methods are tested and statistically verified using a large set of images.

A detailed analysis of restoration of images corrupted by Poisson noise was performed in Chapter 4. To this end, a non-local total variational framework with  $L_p$  norm has been proposed to restore the images corrupted by a Poisson process. Image data from some of the important imaging applications such as fluorescence, confocal

microscopy and computed tomography were tested and compared using the proposed framework and the other state-of-the-art Poisson denoising algorithms. The variational energy formulation was designed using the MAP estimate of the noise PDF. A split-Bregman iteration scheme is employed to solve this optimization problem for obtaining a faster converge rate in place of the usual explicit schemes. This study provides a demonstration of the results in terms of both visual and statistical measures. The effectiveness of  $L_p$  norm in a non-local regularization scheme is analyzed in this work. The implementation details maybe provided like software and hardware

## **5.2 FUTURE SCOPE OF THE RESEARCH**

Various restoration models have been highlighted as a part of this thesis. The major focus is laid on variational formulations and their properties. A further theoretical and experimental improvisation is envisaged in futures research endeavors. In terms of theoretical framework, a further study can be conducted that includes properties like convexity, coercivity, regularity, Lipschitz continuity of the gradient of the functional that is being minimized. The behavior of the implemented algorithm depends on such properties. Understanding and implementing them in the construction of algorithm makes the algorithm robust and makes it flexible to work in any circumstance.

Further, to improve the convergence aspects, projection based models are apt candidates for further exploration. An effective projection based model can further catalyze the convergence rate by reducing the computational complexity. Their features and properties are to be studied in depth to analyze their suitability in such variational optimization problems.

Finally, the computational efficiency of the models can further be improved using hardware accelerators (such as parallel processing and graphical processing units.), which is one of the most crucial requirements in most of the real-time imaging applications. Hence, the future work involves employing advancements at the hardware level for the smooth and fast performance of the variational image restoration models.





# Appendix A

This section gives the mathematical derivations, examples, and condition for existence of unique solutions relevant for the proposed schemes. Some sample MATLAB codes used for the implementation are also shown in this section.

## A.1 EXAMPLE FOR AN ILL-POSED PROBLEM

Consider the system (Hansen (2010)),

$$\begin{pmatrix} 1 \\ 2 \end{pmatrix} x = \begin{pmatrix} 1 \\ 2.2 \end{pmatrix}. \quad (\text{A.1})$$

For this problem, there is no solution (there is no  $x$  such that  $x = 1$  and  $2x = 2.2$ ) hence it is an ill-posed problem. To solve the problem given in (A.1), we can reformulate the same as the least squares (or minimization) problem:

$$\min_x \left\| \begin{pmatrix} 1 \\ 2 \end{pmatrix} x - \begin{pmatrix} 1 \\ 2.2 \end{pmatrix} \right\|_2^2 = \min_x ((x-1)^2 + (2x-2.2)^2), \quad (\text{A.2})$$

has a unique and approximated solution,  $x = 1.08$  (where,  $\|\cdot\|$  represents the Euclidean norm).

## A.2 EULER-LAGRANGIAN DERIVATIVE

Let  $y(x)$  be a curve in a two dimensional Euclidean space and  $\eta(x)$  be another curve such that  $\eta(x_1) = \eta(x_2) = 0$ . Let us consider another function

$$Y(x) = y(x) + \varepsilon \eta(x),$$

where  $\varepsilon$  is a constant scalar which scales the curve  $\eta(x)$ . Now,

$$Y'(x) = y'(x) + \varepsilon \eta'(x),$$

where  $y'(x)$  denotes  $\frac{dy}{dx}$ . Similarly

$$\frac{\partial Y'}{\partial \varepsilon} = \eta'(x), \quad (\text{A.3})$$

and

$$\frac{\partial Y}{\partial \varepsilon} = \eta(x). \quad (\text{A.4})$$

Now consider the functional  $J$

$$J(\varepsilon) = \int_{x_1}^{x_2} F(x, Y, Y') dt, \quad (\text{A.5})$$

where  $F$  is a functional that depends on  $x$ ,  $Y$  and  $Y'$ .

To find the minimum of  $J(\varepsilon)$ , we let

$$\left. \frac{\partial J}{\partial \varepsilon} \right|_{\varepsilon=0} = 0.$$

When  $\varepsilon = 0$ , we get  $Y'(x) = y(x)$  which is exactly the curve  $y(x)$ . Now we have,

$$\frac{\partial}{\partial \varepsilon} \int_{x_1}^{x_2} F(x, Y, Y') dx = 0. \quad (\text{A.6})$$

Now applying chain rule for integration, we get

$$\int_{x_1}^{x_2} \left[ \frac{\partial f}{\partial Y} \frac{\partial Y}{\partial \varepsilon} + \frac{\partial f}{\partial Y'} \frac{\partial Y'}{\partial \varepsilon} \right] dx = 0. \quad (\text{A.7})$$

By the substitution of A.3 and A.4 in A.7 we get,

$$\int_{x_1}^{x_2} \left[ \frac{\partial f}{\partial y} \eta(x) + \frac{\partial f}{\partial y'} \eta'(x) \right] dx = 0. \quad (\text{A.8})$$

Next, we distribute the integration over the equation and apply integration by parts rule to the second term of the equation. And we apply the limit  $\eta(x_1) = \eta(x_2) = 0$ , we get the equation as

$$\int_{x_1}^{x_2} \left[ \frac{\partial f}{\partial y'} dx + \int_{x_1}^{x_2} \frac{d}{dx} \frac{\partial f}{\partial y'} dx \right] \eta(x) = 0. \quad (\text{A.9})$$

Since  $\eta(x)$  cannot be zero, the only possibility is

$$\frac{\partial f}{\partial y} + \frac{d}{dx} \frac{\partial f}{\partial y'} = 0. \quad (\text{A.10})$$

Above equation is called as the Euler-Lagrangian (E-L) equation (see Gelfand and Fomin (1963) for more details).

### **A.3 CONDITION FOR EXISTENCE OF A UNIQUE SOLUTION FOR *Chi* DISTRIBUTED RESTORATION MODEL**

Here we analyze the uniqueness property of the solution of (2.9) since the convexity of the TV is known the regularization term need not require any further explanation. Consider the reactive or fidelity term and define it as  $\Phi(u)$  (the Gaussian blurring kernel  $K$  is taken as identity as the presence of this linear operator does not make any effect on

the analysis)

$$\Phi(u) = (L-1) \log(u) + (u^2)/(2\sigma^2) - \log I_{L-1} \left( \frac{u_0 u}{\sigma^2} \right), \quad (\text{A.11})$$

let us take the first variation of  $\Phi(u)$  with respect to  $u$ , we get

$$\Phi'(u) = (L-1)/u + \frac{1}{\sigma^2} \left[ u - \frac{I'_{L-1} \left( \frac{u_0 u}{\sigma^2} \right)}{I_{L-1} \left( \frac{u_0 u}{\sigma^2} \right)} u_0 \right], \quad (\text{A.12})$$

where  $I'(\cdot)$  is the first derivative of the Bessel function  $I(\cdot)$ . Now let us take the second derivative of the function  $\Phi(u)$

$$\Phi''(u) = \frac{1-L}{u^2} + \frac{1}{\sigma^2} \left[ 1 - \frac{u_0^2}{\sigma^2} \left[ \frac{I''_{L-1} \left( \frac{u_0 u}{\sigma^2} \right)}{I_{L-1} \left( \frac{u_0 u}{\sigma^2} \right)} - \left[ \frac{I'_{L-1} \left( \frac{u_0 u}{\sigma^2} \right)}{I_{L-1} \left( \frac{u_0 u}{\sigma^2} \right)} \right]^2 \right] \right], \quad (\text{A.13})$$

where

$$I_L(u) = \sum_{k=0}^{\infty} \frac{(-1)^k \left( \frac{u}{2} \right)^{2L+1}}{(k+L)!k!},$$

$$I'_L(u) = \frac{1}{2} [I_{L-1}(u) + I_{L+1}(u)],$$

and

$$I''_L(u) = \frac{1}{4} [I_{L-2}(u) + 2I_L(u) + I_{L+2}(u)].$$

Now the condition for convexity of the functional  $\Phi(u)$  is that  $\Phi''(u) > 0$ , therefore,

$$\frac{u_0^2}{\sigma^2} \left[ \frac{I''_{L-1} \left( \frac{u_0 u}{\sigma^2} \right)}{I_{L-1} \left( \frac{u_0 u}{\sigma^2} \right)} - \left[ \frac{I'_{L-1} \left( \frac{u_0 u}{\sigma^2} \right)}{I_{L-1} \left( \frac{u_0 u}{\sigma^2} \right)} \right]^2 \right] < 1 \quad (\text{A.14})$$

$$\left[ \frac{I''_{L-1} \left( \frac{u_0 u}{\sigma^2} \right)}{I_{L-1} \left( \frac{u_0 u}{\sigma^2} \right)} - \left[ \frac{I'_{L-1} \left( \frac{u_0 u}{\sigma^2} \right)}{I_{L-1} \left( \frac{u_0 u}{\sigma^2} \right)} \right]^2 \right] < \frac{\sigma^2}{u^2},$$

it implies

$$\frac{I''_{L-1} \left( \frac{u_0 u}{\sigma^2} \right)}{I_{L-1} \left( \frac{u_0 u}{\sigma^2} \right)} < \left( \frac{I'_{L-1} \left( \frac{u_0 u}{\sigma^2} \right)}{I_{L-1} \left( \frac{u_0 u}{\sigma^2} \right)} \right)^2 + \frac{\sigma^2}{u^2},$$

Substituting the expressions of  $I'(\cdot)$  and  $I''(u)$  in the above expression we get

$$\frac{\frac{1}{4} \left[ I_{L-3} \left( \frac{u_0 u}{\sigma^2} \right) + 2I_{L-1} \left( \frac{u_0 u}{\sigma^2} \right) + I_{L+1} \left( \frac{u_0 u}{\sigma^2} \right) \right]}{I_{L-1} \left( \frac{u_0 u}{\sigma^2} \right)} < \left( \frac{\frac{1}{2} \left[ I_{L-2} \left( \frac{u_0 u}{\sigma^2} \right) + I_L \left( \frac{u_0 u}{\sigma^2} \right) \right]}{I_{L-1} \left( \frac{u_0 u}{\sigma^2} \right)} \right)^2 + \frac{\sigma^2}{u^2} \quad (\text{A.15})$$

## A.4 UNIQUENESS OF THE SOLUTIONS OF RAYLEIGH MODELS

Here the condition for the existence of a unique solution for the proposed functional in (3.15) is derived. Let us recall the functional,

$$\min_u \left\{ \int_{\Omega} \left( \frac{u_0^2}{2(u)^2} + 2 \log(u) \right) dx dy + \int_{\Omega} \frac{\lambda}{2} J_{NLTV}(u) dx dy \right\}. \quad (\text{A.16})$$

The first term in the functional (A.16) ensures the fidelity of the solution. This term is conditionally convex i.e. its second derivative is conditionally non-negative. The first derivative of the fidelity term is

$$K^* \left( -u_0^2 / (Ku)^3 + 2 / (Ku) \right) \quad (\text{A.17})$$

and the second derivative is

$$K^* \left( K^* \left( 3u_0^2 / (Ku)^4 - 2 / (Ku)^2 \right) \right). \quad (\text{A.18})$$

Therefore the fidelity term is non-negative only if  $u_0^2 > (2/3)(Ku)^2$ . However, it is practically not feasible to make such assumptions, therefore we perform a variable substitution to make the problem un-conditionally convex. Let us consider  $Kz = \log(Ku)$  or  $Ku = e^{Kz}$ . Now substituting this in the main functional gives the modified functional

$$\min_u \left\{ \int_{\Omega} \left( \frac{u_0^2}{2e^{2z}} + 2z \right) dx dy + \lambda \int_{\Omega} \phi(e^z) dx dy \right\}. \quad (\text{A.19})$$

and for deblurring case, the modified functional will be,

$$\min_u \left\{ \int_{\Omega} \left( \frac{u_0^2}{2e^{2Kz}} + 2Kz \right) dx dy + \lambda \int_{\Omega} \phi(e^{Kz}) dx dy \right\}. \quad (\text{A.20})$$

The second derivative of the new fidelity term is  $\frac{2u_0^2}{e^{2z}}$ , since  $u \geq 0$  ( $z = \log u$  or  $e^z = u$ ) and  $u_0 \geq 0$  (since both  $u$  and  $u_0$  represent the image pixels which are generally positive) the fidelity term is invariably convex. Now the second term or the regularization term is chosen as convex i.e.  $\phi(u) = \|\nabla_{NL}u\|^p$  and this term is convex for all values of  $p \geq 1$ . Therefore, the energy functional is convex and a unique solution is guaranteed, subsequently, the iterative procedure converges in finite amount of time.

## Appendix B

This section contains the derivations of MAP estimators for all the discussed models in this thesis. The derivations are provided to ensure the completeness of the thesis. Further details can be found in Afonso and Sanches (2015) and Le et al. (2007), respectively for Rayleigh and Poisson distributions.

### B.1 MAP ESTIMATOR FOR THE NON-CENTRAL *Chi* DISTRIBUTION

The posterior probability function of a *Chi* distribution is given in terms of Bayesian conditional probability as in Fernandez and Vega (2013),

$$P(u_0|u, \sigma, L) = \frac{u^{L-1}}{\sigma^2} u_0^L e^{\left(\frac{-(u_0^2+u^2)}{2\sigma^2}\right)} I_{L-1}\left(\frac{u_0 u}{\sigma^2}\right) H(u_0). \quad (\text{B.1})$$

Let us recall the Bayes rule,

$$P(U|F) = \frac{P(F|U)P(U)}{P(F)}, \quad (\text{B.2})$$

where  $F$  and  $U$  are events,  $P(F) \neq 0$ ,  $P(F|U)$  a likelihood estimate of the distribution,  $P(U|F)$  is a posterior estimate and  $P(F)$  and  $P(U)$  are probabilities of  $U$  and  $F$  respectively. In our case  $F = u_0$  and  $U = u$  (will be the observed and the original images respectively). So we need to maximize  $P(u|u_0)$ . This leads to maximization of log-likelihood:

$$\log(P(u|u_0)) = \log(P(u_0|u)) + \log(P(u)) - \log(P(u_0)). \quad (\text{B.3})$$

Since  $P(u_0)$  is constant and does not affect the optimization process, let us omit this term without losing generality of the expression, therefore we have,

$$P(u|u_0) \triangleq P(u_0|u, \sigma, L) = \frac{u^{L-1}}{\sigma^2} u_0^L e^{\left(\frac{-(u_0^2+u^2)}{2\sigma^2}\right)} I_{L-1}\left(\frac{u_0 u}{\sigma^2}\right) H(u_0) P(u). \quad (\text{B.4})$$

Now maximizing this conditional probability gives,

$$\max_u \{P(u|u_0)\} = \max_u \left\{ \frac{u^{L-1}}{\sigma^2} u_0^L e^{\left(\frac{-(u_0^2+u^2)}{2\sigma^2}\right)} I_{L-1} \left(\frac{u_0 u}{\sigma^2}\right) H(u_0) P(u) \right\}, \quad (\text{B.5})$$

since the image is pixellated (represented in terms of discrete pixel values) the above expression gets modified as:

$$\max_u \{P(u(x)|u_0(x))\} = \max_u \left\{ \prod_x \frac{u(x)^{L-1}}{\sigma^2} u_0(x)^L e^{\left(\frac{-(u_0(x)^2+u(x)^2)}{2\sigma^2}\right)} I_{L-1} \left(\frac{u_0(x)u(x)}{\sigma^2}\right) H(u_0(x)) \prod_x P(u(x)) \right\}, \quad (\text{B.6})$$

modifying above equation according to Equation B.3 gives,

$$\max_u \{\log P(u(x)|u_0(x))\} = \max_u \left\{ \log \prod_x \frac{u(x)^{L-1}}{\sigma^2} u_0(x)^L e^{\left(\frac{-(u_0(x)^2+u(x)^2)}{2\sigma^2}\right)} I_{L-1} \left(\frac{u_0(x)u(x)}{\sigma^2}\right) H(u_0(x)) + \log \prod_x P(u(x)) \right\}, \quad (\text{B.7})$$

since the multiplication gets transformed to addition in the log domain, let us replace the product symbols with summation symbols i.e.,

$$\max_u \{\log P(u(x)|u_0(x))\} = \max_u \left\{ \sum_x \log \frac{u(x)^{1-L}}{\sigma^2} u_0(x)^L e^{\left(\frac{-(u_0(x)^2+u(x)^2)}{2\sigma^2}\right)} I_{L-1} \left(\frac{u_0(x)u(x)}{\sigma^2}\right) H(u_0(x)) + \sum_i \log P(u(x)) \right\}, \quad (\text{B.8})$$

since maximizing the log-likelihood is equivalent to minimizing the  $-\log$  likelihood, we have

$$\min_u \{-\log P(u(x)|u_0(x))\} = \min_u \left\{ \sum_x -\log \frac{u(x)^{1-L}}{\sigma^2} u_0(x)^L e^{\left(\frac{-(u_0(x)^2+u(x)^2)}{2\sigma^2}\right)} I_{L-1} \left(\frac{u_0(x)u(x)}{\sigma^2}\right) H(u_0(x)) + \sum_i -\log P(u(x)) \right\}, \quad (\text{B.9})$$

which implies

$$\begin{aligned} \min_u \{-\log P(u(x)|u_0(x))\} = \min_u \left\{ \sum_x -(1-L) \log(u(x)) + \log(\sigma^2) - L \log u_0(x) \right. \\ \left. - (-(u_0(x)^2 + u(x)^2)/(2\sigma^2)) - \log \left( I_{L-1} \left( \frac{u_0(x)u(x)}{\sigma^2} \right) \right) \right. \\ \left. - \log H(u_0(x)) - \sum_x \log(P(u(x))) \right\}. \end{aligned} \quad (\text{B.10})$$

Now discarding the constant terms as they do not contribute towards the optimization procedure, we have

$$\min_u \{-\log P(u(x)|u_0(x))\} = \min_u \left\{ \sum_x (L-1) \log(u(x)) + \frac{u(x)^2}{2\sigma^2} - \log \left( I_{L-1} \left( \frac{u_0(x)u(x)}{\sigma^2} \right) \right) - \sum_x \log(P(u(x))) \right\}, \quad (\text{B.11})$$

further, without losing the generality lets drop the index terms and the sum symbol in the above expression, i.e.

$$\min_u \{-\log P(u|u_0)\} = \min_u \left\{ (L-1) \log(u) + \frac{u^2}{2\sigma^2} - \log \left( I_{L-1} \left( \frac{u_0 u}{\sigma^2} \right) \right) - \log(e^{-\gamma J(u)}) \right\},$$

where  $P(u) \triangleq e^{\gamma J(u)}$  and  $J(u)$  (already defined in (1.25)) is a function of prior probability ( using non-local TV prior in place of  $J(\cdot)$ ) and  $\gamma$  is a scalar regularization parameter.

With this assumption we have

$$\min_u \{-\log P(u|u_0)\} = \min_u \left\{ (L-1) \log(u) + \frac{u^2}{2\sigma^2} - \log \left( I_{L-1} \left( \frac{u_0 u}{\sigma^2} \right) \right) + \gamma J(u) \right\}. \quad (\text{B.12})$$

## B.2 MAP ESTIMATE FOR THE RAYLEIGH DISTRIBUTION

Considering the Rayleigh distribution with PDF  $P(x; \sigma) \triangleq \frac{x}{\sigma^2} e^{-\frac{x^2}{2\sigma^2}}$ , we need to maximize the probability of the random variable  $u$  (the original image pixels) given the observed noisy image  $u_0$ . The conditional probability  $P(u_0|u)$  is defined as

$$P(u_0|u) = p_u(u_0) = \frac{u_0}{u^2} e^{-\frac{u_0^2}{2u^2}}. \quad (\text{B.13})$$

We obtained  $P(u_0|u)$  from the definition of the PDF of the Rayleigh distribution by replacing the variables appropriately. Now the Bayesian formulation takes the form

$$\max_u P(u|u_0) = \max_u P(u_0|u)P(u). \quad (\text{B.14})$$

Here  $P(u_0|u)$  denotes the conditional probability (likelihood estimate of the distribution),  $P(u|u_0)$  is a posteriori probability and  $P(u)$  is the prior probability. Considering the image ( $u$  and  $u_0$ ) as a set of independent pixels at  $x_i$  (the joint probability becomes the product of marginal probabilities of each random variable  $u(x_i)$ ), we can modify the above expression as:

$$\max_u P(u(x_i)|u_0(x_i)) = \left\{ \max_u \prod_{i=0}^N (P(u(x_i)|u_0(x_i))P(u(x_x))) \right\}, \quad (\text{B.15})$$

where  $N$  denotes the total number of pixels in the image. Substituting the expression for  $P(\cdot)$  in the above equation and omitting the LHS of the equation for the time being, we have

$$\max_u \left\{ \prod_{i=0}^N \left( \frac{u_0(x_i)}{u(x_i)^2} e^{-\frac{u_0(x_i)^2}{2u(x_i)^2}} P(u(x_i)) \right) \right\}. \quad (\text{B.16})$$

In order to simplify the maximization problem, we consider its analogous log likelihood maximization problem i.e

$$\max_u \left\{ \log \left( \prod_{i=0}^N \frac{u_0(x_i)}{u(x_i)^2} e^{-\frac{u_0(x_i)^2}{2u(x_i)^2}} \right) + \sum_{i=0}^N \log(P(u(x_i))) \right\}. \quad (\text{B.17})$$

(Since  $u_0$  is a constant it does not affect the minimization process, therefore,  $\log(u_0)$  is omitted from further steps.) The above maximization problem can be designed as a minimization problem by considering the  $-\log$  likelihood of the function i.e.

$$\min_u \left\{ \sum_{i=0}^N 2 \log u(x_i) + \frac{u_0(x_i)^2}{2u(x_i)^2} - \sum_{i=0}^N \log(P(u(x_i))) \right\}. \quad (\text{B.18})$$

Without loss of generality let us drop the indices for the images, therefore we have

$$\min_u \left\{ 2 \log u + \frac{u_0^2}{2u^2} - \log(P(u)) \right\}. \quad (\text{B.19})$$

Assuming Gibbs prior  $P(u) = e^{(-\frac{\lambda}{2}J(u))}$ , the above equation becomes

$$\min_u \left\{ 2 \log u + \frac{u_0^2}{2u^2} + \frac{\lambda}{2} J(u) \right\}. \quad (\text{B.20})$$

Here  $J(\cdot)$  denotes the regularization functional and  $\lambda > 0$  the regularization parameter, which are already defined earlier.

### B.3 MAP ESTIMATOR FOR POISSON DISTRIBUTION

The Probability Density Function(PDF) of Poisson distribution is given by,

$$P(z; \lambda) = \frac{e^{-\lambda} \lambda^z}{z!}, \quad (\text{B.21})$$

where  $\lambda$  is both mean and standard deviation for a sample  $z$ . Our goal is to maximize the probability of the random variable  $u$  (the original image) given the observed noisy image  $u_0$ .

$$P(u_0|u) = P_u(u_0) = \frac{e^{-u} u^{u_0}}{u_0!}, \quad (\text{B.22})$$

we got  $P_u(u_0)$  (B.21), now the Bayesian formulation takes the form as in (B.14).

Considering the image ( $u$  and  $u_0$ ) as a set of independent pixels at  $x_i$  (the joint probability becomes the product of marginal probabilities of each random variable  $u(x_i)$ ), we can modify the above expression using a log maximization procedure as: (Since  $u_0$



is a constant it does not affect the minimization process, therefore,  $\log(u_0)$  is omitted from further steps.) Following similar steps as in the previous section and let us modify the above expression using a log maximization procedure as

$$\max_u \left\{ \sum_{i=0}^N -u(x_i) + u_0(x_i) \log u(x_i) + \sum_{i=0}^N \log(P(u(x_i))) \right\}. \quad (\text{B.23})$$

The above maximization problem can be designed as a minimization problem by considering the -log likelihood of the function i.e.

$$\min_u \left\{ \sum_{i=0}^N u(x_i) - u_0(x_i) \log u(x_i) - \sum_{i=0}^N \log(P(u(x_i))) \right\}. \quad (\text{B.24})$$

Generally, we can write the above equation as follows

$$\min_u \left\{ u - u_0 \log u - \log(P(u)) \right\}. \quad (\text{B.25})$$

Assuming Gibbs prior  $P(u) = e^{(-\frac{\lambda}{2}J(u))}$ , the above equation becomes

$$\min_u \left\{ u - u_0 \log u + \frac{\lambda}{2}J(u) \right\}. \quad (\text{B.26})$$

The energy formulation for the above equation is

$$\min_u \left\{ \int_{\Omega} (u - u_0 \log u) dx dy + \int_{\Omega} \frac{\lambda}{2} J(u) dx dy \right\}. \quad (\text{B.27})$$

Assuming  $J(u)$  as  $J_w(u, p)$  as defined in (4.2), we can rewrite the above expression as

$$\min_u \left\{ \int_{\Omega} (u - u_0 \log u) dx dy + \int_{\Omega} \frac{\lambda}{2} J_w(u, p) dx dy \right\}. \quad (\text{B.28})$$

Let us define  $H(u) = u - u_0 \log(u)$ . The steepest descent equation for (B.28) is:

$$u_{n+1} = u_n + \Delta t \left( -\lambda \sum_{x \sim y} w_{xy}^{\frac{p}{2}} (|u(y) - u(x)| + \epsilon)^{p-2} (u(y) - u(x)) + H'(u) \right), \quad (\text{B.29})$$

where  $H'(u) = \frac{u-u_0}{u}$ .



## Appendix C

In this section, a sample MATLAB code used for the implementation of NLTV and split Bregman iterative scheme for additive Gaussian noise is shown. Codes for non-local gradient, non-local divergence and non-local weights are implemented according to Zosso et al. (2013).

### C.1 SAMPLE CODE FOR THE NLTV FILTER USING SPLIT BREGMAN ITERATIVE SCHEME

```
1 function split_breg_Nonlocal
2 % Read image
3 img=imread('barbara.png');
4
5 [n,m]=size(img);
6 N=n*m;
7 img=double(img);
8 figure(1), imshow(img,[]),title('original image');
9 img=img/max(img(:));
10
11 % Add Gaussian noise to the original image
12 nv=15/255;
13 noise=randn(size(img))*nv;
14 img=double(img)+noise;
15
16 figure(2), imshow(img,[]),title('Noisy image');
17 u=img(:); f=img(:);
18 % Set variuos parameters
19 ws=5;ps=3;ms=10;binary=false;h=15;sigma2=3.0;weight_thres=0;
20 W=weights_nonlocal(img,ws,ps,ms,binary,sigma2,h,weight_thres);
21
22 b=sparse(N,N);
23 v=sparse(N,N);
24 beta=.05; lam=0.4;
25 iter=0;
26 while iter<3
27     u=(lam*f+beta*W*u-beta*nonlocal_divergence(W,v-b) ) ./ ...
28         (lam + beta*sum(W,2));
29     del_u=nonlocal_gradient(W,u);
30     v=shrink2(del_u+b, beta);
31     b=b+del_u-v;
32     iter=iter+1;
33 end
34 x=reshape(u,n,m);
35 figure, imshow(x,[]);
```

```

35 end
36
37
38 function x=shrink2(del_ub,beta)
39 st=sign(del_ub);
40 ft=abs(del_ub);
41 ft(ft>0)=ft(ft>0)-beta;
42 ft(ft<0)=0;
43 x=ft.*st;
44 end
45
46
47 function W = ...
    weights_nonlocal(f,ws,ps,ms,binary,sigma,h,weight_thres)
48 % Helper function to construct non-local weight matrix between ...
    image pixels
49 % as introduced by Buades, Coll and Morel.
50
51 if (margin==1)
52     binary = false;
53     sigma = 3.0;
54     ws = 10;
55     ps = 5;
56     ms = 8;
57 end
58
59 [m, n] = size(f);
60 r = m*n;
61 G = fspecial('gaussian', [40, 40], sigma);
62
63 % Computing distance
64 dist = zeros((2*ws+1)*(2*ws+1), r);
65
66 padu = padarray(f, [ws ws], 'symmetric', 'both');
67
68 for i = -ws:ws
69     for j = -ws:ws
70         shiftpadu = padarray(f, [ws-i ws-j], 'symmetric', 'pre');
71         shiftpadu = padarray(shiftpadu, [ws+i ...
            ws+j], 'symmetric', 'post');
72
73         tempu = (padu-shiftpadu);
74         tempu = tempu(1+ws:m+ws, 1+ws:n+ws); % tempu(r,c) = ...
            f(r,c) - f(r+i,c+j);
75
76         padtempu = padarray(tempu, [ps,ps], 'symmetric', 'both');
77
78         uu = conv2(padtempu.^2, G, 'same');
79         uu = uu(1+ps:m+ps, 1+ps:n+ps);
80
81         k=(j+ws)*(2*ws+1)+i+ws+1;
82         dist(k, :) = reshape(uu, 1, []);
83     end
84 end
85 % Computing the weight
86 W = sparse(r,r);
87
88 idx = (0:r-1)';
89 idx = idx*(2*ws+1)^2;
90
91 dist(dist==0) = 1e+5; % Assign a large value -> don't count ...
    that pixel itself
92 for i = 1 : ms
93     [y, minindex] = min(dist); % choose the ms smallest distance
94
95     % position in the vector image f
96     ind1 = [1:r]';
97     minindex = minindex';

```

```

98     ind2 = floor((minindex-1)/(2*ws+1))*(m-2*ws-1) + minindex ...
          +ind1 -ws-1-ws*m;
99
100    tmpindex = find(ind2>0 &ind2≤r);
101
102    if (binary)
103        W = W + sparse(ind1(tmpindex), ind2(tmpindex), 1, r, r);
104    else
105        values = max(exp(-y(tmpindex)/h^2),weight_thres);
106        W = W + sparse(ind1(tmpindex),ind2(tmpindex),values,r,r);
107    end
108    idx2 = idx + minindex; % position in the matrix dist
109    dist(idx2) = inf; % assign inf so that we can come to the ...
          next smallest distance
110 end
111
112 end
113
114
115 function grad=nonlocal_gradient(W,I)
116 N = length(I(:));
117 [row,col,~] = find(W);
118 z = sparse(row,col, I(col)-I(row),N,N);
119 % fgrad = f(z,tau);
120 grad = z.*sqrt(W);
121 end
122
123
124 function div = nonlocal_divergence( W, v )
125 % Helper function that computes the non-local divergence of ...
          vector v on
126 % graph weights W.
127
128 N = size( W, 1 );
129 in = sqrt(W).*v;
130 in = in - in';
131 div = in*ones(N,1);
132 end

```



## Bibliography

- Abbott, J. G. and Thurstone, F. L. (1979). Acoustic speckle: Theory and experimental analysis. *Ultrasonic Imaging*, 1(4), 303–324.
- Afonso, M. and Sanches, J. M. (2015). Image reconstruction under multiplicative speckle noise using total variation. *Neurocomputing*, 150(1), 200–213.
- Aja-Fernandez, Brionb, V., and Tristan-Vegaa, A. (2013). Effective noise estimation and filtering from correlated multiple-coil MR data. *Magnetic Resonance Imaging*, 31(2), 272–285.
- Aja-Fernandez, S., Alberola-Lopez, C., and Westin, C. (2008). Noise and signal estimation in magnitude MRI and Rician distributed images: A LMMSE approach. *IEEE Trans Image Process*, 17(8), 1383–1398.
- Alliney, S. (1992). Digital filters as absolute norm regularizers. *IEEE Transactions on Signal Processing*, 40(6), 1548–1562.
- Aubert, G. and Aujol, J. (2008). A variational approach to removing multiplicative noise. *SIAM Journal on Applied Mathematics*, 68(4), 925–946.
- Awate, S. and Whitaker, R. (2005). Nonparametric neighborhood statistics for MRI denoising. In *Proc IPMI*, 677–88.
- Azzari, L. and Foi, A. (2014). A new nonlocal total variation regularization algorithm for image denoising. *Mathematics and Computers in Simulation*, 97(1), 224–233.
- Azzari, L. and Foi, A. (2016). Variance stabilization for noisy+estimate combination in iterative poisson denoising. *IEEE Signal Processing Letters*, 23(8), 1086–1090.

- Benvenuto, F., Camera, A. L., Theys, C., Ferrari, A., Lanteri, H., and Bertero, M. (2008). The study of an iterative method for the reconstruction of images corrupted by poisson and gaussian noise. *Inverse Problems*, 24(3), 1–20.
- Bertero, M. and Boccacci, P. (1998). *Introduction to inverse problems in imaging*. Institute of Physics Publishing, Bristol.
- Bertero, M., Boccacci, P., and Vicidomini, G. D. G. (2009). Image deblurring with Poisson data: from cells to galaxies. *Inverse Problems*, 25(12), 1–26.
- Bini, A. and Bhat, M. (2014). Despeckling low SNR, low contrast ultrasound images via anisotropic level set diffusion. *Multidimensional Systems and Signal Processing*, 25(1), 41–65.
- Borengasser, M., Hungate, W. S., and Watkins, R. (2007). *Hyperspectral remote sensing: principles and applications*. CRC press, Indiana State University Terre Haute, Indiana, U.S.A.
- Bregman, M. L. (1967). The relaxation method of finding the common point of convex sets and its application to the solution of problems in convex programming. *USSR computational mathematics and mathematical physics*, 7(3), 200–217.
- Buades, A., Coll, B., and Morel, J. (2005). A non-local algorithm for image denoising. In *2005 IEEE Computer Society Conference on Computer Vision and Pattern Recognition (CVPR'05)*, 2, 1–6.
- Chakrabarti, A. and Zickler, T. E. (2012). Image restoration with signal-dependent camera noise. *Computing Research Repository - arXiv*, 1204.
- Chambolle, A. and Pock, T. (2010). A first-order primal-dual algorithm for convex problems with applications to imaging. *Journal of Mathematical Imaging and Vision*, 40(1), 120–145.
- Chan, S., Khoshabeh, R., Gibson, K. B., Gill, P. E., and Nguyen, T. Q. (2011). An augmented Lagrangian method for total variation video restoration. *IEEE Transactions on Image Processing*, 20(11), 3097–3111.



- Chan, Y. K. and Koo, V. C. (2008). An introduction to Synthetic Aperture Radar (SAR). *Progress In Electromagnetics Research*, 2, 27–60.
- Chang, C.-I. (2003). *Hyperspectral imaging: techniques for spectral detection and classification*, 1. Springer Science & Business Media, US.
- Chang, L., ChaoBang, G., and Xi, Y. (2015). A MRI denoising method based on 3D nonlocal means and multidimensional PCA. *Computational and Mathematical Methods in Medicine*, 2015(1), 1–11.
- Combettes, P. and Wajs, V. (2005). Signal recovery by proximal forward-backward splitting. *SIAM Multiscale Modeling and Simulation*, 4(4), 1168–1200.
- Dabov, K., Foi, A., Katkovnik, V., and Egiazarian, K. (2007). Image denoising by sparse 3-D transform-domain collaborative filtering. *IEEE Transactions on Image Processing*, 16(8), 2080–2095.
- De Gonzalez, A. B., Mahesh, M., Kim, K. P., Bhargavan, M., Lewis, R., Mettler, F., and Land, C. (2009). Projected cancer risks from computed tomographic scans performed in the United States in 2007. *Archives of internal medicine*, 169(22), 2071–2077.
- Deger, F., Mansouri, A., Pedersen, M., Hardeberg, J. Y., and Voisin, Y. (2015). A sensor-data-based denoising framework for hyperspectral images. *Optics express*, 23(3), 1938–1950.
- Dey, N., Blanc-Feraud, L., Zimmer, C., Roux, P., Kam, Z., Olivo-Marin, J.-C., and Zerubia, J. (2006). Richardson–Lucy algorithm with total variation regularization for 3D confocal microscope deconvolution. *Microscopy research and technique*, 69(4), 260–266.
- Dong, F., Zhang, H., and Kong, D. (2012). Nonlocal total variation models for multiplicative noise removal using split Bregman iteration. *Mathematical and Computer Modelling*, 55(3), 939–954.

- Esedoglu, S. and Osher, S. J. (2004). Decomposition of images by the anisotropic Rudin-Osher-Fatemi model. *Communications on pure and applied mathematics*, 57(12), 1609–1626.
- Feng, W. and Chen, Y. (2015). Fast and accurate Poisson denoising with optimized nonlinear diffusion. *Computing Research Repository - arXiv*, 1510.
- Fernandez, S. A. and Lopez, C. A. (2006). On the estimation of the coefficient of variation for anisotropic diffusion speckle filtering. *IEEE Transactions on Image Processing*, 15(10), 2694–2701.
- Fernandez, S. A. and Vega, A. T. (2013). A review on statistical noise models for magnetic resonance imaging. *Tech Report of the LPI, TECH-LPI2013-01, Universidad de Valladolid, Spain*, (1), 1–23.
- Fernandez, S. A., Vega, A. T., and Lopez, C. A. (2009). Noise estimation in single- and multiple-coil magnetic resonance data based on statistical models. *Magnetic Resonance Imaging*, 27(10), 1397–1409.
- Foi, A. (2011). Noise estimation and removal in MR imaging: The variance-stabilization approach. In *2011 IEEE International Symposium on Biomedical Imaging: From Nano to Macro*, 1809–1814.
- Gelfand, I. and Fomin, S. (1963). *Calculus of variations: Revised English edition translated and edited by Richard A. Silverman*. Prentice Hall Inc., Englewood Cliffs.
- Getreuer, P. (2012a). Rudin-Osher-Fatemi total variation denoising using split Bregman. *Image Processing online*, 2(1), 74–95.
- Getreuer, P. (2012b). Total variation deconvolution using split Bregman. *Image processing online*, 2(1), 158–174.
- Gilboa, G. (2018). *Nonlinear Eigenproblems in Image Processing and Computer Vision*. Springer International Publishing, Gewerbestrasse 11, 6330 Cham, Switzerland.

- Gilboa, G. and Osher, S. (2008). Nonlocal operators with applications to image processing. *SIAM Multiscale Mod. Simul. (MMS)*, 7(3), 1005–1028.
- Giryas, R. and Elad, M. (2014). Poisson denoising using sparse representations and dictionary learning. *IEEE Transactions on Image Processing*, 23(12), 5057–5069.
- Goldstein, T., Bresson, X., and Osher, S. (2010). Geometric applications of the split Bregman method: Segmentation and surface reconstruction. *Journal of Scientific Computing*, 45(1), 272–293.
- Goldstein, T. and Osher, S. (2009). The split Bregman method for L1-regularized problems. *SIAM journal on imaging sciences*, 2(2), 323–343.
- Golshan, H., Hasanzadeh, R., and Yousefzadeh, C. (2013). An MRI denoising method using image data redundancy and local snr estimation. *Magnetic Resonance Imaging*, 31(7), 1206–17.
- Gonzalez, R. C. and Woods, R. E. (2006). *Digital Image Processing (3rd Edition)*. Prentice-Hall, Inc., Upper Saddle River, NJ, USA.
- Gunturk, B. K. and Li, X. (2012). *Image restoration: fundamentals and advances*. CRC Press, Indiana State University Terre Haute, Indiana, U.S.A.
- Hadamard, J. and Morse, P. M. (1953). *Lectures on Cauchy’s problem in linear partial differential equations*, 6. Dover Publications, New York.
- Hansen, P. C. (2010). *Discrete inverse problems: insight and algorithms*, 7. SIAM, Society for Industrial and Applied Mathematics, Philadelphia.
- Hansen, P. C., Nagy, J. G., and O’leary, D. P. (2006). *Deblurring images: matrices, spectra, and filtering*, 3. SIAM, Society for Industrial and Applied Mathematics, Philadelphia.
- Hounsfield, G. N. (1973). Computerized transverse axial scanning (tomography): Part 1. description of system. *The British journal of radiology*, 46(552), 1016–1022.

- Hsieh, J. et al. (2009). *Computed tomography: principles, design, artifacts, and recent advances*, PM259. SPIE Bellingham, Western Australia.
- Jia, R.-Q., Zhao, H., and Zhao, W. (2009). Convergence analysis of the bregman method for the variational model of image denoising. *Applied and Computational Harmonic Analysis*, 27(3), 367–379.
- Jin, Z. and Yang, X. (2011a). A variational model to remove the multiplicative noise in ultrasound images. *Journal of Mathematical Imaging and Vision*, 39(1), 64–71.
- Jin, Z. and Yang, X. (2011b). A variational model to remove the multiplicative noise in ultrasound images. *J. Math. Imaging Vis.*, 39(1), 64–71.
- Jost, J. and Li Jost, X. (1998). *Calculus of variations*, 64. Cambridge University Press, New York.
- Kais, G., Noureddine, E., and Chedly, F. M. (2016). Comparative analysis between a variational method and wavelet method pure-let to remove poisson noise corrupting ct images. In *Systems, Signals & Devices (SSD), 2016 13th International Multi-Conference on*, 287–294. IEEE.
- Kempen, G. V. (1999). *Image Restoration in Fluorescence Microscopy, PhD thesis*. Delft University, The Netherlands.
- Kervrann, C. and Trubuil, A. (2004). An adaptive window approach for poisson noise reduction and structure preserving in confocal microscopy. In *Biomedical Imaging: Nano to Macro, 2004. IEEE International Symposium on*, 788–791. IEEE.
- Krissian, K., Kikinis, R., Westin, C., and Vosburgh, K. (2005). Speckle constrained filtering of ultrasound images. In *IEEE Comput. Vis. Pattern Recogn. (CVPR)*, 547–552.
- Krissian, K., Westin, C.-F., Kikinis, R., and Vosburgh, K. (2007). Oriented speckle reducing anisotropic diffusion. *IEEE Transactions on Image Processing*, 16(5), 1412–1424.

- Kuijper, A. (2007). P-Laplacian driven image processing. In *2007 IEEE International Conference on Image Processing*, 5, 257–260.
- Lakowicz, J. R. (2006). *Principles of Fluorescence Spectroscopy, 3rd edition*. Springer US.
- Lanza, A., Morigi, S., Sgallari, F., and Wen, Y.-W. (2014). Image restoration with poisson-gaussian mixed noise. *Computer Methods in Biomechanics and Biomedical Engineering: Imaging & Visualization*, 2(1), 12–24.
- Le, T., Chartrand, R., and Asaki, T. J. (2007). A variational approach to reconstructing images corrupted by poisson noise. *Journal of Mathematical Imaging and Vision*, 27(3), 257–263.
- Lemarechal, C. and Hiriart Urruty, J. (1996). *Convex analysis and minimization algorithms I*, 305. Springer Verlag Berlin, Heidelberg.
- Li, H., Wu, J., Miao, A., Yu, P., Chen, J., and Zhang, Y. (2017). Rayleigh-maximum-likelihood bilateral filter for ultrasound image enhancement. *Biomedical engineering online*, 16(1), 46.
- Li, L., Kasabov, N., Yang, J., Yao, L., and Jia, Z. (2015). Poisson image denoising based on BLS-GSM method. In *Neural Information Processing*, 513–522. Springer International Publishing.
- Lillesand, T., Kiefer, R. W., and Chipman, J. (2014). *Remote sensing and image interpretation, 7th edition*. John Wiley & Sons, USA.
- Liu, H., Zhang, Z., Xiao, L., and Wei, Z. (2017). Poisson noise removal based on nonlocal total variation with Euler’s elastica pre-processing. *Journal of Shanghai Jiaotong University (Science)*, 22(5), 609–614.
- Liu, R., Shi, L., Huang, W., Xu, J., Yu, S., and Wang, D. (2014). Generalized total variation-based MRI Rician denoising model with spatially adaptive regularization parameters. *Magnetic Resonance Imaging*, 32(6), 702–20.

- Liu, R., Shi, L., Simon, C. H. Y., and Wang, D. (2015). A two-step optimization approach for nonlocal total variation-based Rician noise reduction in magnetic resonance images. *Medical Physics*, 42(9), 5167–87.
- Liu, X. and Huang, L. (2011). Split bregman iteration algorithm for total bounded variation regularization based image deblurring. *Journal of Mathematical Analysis and Applications*, 372(2), 486–495.
- Luisier, F., Blu, T., and Unser, M. (2011). Image denoising in mixed poisson-gaussian noise. *IEEE Transactions on Image Processing*, 20(3), 696–708.
- Makitalo, M. and Foi, A. (2013a). Optimal inversion of the generalized anscombe transformation for poisson-gaussian noise. *IEEE Transactions on Image Processing*, 22(1), 91–103.
- Makitalo, M. and Foi, A. (2013b). Optimal inversion of the generalized anscombe transformation for poisson-gaussian noise. *IEEE Transactions on Image Processing*, 22(1), 91–103.
- Mäkitalo, M., Foi, A., Fevrale, D., and Lukin, V. (2010). Denoising of single-look sar images based on variance stabilization and nonlocal filters. In *Mathematical Methods in Electromagnetic Theory (MMET), 2010 International Conference on*, 1–4. IEEE.
- Manjo, J., Carbonell-Caballero, J., Lull, J., Gracia, G., Bonmat, L., and Robles, M. (2008). MRI denoising using non-local means. *Medical Image Analysis*, 12(1), 514–523.
- Mansouri, A., Deger, F., Pedersen, M., Hardeberg, J. Y., and Voisin, Y. (2016). An adaptive spatial–spectral total variation approach for poisson noise removal in hyperspectral images. *Signal, Image and Video Processing*, 10(3), 447–454.
- Marquina, A. and Osher, S. (2000). Explicit algorithms for a new time dependent model based on level set motion for nonlinear deblurring and noise removal. *SIAM Journal on Scientific Computing*, 22(2), 387–405.

- Milanfar, P. (2013). A tour of modern image filtering: New insights and methods, both practical and theoretical. *IEEE Signal Processing Magazine*, 30(1), 106–128.
- Mohammad Djafari, A. (2002). Bayesian inference for inverse problems. In *Bayesian Inference and Maximum Entropy Methods in Science and Engineering*, 617 of *American Institute of Physics Conference Series*, 477–496.
- Mondal, P. P. and Diaspro, A. (2013). *Fundamentals of Fluorescence Microscopy, Exploring Life with Light*. Springer, Netherlands.
- Mukherjee, P. and Qiu, P. (2011). 3-D image denoising by local smoothing and non-parametric regression. *Technometrics*, 53(2), 196–208.
- Osher, S., Burger, M., Goldfarb, D., Xu, J., and Yin, W. (2005). An iterative regularization method for total variation-based image restoration. *Multiscale Modeling & Simulation*, 4(2), 460–489.
- Perona, P. and Malik, J. (1990). Scale-space and edge detection using anisotropic diffusion. *IEEE Transactions on Pattern Analysis and Machine Intelligence*, 12(7), 629–639.
- Porcello, L. J., Massey, N. G., Innes, R. B., and Marks, J. M. (1976). Speckle reduction in synthetic-aperture radars. *Journal of the Optical Society of America*, 66(11), 1305–1311.
- Rajan, J., Veraart, J., Audekerke, J., Verhoye, M., and Sijbers, J. (2012). Nonlocal maximum likelihood estimation method for denoising multiple-coil magnetic resonance images. *Magnetic Resonance Imaging*, 30(10), 1512–1518.
- Rond, A., Giryes, R., and Elad, M. (2016). Poisson inverse problems by the plug-and-play scheme. *Journal of Visual Communication and Image Representation*, 41, 96–108.
- Rudin, L., Lions, P. L., and Osher, S. (2003). *Multiplicative Denoising and Deblurring: Theory and Algorithms*, 103–119. Springer New York, US.

- Rudin, L. I., Osher, S., and Fatemi, E. (1992). Nonlinear total variation based noise removal algorithms. *Physica D: nonlinear phenomena*, 60(1), 259–268.
- Salmon, J., Harmany, Z., Deledalle, C.-A., and Willett, R. (2014). Poisson noise reduction with non-local pca. *Journal of mathematical imaging and vision*, 48(2), 279–294.
- Sarode, M. V. and Deshmukh, P. R. (2011). Reduction of speckle noise and image enhancement of images using filtering technique. *International Journal of Advancements in Technology*, 2(1), 30–38.
- Shuai, L., Ximei, Z., and Guodong, W. (2015). Non local TV model for multiplicative noise with Rayleigh distribution removal. *Chinese Journal of Scientific Instrument*, 36(7), 1570–1576.
- Sijbers, J. and den Dekker, A. (2004). Maximum likelihood estimation of signal amplitude and noise variance from MR data. *Magnetic Resonance in Medicine*, 51(3), 586–594.
- Sijbers, J., den Dekker, A., der Linden, A. V., Verhoye, M., and Dyck, D. V. (1999). Adaptive anisotropic noise filtering for magnitude MR data. *Magnetic Resonance in Medicine*, 17(10), 1533–1539.
- Smith, N. B. and Webb, A. (2010). *Introduction to medical imaging: physics, engineering and clinical applications*. Cambridge university press, Cambridge, UK.
- Soumya, V., Varghese, A., Manesh, T., and Neetha, K. (2016). Denoising multi-coil magnetic resonance imaging using nonlocal means on extended LMMSE. In *Advances in Signal Processing and Intelligent Recognition Systems*, 187–198. Springer.
- Srivastava, R. and Srivastava, S. (2013). Restoration of Poisson noise corrupted digital images with nonlinear pde based filters along with the choice of regularization parameter estimation. *Pattern Recognition Letters*, 34(10), 1175–1185.



- Suna, Q., Hossackb, J., Tangc, J., and Acton, S. (2004). Speckle reducing anisotropic diffusion for 3D ultrasound images. *Computerized Medical Imaging and Graphics*, 28(2), 461–470.
- Svoboda, D., Ulman, V., Kovavc, P., Vsalingova, B., Tesavrova, L., Koutna, I. K., and Matula, P. (2016). Vascular network formation in silico using the extended cellular potts model. In *Image Processing (ICIP), 2016 IEEE International Conference on*, 3180–3183. IEEE.
- Ta, V. T., Bougleux, S., Elmoataz, A., and Lezoray, O. (2007). Nonlocal Anisotropic Discrete Regularization for Image, Data Filtering and Clustering. Tech. Rep., University of Caen, Caen, France.
- Tikhonov, A. N. and Arsenin, V. Y. (1977). *Solutions of ill-posed problems*. V. H. Winston & Sons, Washington, D.C.: John Wiley & Sons, New York-Toronto, London.
- Vogel, C. R. (2002). *Computational methods for inverse problems*, 23. SIAM, Society for Industrial and Applied Mathematics, Philadelphia.
- Wang, W. and He, C. (2017). A fast and effective algorithm for a poisson denoising model with total variation. *IEEE Signal Processing Letters*, 24(3), 269–273.
- Wang, Z., Bovik, C. A., Sheikh, R. H., and P Simoncelli, E. (2004). Image quality assessment: from error visibility to structural similarity. *IEEE transactions on image processing*, 13(4), 600–612.
- Weickert, J. (1997). A review of nonlinear diffusion filtering. In *Scale-Space Theory in Computer Vision*, 1–28, Berlin, Heidelberg. Springer Berlin Heidelberg.
- Wood, J. and Johnson, K. (1999). Wavelet packet denoising of magnetic resonance images: importance of Rician noise at low SNR. *Magnetic Resonance in Medicine*, 41(3), 631–635.
- Wotao, Y., Osher, S., Goldfarb, D., and Darbon, J. (2008). Bregman iterative algorithms for  $\ell_1$ -minimization with applications to compressed sensing. *SIAM Journal on Imaging Sciences*, 1(1), 143–168.

- Yahya, N., Kamel, N. S., and Malik, A. S. (2014). Subspace-based technique for speckle noise reduction in SAR images. *IEEE Transactions On Geoscience and remote sensing*, 52(10), 6257–6271.
- Yu, Y. and Acton, S. (2002). Speckle reducing anisotropic diffusion. *IEEE Transactions on Image Processing*, 11(11), 1260–1270.
- Zhang, J. and Hirakawa, K. (2017). Improved denoising via Poisson mixture modeling of image sensor noise. *IEEE Transactions on Image Processing*, 26(4), 1565–1578.
- Zhang, X., Burger, M., Bresson, X., and Osher, S. (2010). Bregmanized nonlocal regularization for deconvolution and sparse reconstruction. *SIAM Journal on Imaging Sciences*, 3(3), 253–276.
- Zhang, Z., Huang, L., FEI, X., and WEI, Z. (2014). Image Poisson denoising model and algorithm based on nonlocal TV regularization. *Journal of System Simulation*, 26(9), 2010–2015.
- Zhu, M. and Chan, T. (2008). An efficient primal-dual hybrid gradient algorithm for total variation image restoration. *UCLA CAM technical report, 08-34*.
- Zhu, Y., Zhao, M., Zhao, Y., Li, H., and Zhang, P. (2012). Noise reduction with low dose CT data based on a modified ROF model. *Optics express*, 20(16), 17987–18004.
- Zosso, D., Tran, G., and Osher, S. (2013). A unifying retinex model based on non-local differential operators. In *Computational Imaging XI*, 8657, 1–16. International Society for Optics and Photonics.

# LIST OF PUBLICATIONS

## Journal Publications

- [1] P. Jidesh, Shivaram Holla (2017). “Non-local total bounded variation scheme for multiple-coil magnetic resonance image restoration”, *Multidimensional Systems and Signal Processing* (Springer US), 29(4), 1427-1448. *Indexing :SCI*  
doi:10.1007/s11045-017-0510-z.
- [2] P. Jidesh, Shivarama Holla K. (2018), “Non-local total variation regularization models for image restoration”, *Computers and Electrical Engineering* (Elsevier), 67(1), 114-133. *Indexing :SCI*  
doi:10.1016/j.compeleceng.2018.03.014.
- [3] Shivarama Holla K, P. Jidesh (2018), “Non-local total variation regularization approach for image restoration under a Poisson degradation”, *Journal of modern optics* (Taylor & Francis), 65(19), 2231-2242. *Indexing :SCI*  
doi:10.1080/09500340.2018.1506058



## BIO-DATA

**Name** : Shivarama Holla K  
**Email Id** : shivaram.holla@gmail.com  
**Contact No** : +91-8547525635 / 9611226014  
**Date of Birth** : 20<sup>th</sup> February , 1993  
**Permanent address** : S/o. K Gopalakrishna Holla,  
Kayyar house,  
(Post) Kayyar,  
Via Uppala,  
Kasaragod,  
Kerala , India.  
Pin code - 671322

### Educational Qualifications:

<b>Degree</b>	<b>Year of Passing</b>	<b>Institution/University</b>
B.Sc. (Physics, Mathematics, Computer Science)	2013	Canara First Grade College, Mangaluru University
M.Sc. (Computer Science)	2015	Mangaluru University.